THEORY OF DIPOLES, ARRAY FACTORS, AND MULTI-ELEMENT ANTENNAS WITH PHYSICS-BASED PROPAGATION FOR MOBILE COMMUNICATIONS

by

Maryam Dehghani Estarki

M.Sc., University of Tehran, 2004

B.Sc., University of Tehran, 2000

a Thesis submitted in partial fulfillment of
the requirements for the degree of

Doctor of Philosophy

in the
School of Engineering Science
Faculty of Applied Sciences

SIMON FRASER UNIVERSITY
Summer 2014

APPROVAL

Name: Maryam Dehghani Estarki

Degree: Doctor of Philosophy

Title of Thesis: Theory of Dipoles, Array Factors, and Multi-Element Antennas with Physics-Based Propagation for Mobile Communications

Examining Committee: Dr. Jie Liang, Associate Professor, Ph.D., P.Eng.
Chair

Dr. Rodney G. Vaughan
Senior Supervisor, Professor, Ph.D., P.Eng.

Dr. Shawn Stapleton
Supervisor, Professor, Ph.D., P.Eng.

Dr. Daniel Janse van Rensburg, Nearfield Systems, Adjunct Professor, Supervisor, Ph.D., P.Eng.

Dr. Behrouz Pourseyed, Sierra Wireless Inc., RF Director, Supervisor, Ph.D.

Dr. Daniel C. Lee, Simon Fraser University
Internal Examiner, Professor, Ph.D., P.Eng.

Dr. Robert Paknys, Concordia University, ECE Dept.
External Examiner, Professor, Ph.D., P.Eng.

Date Defended/Approved: April 29, 2014

Partial Copyright Licence

Abstract

Bandwidth, volume and energy are the basic resources for communications, and current signal processing techniques use these in many different ways. The bandwidth is limited by the antenna size, and maximizing the bandwidth of the elements and the design of multi-element antennas (MEAs) require new research. This two-part thesis addresses antenna-theoretic bandwidth and MEA evaluation.

The limiting bandwidth of the most fundamental antenna element - the dipole - remains elusive despite its long research history. This motivates Part I, in which the bandwidth of the electric dipole is developed from theoretical and numerical methods, and recent measurements. The resulting antenna-theoretic bandwidth of the dipole with a feed gap offers new benchmark results for compact elements. The lossless, thin dipole with finite gap has a much wider bandwidth than was previously known, and the non-radiating feed is identified as the challenge to realize the available bandwidth.

Using multiple-input multiple-output (MIMO) and other diversity techniques with large dimensions (many elements) is the key technology for high spectral efficiency. But large-dimension MIMO is not yet used commercially, and the design methodology and evaluation of MEAs is undeveloped. There is no standard for evaluating MEAs used for MIMO communications, and currently, the physical evaluation of a MIMO terminal comprises coarse throughput tests in an idealized environment. The real-world performance of the terminal, and especially the antenna performance, remains unclear from such tests. This motivates Part II, which explores MEA evaluation using physical antenna parameters together with site-specific, ray-traced models for the spatial channel. Ray-tracing calculation is well established, but its application with MEAs is in its infancy. Using third-party ray-tracing files, an approach for evaluating MEAs for urban channels is presented. The advantage is that it maintains the full control of being computer-driven, thereby avoiding expensive,

hard-to-repeat physical measurements, while incorporating the ground-truth of empirical antenna parameters.

key words: wire dipole; Q bounds; mm wave antennas; array; ray-tracing; MIMO/diversity

To my parents, Mehrzad and Mahmood,
for all the beauty and love they always fill my life with,
and to my brother, Maziar,
for his unconditional friendship and support.
Maral

"It took me so long to figure out where he was coming from. The Little Prince, who was asking me too many questions, did not seem to hear at all the ones I was asking him. It was from the words uttered by chance that, little by little, everything was revealed to me."

— *The Little Prince*, Antoine de Saint-Exupry, *1900-1944*

Acknowledgments

I always knew writing this part of the thesis would be the hardest. Since I started this journey, many amazing people have been accompanying me, without their love, support, care, patience and endurance, I have never been able to survive a single day. I would like to acknowledge some of these many people.

There is no way to thank my senior supervisor at the School of Engineering Science, SFU, Dr. Rodney G. Vaughan. He invited me to work in his research group when I was about to leave this school. He changed my points of views about science and research. This thesis and all my publications were accomplished by his constant supervision and support. Though, what I learnt from Rodney is much more than my research and my papers. He assisted me improving my writing style and my communications skills. During the stages that I was physically and emotionally weak, Rodney and his encouraging words made me feel stronger, stand up and proceed. Whenever I was demotivated and frustrated of research, he was there offering a new approach. Many of his brilliant ideas have become the foundation of the present dissertation. In response to my faults and mistakes, he was patient and forgiving. Being a member of his research team was one of the best things ever happened to me. He helped me gain back my interest in research. At last, I have to mention that he financially supported me from the very first day I joined his team till the day I defended my thesis and that made the way much smoother for me to pass.

I wish to express my sincere gratitude and appreciation to my former supervisors, Dr. Dong In Kim and Dr. Paul Ho. Dr. Kim gave me the admission to join SFU and start my PhD in Vancouver. He supervised me during the first two semesters of my study at SFU. He is one of the most knowledgeable people in the ultra wideband research and a great mentor in this field. I also want to thank Dr. Paul Ho, my second (temporary) supervisor, for all I learnt from him during the single semester I worked with him. He is

an excellent teacher and I very much profited from his guidance and knowledge in digital communications.

I am so grateful to my supervisor Dr. Shawn Stapleton who has always been positive about my work and research since September 2007 that I started working with him as a teaching assistant. It was a great pleasure to work for him. Since then, he has been one of my best friends at SFU from whom I always get advice.

I want to thank my supervisor, Dr. Daniel Janse van Rensburg from Nearfield Systems Inc. Daniel traveled from the other side of the country, made it to my defence session and provided me with thoughtful comments and questions. His comments were so detailed and he had captured some points that I had not seen before.

I wish to express my appreciation to Dr. Behrouz Pourseyed from Sierra Wireless Inc. He became a member of my supervisory committee despite his busy schedule and supervised my thesis progress insightfully. Behrouz's practical comments prompted me to consider the problem from another angle. His brilliant questions during the defence session delighted me.

It is my honor to thank my external examiner, Dr. Robert Paknys who traveled from Montreal for my defence. He provided me with great comments during the defence session and left me with his precious constructive notes after the defence.

I want to express my gratitude to Dr. Daniel C. Lee, my internal examiner, for his insightful questions and for his nice and supportive contribution. I was always inspired by his passion for learning and teaching. He is always around and always eager for new ideas.

I am thankful to the defence chair, Dr. Jie Liang for his valuable contribution. He is an amazing graduate chair who is always there to assist you.

I warmly acknowledge Dr. Yvo de Jong from Communications Research Centre Canada (CRC), and Dr. Thomas Kürner and Mr. Jörg Nuckelt from Braunschweig Technische Universität Germany for generating and supplying a sample file of simulated channels. They patiently answered my questions and kindly helped me all along the way.

I want to thank all the faculty and staff of the School of Engineering Science for their support during my graduate study at SFU. Especially, I want to thank Ms. Raj Pabla, Ms. Lindsay Ward, Ms. Roya Ghorab, Mr. Chao C. Cheng, Mr. Gary Houghton, Mr. Gary Shum and Mr. Bryan Sales.

I am so grateful to my amazing mentors at the Engineering Science Co-operative Education Program at SFU for their support and encouragement, especially to Ms. Harriet Chicoine for her trust and encouragement. During the two semesters with Co-op office, I

enjoyed working with Ms. Shannon Danson, Ms. Isabella Silvestre and Ms. Heather Keeping. I express my appreciation to Mr. Steve Whitmore for all I learnt from his writing course and all the joy I had while I was working as a TA for him.

I thank Health and Counselling Services at SFU, especially Dr. Dianne Vosloo and Ms. Enzula Tavormina for the all the efficient sessions I had with them.

I am indebted to my lab colleagues for their friendship, encouragement and advice during these years. Jane Xing Yun helped me a lot in using simulation packages. She kindly provided me with the patterns of the antennas she had simulated and measured. My colleague, Xu Han, also, assisted me a lot in numerical methods. I express my special thanks to the past and current members of the Sierra Wireless Communications Laboratory, Nima Mahanfar, Sara Bavarian, Shirin Karimifar, Ted Liu, Jinyun Ren, Muhammad Naeem, Alireza Banani, Mehdi Seyfi, Piraj Fozoonmayeh, Omar Altrad, Jaspreet Oberoi, Moein Shayegan Nia, Saeed Asharfinia, Milad Amir Toutounchian, Ali Zarei, Maryam Razmhosseini, Ying Chen, Abhijit Bhattacharya and Hanieh Khalilian.

I also want to thank my amazing friends form SFU who were always there for me, Arina Aboonabi, Lila Torabi, Parastoo Dehkordi, Mahsa Najibi, Farnaz Gharibian, Leila Kalantari, Reza Entezari, Maryam Soleimani, Esmaeil Tafazzoli, Neda Changizi, Vahid Kazempour and Kaveh Kianfar. I want to thank my friends Anooshe Bazzazan, Alireza Saremi, Nooshin Karimifar and Azadeh Hajihosseini for their support and encouragement.

I would like to thank my friends Mona Jafarnejad, Vafa Sarmast, Neda Ehtiati and Sahar Ayazian for being so close to me although they are so far away from Vancouver and for being so amazing to me all the time.

I am grateful to my beloved friend, Armita Kaboli. There is no way to thank her (and her family) for the priceless friendship. She always gave me courage and energy. She was listening patiently to me and was offering me incredible solutions.

I wish to thank my aunts and uncles and my beloved cousins who were so supportive from different parts of the world. I want to thank my Grandma, Irandokht Aminian, who has been the best Grandma ever. I will always remain thankful and grateful to them.

I have no word to thank my dear friend Hassan Goldani Moghaddam who never stopped supporting, encouraging and helping me. He was unbelievably patient with me throughout my research and was always encouraging and understanding during the toughest times. He was by my side all over my study at SFU. While I was so overwhelmed by my thesis, every night he was coming to the lab with a big smile and a bar of chocolate asking me how my

day had been. Whenever I had a programming problem, he was so patient listening to my complaints, going through my codes and helping me debugging. He explained the same concepts over and over to me until I actually understood the ideas fully. I want to thank him for all his support while I was ill and sad, while I was happy and strong.

My greatest debt of gratitude is to my family. It is impossible to thank my family for all they did for me. My parents, Mehrzad and Mahmood, believed in me and were consistently positive and optimistic about my choice. They encouraged me to pursue my dreams. They sacrificed their life for me to run after my passion and become who I am. For the past eight years, they called me every day cheering me up with their energetic voice. I admire them for being so amazing parents. They are my first teachers and my role models. I am always thankful and grateful to them. I am so thankful to my brother, Maziar, for his endless kindness, patience and support. During the toughest parts of my PhD, he came and stayed with me and put up with me and never frowned even once in response to my countless days of sickness and sadness. He always forgave me for my faults and appreciated me for my achievements. This thesis is the least I can dedicate to my family.

Contents

List of Tables

List of Figures

List of Symbols

$\{.\}^{\mathrm{T}}$	Transposition
$\{.\}^{*}$	Complex conjugate
$\{.\}^{\mathrm{H}}$	Transpose complex conjugate
$\|.\|$	Absolute value
$\langle\ ,\ \rangle$	Inner product
a	Radius of wire dipole
$a_{ij}^{\theta\theta}$	Amplitude of the jth discrete component at the ith receiver, for the vertical-vertical (θ-θ) polarization component
$a_{ij}^{\theta\phi}$	Amplitude of the jth discrete component at the ith receiver, for the vertical-horizontal (θ-ϕ) polarization component
$a_{ij}^{\phi\theta}$	Amplitude of the jth discrete component at the ith receiver, for the horizontal-vertical (ϕ-θ) polarization component
$a_{ij}^{\phi\phi}$	Amplitude of the jth discrete component at the ith receiver, for the horizontal-horizontal (ϕ-ϕ) polarization component
$\alpha_{ij}^{\theta\theta}$	Phase of the jth discrete component at the ith receiver, vertical-vertical (θ-θ) polarization component
$\alpha_{ij}^{\theta\phi}$	Phase of the jth discrete component at the ith receiver, vertical-horizontal (θ-ϕ) polarization component
$\alpha_{ij}^{\phi\theta}$	Phase of the jth discrete component at the ith receiver, horizontal-vertical (ϕ-θ) polarization component
$\alpha_{ij}^{\phi\phi}$	Phase of the jth discrete component at the ith receiver, horizontal-horizontal (ϕ-ϕ) polarization component
A	Area of the cross section of a conductor
BW_{3dB}	Half power (3dB) impedance bandwidth

$BW_{3dB}^{(L)}$	Relative loaded double-sided half power (3dB) impedance bandwidth
$BW_{3dB}^{(L,T)}$	Loaded theoretical half power (3dB) impedance bandwidth
$b_{r_i}^{\theta\theta}$	Amplitude of the summed field at the ith receiver, (θ-θ) polarization component
$\beta_{r_i}^{\theta\theta}$	Phase of the summed field at the ith receiver, (θ-θ) polarization component
$b_{0_i}^{\theta\theta}$	Demeaned signal at the ith receive point
C	Capacitance
$\frac{C}{B}$	Capacity efficiency
$C(d, \gamma)$	Correlation between two patterns in terms of d and γ
D	Directivity of an antenna
$\mathrm{DG}_{DIV}(dB)$	Diversity gain in dB
D_{LA}	Linear array factor directivity
d	Distance, spacing
d_{TR}	Distance between transmitting and receiving antennas
d_{r_i}	Distance between the transmitting antenna and the ith receiving antenna
δ	Dirac function
δ_g	Gap size
δ_S	Skin depth (the depth of the conductor at which the current reduces to $\frac{1}{e}$ or 37% of its surface value
$\Delta\omega_{3dB}$	Half power (3dB) impedance angular frequency bandwidth
e	Napier's constant
C_{Euler}	Euler constant
$\mathbf{E}$	Electric field (vector)
E_b/N_0	Energy per bit to noise power spectral density ratio
$E_{inc}^{\theta\theta}$	Incident (normalized) electric field at the antenna (for polarization component (θ-θ))
ϵ	Permittivity
ϵ_r	Relative permittivity
ϵ_0	Permittivity of air
η_{total}	Total efficiency
η_{pol}	Polarization efficiency
η_{imp}	Impedance mismatch efficiency

η_{rad}	Antenna radiation efficiency
$\mathbf{E_R}(\omega, \mathbf{r})$	Vector electric field as a function of frequency and position
$E_x(\omega, \mathbf{r})$	Electric field components in x direction (complex scalar)
$E_y(\omega, \mathbf{r})$	Electric field components in y direction (complex scalar)
$E_z(\omega, \mathbf{r})$	Electric field components in z direction (complex scalar)
f	Frequency
$f_{filter}(\tau)$	Narrowband filter complex amplitude in time domain
$f(\theta, \phi)$	Common element pattern (in an array)
$f_\theta(\theta, \phi)$	Scalar common element pattern for $\hat{\theta}$ polarization
$f_\phi(\theta, \phi)$	Scalar common element pattern for $\hat{\phi}$ polarization
F_{LA}	Linear array factor
$F_{filter}(\omega_{BB})$	Narrowband filter complex amplitude baseband frequency response at baseband frequency
$g_{r_i}^{\theta\theta}$	Summed ray, i.e., received impulse response, at the ith receiver along the trajectory, for vertical-vertical (θ-θ) polarization component
$g_{r_i}^{\phi\theta}$	Summed ray, i.e., received impulse response, at the ith receiver point along the trajectory, for horizontal-vertical (ϕ-θ) polarization component
$g_{r_i}^{\theta\phi}$	Summed ray, i.e., received impulse response, at the ith receiver point along the trajectory, for vertical-horizontal (θ-ϕ) polarization component
$g_{r_i}^{\phi\phi}$	Summed ray, i.e., received impulse response, at the ith receiver point along the trajectory, for horizontal-horizontal (ϕ-ϕ) polarization component
$\mathbf{g}_{r_i}$	Summed-ray (impulse response) polarization matrix
G	Gain of an antenna
$G_T(\theta_T, \phi_T)$	Directional gain for the transmitting antenna
$G_R(\theta_R, \phi_R)$	Directional gain for the receiving antenna
γ	Phase shift of the phased array antenna
γ_k	Energy ratio for the kth antenna branch, i.e., $SNR_k = q_k^2$
γ_C	SNR of the combined signal
γ_{ref}	Instantaneous SNR of a reference signal
Γ_C	Mean SNR of the combined signal
Γ_{ref}	Mean SNR of a reference signal
Γ_k	Mean SNR for the kth antenna branch, i.e., $\Gamma_k = \langle \gamma_k \rangle$
Γ_{refl}	Signal reflection coefficient

$\|\Gamma_{refl}\|^2$	Power reflection coefficient
$\hat{e}$	Electric polarization vector
$\mathbf{H_R}(\omega, \mathbf{r})$	Vector magnetic field as a function of frequency and position
$H_x(\omega, \mathbf{r})$	Magnetic field components in x direction (complex scalar)
$H_y(\omega, \mathbf{r})$	Magnetic field components in y direction (complex scalar)
$H_z(\omega, \mathbf{r})$	Magnetic field components in z direction (complex scalar)
$\mathbf{h}(\Omega)$	Co-polar complex amplitude gain of the receiving antenna pattern
$h_\theta(\Omega)$	Complex amplitude gain of the receiving antenna pattern, $\hat{\theta}$ polarization
$h_\phi(\Omega)$	Complex amplitude gain of the receiving antenna pattern, $\hat{\phi}$ polarization
h_t	Height of the transmitting antenna
h_{r_i}	Height of the ith receiving antenna
$\mathbf{h}_T(\theta, \phi)$	Transmitting antennas with complex normalized patterns in spherical coordinates
$\mathbf{h}_R(\theta, \phi)$	Receiving antennas with complex normalized patterns in spherical coordinates
$h_\theta(\Omega)$	Antenna patterns in $\hat{\phi}$ polarization
$h_\phi(\Omega)$	Antenna patterns in $\hat{\theta}$ polarization
I	Current
I_0	Current at the surface of the conductor
I_{max}	Current maximum
I_Z	Current distribution along z axis
l_m	Monopole length
$I_z(r)$	Current parallel to z-axis in distance r to the z-axis
J	Current density
J_0	Bessel function of the first kind, zeroth order
J_1	Bessel function of the first kind, first order
J_2	Bessel function of the first kind, second order
J_i	Number of ray components at the ith receiver along trajectory
k	Wave number, propagation constant
k_0	Air propagation constant
k_C	Wave number corresponding to frequency f_C
l	Dipole length
l_{mn}	Spacing between mth and nth receiving points
L	Integration distance for local mean evaluation
$G_{path}(d)$	Path gain at distance d from the transmitting antenna

λ	Wavelength
$m_i^{\theta\theta}$	Local mean at the ith receive
$\hat{m}_i^{\theta\theta}$	Estimate of local mean at the ith receiver
μ	Permeability
N_l	Number of turns of a wire loop
N_{Tx}	Number of transmitting antennas
N_{Rx}	Number of receiving antennas
n_k	Baseband noise powers at the kth antenna branch (out of the total $M_{ant} = N_{Rx} \times N_{Tx}$ branches)
ω	Angular frequency
ω_C	Carrier angular frequency
$\omega_C^{(L)}$	Loaded angular frequency
ω_{res}	Resonance frequency
ω_{BB}	Baseband (angular) frequency
ω_r	Radio (angular) frequency
Ω	Solid angle
Ω_D	Departure solid angles
Ω_A	Arrival solid angles
Ω_{Aij}	Arrival solid angle, corresponding to the jth ray component of the ith receiver
Ω_{Dij}	Departure solid angle, corresponding to the jth ray component of the ith receiver
σ	Conductivity of the conductor
P_L	Average power dissipated in the load (resistor)
P_R	Power received at the receiving antenna
P_T	Transmitted power
P_θ	Normalized power in $\hat{\theta}$ polarization
P_ϕ	Normalized power in $\hat{\phi}$ polarization
P_{ohmic}	Dissipated power in ohmic losses
P_{rad}	Radiated power of an antenna
$\Pi_{\omega_{BW}}(\omega_C;\omega)$	Rectangular filter centered at ω_C and with single sided bandwidth, ω_{BW}
ϕ_{Aij}	Arrival azimuth angle, corresponding to the jth ray component of the ith receiver

ϕ_{Dij}	Departure azimuth angle, corresponding to the jth ray component of the ith receiver
ϕ_{T_i}	Transmit azimuth angle of the line-of-sight for to the ith receiver
ϕ_{R_i}	Receive azimuth angle of the line-of-sight for to the ith receiver
q_k	Amplitude SNR for the kth antenna
q_C	Envelope of the combined signal
Q	Quality factor
Q_L	Loaded quality factor
Q_{Chu}	Quality factor, Chu bound
$Q_{Chu_{AC}}$	Quality factor, approximate formula
$Q_{Gustafsson}$	Quality factor, recent bound
Q_{Grimes}	Quality factor, Grimes bound
Q_{Hansen}	Quality factor, Hansen bound
Q_{Mclean}	Quality factor, McLean bound
$\mathbf{r}$	Position vector
r_i	Position along the trajectory at the ith point
$\rho_{012}(d, \gamma)$	Correlation coefficient between two patterns in terms of d and γ
R	Resistance
R_1, R_2	Distances to the both ends of the dipole
R_{in}	Input resistance
R_{rad}	Radiated resistance of an antenna
R_{ohmic}	Ohmic resistance of the dipole
R_e	Radiation resistance of an electric dipole
R_m	Radiation resistance of a magnetic dipole
RPF_e	Radiation power of an electric dipole
RPF_m	Radiation power of a magnetic dipole
$s_{r_i}^{\theta\theta}$	Summed field at the ith receiver, (θ-θ) polarization component
$\sigma_{\bar{b}}^2$	Variance of the mean (integrated) amplitude signal (summed rays for ray-traced data)
σ_b^2	Variance of the amplitude signal
$\sigma_{\bar{b}^2}^2$	Variance of the mean power
$\sigma_{b^2}^2$	Variance of the power
σ_{DSi}	Local delay spread at the ith receiver

τ_{ij}	Delay of the jth ray component of the ith receiver along trajectory
$\tau_{i_{LOS}}$	Delay of the line-of-sight ray traveling from the transmitter to the ith receiver
τ_{TOF}	Delay of the time-of-flight (time that takes for light to travel the direct line between two points)
$\bar{\tau}_{rms}$	rms delay spread
$\bar{\tau}_{DSi}$	rms (mean) delay spread at the ith receiver
θ_{Aij}	Arrival zenith angle, corresponding to the jth ray component of the ith receiver
θ_{Dij}	Departure zenith angle, corresponding to the jth ray component of the ith receiver
(θ_T, ϕ_T)	Zenith and azimuth angles of the signal in the spherical coordinates for transmitting antenna
(θ_R, ϕ_R)	Zenith and azimuth angles of the signal in the spherical coordinates for receiving antenna
θ_{T_i}	Transmit zenith angle of the line-of-sight for the ith receiver
θ_{R_i}	Receive zenith angle of the line-of-sight for the ith receiver
Υ^{-1}	Radius of the dipole in wavelength
V	Driving point voltage
$V_{\mathrm{O}}^{\theta\theta}(r_i, \tau)$	Time domain open circuit voltage at the antenna corresponding to the polarization component (θ-θ), at r_i
$V_{\mathrm{O}}^{\theta\theta}(r_i, \omega)$	Frequency domain open circuit voltage at the antenna corresponding to the polarization component (θ-θ), at r_i
$V_{BB}^{\theta\theta}(r_i, \omega_{BB})$	Baseband voltage corresponding to the polarization component (θ-θ), at r_i
W_e	Average electric energy
W_m	Average magnetic energy
$\hat{\mathbf{x}}$	Unit vector of the Cartesian coordinates along x-axis
$\hat{\mathbf{y}}$	Unit vector of the Cartesian coordinates along y-axis
$\hat{\mathbf{z}}$	Unit vector of the Cartesian coordinates along z-axis
X	Reactance
X_{in}	Input reactance
(x_t, y_t, h_t)	Cartesian coordinates of the transmitting antenna (i.e., base station)
$(x_{r_i}, y_{r_i}, h_{r_i})$	Cartesian coordinates of the receiving antenna (i.e., base station) at the ith receiver

Y	Admittance
$\mathbf{Y}_{r_i N_{Rx} \times N_{Tx}}(\tau)$	Received signal matrix at the ith receiver
y_k	Baseband equivalent signal voltage at the kth antenna branch
	(out of the total $M_{ant} = N_{Rx} \times N_{Tx}$ branches)
ζ	Positive direction axis of a straight line
(x, y, z)	Components of the Cartesian coordinates
Z_0	Intrinsic impedance
$Z_{antenna}$	Antenna impedance
Z_m	Input impedance referred to the current maximum
Z_{in}	Input impedance
$\hat{\theta}$, $\hat{\phi}$	Unit vectors of spherical coordinates corresponding to θ and ϕ polarizations

List of Acronyms

2D	Two-Dimensional
3D	Three-Dimensional
BW	Bandwidth
BTU	Braunschweig Institute for Communications Technology at Technische Universität Braunschweig
CAD	Computer-Aided Design
CDF	Cumulative Distribution Function
CRC	Communications Research Centre, Canada
DG	Diversity Gain
DS	Delay Spread
EGC	Equal Gain Combining
EM	Electromagnetic
EM Solver	Electromagnetic Solver
EMF	Electromotive Force
FDTD	Finite-Difference Time-Domain
FEC	Forward Error Correction
FEM	Finite Element Method
FIT	Finite Integration Technique
GD	Geometric Directivity
GIS	Geographic Information System
LOS	Line-of-Sight
MEA	Multi-Element Antenna
MIMO	Multiple-Input Multiple-Output
MRC	Maximum Ratio Combining

mm	millimeter
MOM	Method of Moments
M-QAM	M-Quadrature Amplitude Modulation
OTA	Over-the-Air
PDP	Power Delay Profile
QAM	Quadrature Amplitude Modulation
RF	Radio Frequency
rms	root mean square
RPF	Radio Power Factor
SC	Selection Combining
SINR	Signal-to-Interface plus Noise Ratio
SNR	Signal-to-Noise Ratio
TDL	Tapped Delay Line
TOF	Time-of-Flight

Part I

Theory of Dipoles and Array Factors

Chapter 1

Introduction

1.1 Motivation

Communications and sensing applications are continually moving to higher frequencies motivated by physically smaller antennas and larger electrical apertures for elements and arrays.

With fixed spectral constraints, the goal of the designer of any new communication system is to increase the capacity of the link over that of the previous technology. This goal is unlikely to be accomplished unless the efficiencies of the transmitting and receiving antennas at both ends of the link are optimized. In terms of a communications system, the antenna efficiency features directly in the antenna gain, so the signal-to-noise ratio (SNR), or more specifically for digital systems, energy per bit to noise power spectral density ratio (E_b/N_0) - the basic parameter for communications efficiency - is proportional to the antenna efficiencies.

The designer can increase the capacity of the link by increasing the antenna gain. However, to increase the antenna gain, the physical aperture of the antenna has to be increased. Using arrays and multi-element antennas (MEAs) allows the designer to increase the capacity of the link by either higher gain, or else through interference suppression.

The MEA is used as an adaptive matched filter, and so the spatial and temporal agilities of the adaptive antenna are important. Signal processing allows the MEAs to use the transmission medium more efficiently. By knowing the physical structure of the wireless channel, either from modeling and simulation or from physical measurement, the signal processing strives for maximum capacity. It is fundamentally important to match the antenna configuration to the propagation channel characteristics.

Multiple-input multiple-output (MIMO) is not used to its potential in current systems because its large-scale implementation (where the large spectral efficiency cuts in) is not sufficiently understood for commercially feasible deployment. Even the performance evaluation of a well-defined MIMO configuration remains very limited and so new evaluation techniques need to be developed. The evaluation of the antenna performance in urban environments, where the wireless traffic is at its highest, is particularly important for being able to plan and design high spectral-efficiency systems.

Small-scale MIMO systems are in operation, but larger-scale MIMOs are needed for long term performance requirements. To date, there is a noticeable distance between the theoretical performance of communications systems and their practical performance. For example, the achieved throughput is far from the theoretical limits. Subsequent systems will contain a larger number of antennas and should operate closer to their theoretical performance. To implement large-scale MIMO systems, new and more elaborate technology is needed.

Another challenge is the MEA antenna efficiency. The antenna efficiency affects the cost of the whole communications network as well as its efficiency. Recently, the energy cost of the wireless systems, as a limiting communications issue, has been studied, e.g., [1]. A dB power loss in a single handset antenna significantly affects the cost of the large wireless network. The radio efficiency of most commercial handsets is known to be as low as -12dB [2].

To explain how a communication system works and to evaluate and therefore to see how the performance is improved (such as optimizing its capacity), a joint understanding of the antennas, the propagating channel and the signal processing is needed.

In this thesis, fundamental aspects are addressed in:

- antenna elements
- antenna arrays and MEAs
- signal processing for wireless propagation channel

These are introduced in this chapter and the first two topics are developed in **Part I** and the last topic in **Part II**.

1.2 Antenna Elements

1.2.1 Aspects of Antenna Elements

The electric dipole and magnetic dipole are the most fundamental, also practical, antenna elements. The electric dipole (for which, in terms of language simplicity, the term "dipole" is used) is studied in detail.

The impedance of an antenna is a classical topic. For a simple implementation, measurement can be made with a single port vector analyzer, and the accuracy can be enhanced using averaging in the usual way. But an impedance measurement includes the radiation resistance together with the ohmic resistance. Separating these components accurately is difficult.

In **Part I** of this thesis, the most popular numerical techniques and all the readily available theories for evaluating the impedance of the dipole are used. The results have been employed to interpret the quality factor (Q) and impedance bandwidth of a short dipole, i.e., with the length around a half wavelength. A benchmark is provided for the impedance of a dipole with and without an excitation gap [3, 4].

The two available theories for dipole impedance are the wave structure method and the induced EMF method. These two theories are developed and applied for the impedance of a dipole. Numerical methods are also used for practical dipole thicknesses to calculate the dipole impedance.

The quality factor relates to the theoretical impedance bandwidth of an antenna. Such a bandwidth could only be realized using an ideal, i.e., lossless and perfectly matched, network to interface the antenna to its terminating resistance. The Q is therefore particularly useful for deriving the limiting bandwidth of fixed, compact antennas. The Q factors of short dipoles are calculated from different analytical and numerical methods.

The bounds on Q have also been studied. These bounds include the conventional bounds, e.g., the Chu bound [5], and the recent bound by Gustafsson et al. [6], as well as the several bounds from the theories and numerical methods for dipoles [7].

Antenna impedance parameters are used for evaluating multiport antennas for diversity/MIMO, under the convenient assumption that the antennas are lossless. (Recently, a formulation which includes the losses has been proposed [8].) This assumption is reasonable for low frequencies (where the elemental loss is not zero, but can be very low) but does not apply to emerging, higher frequencies such as 60GHz. These millimeter-wave (mm-wave)

frequencies are renewing interest in understanding and quantifying antenna efficiency. The efficiency formulations are reviewed for wire antennas, and a benchmark efficiency is developed for the half wavelength dipole [9].

1.2.2 Electrically Small Antennas

The term of *electrically small antenna*[1] was firstly defined by Wheeler [10] in 1947 as an antenna that could be enclosed within a radian sphere. The radian sphere has a radius of $\lambda/2\pi$, where λ is the wavelength. The early antennas were all electrically small because of the low frequency [11]. The antennas used by Marconi and Fessenden in early years of wireless communications (mostly for telegraphy) were electrically small antennas despite their very large physical structure [11].

All the electrically small antennas have some common characteristics that limit their performance. These characteristics are [11]:

- low radiation resistance
- high reactance
- low efficiency
- narrow bandwidth
- high loss in matching network

The radiation power factor (RPF) is an old figure of merit for the electrically small antennas introduced by Wheeler [10] and is defined as

$$\text{RPF} = \frac{\text{radiation resistance of the antenna}}{\text{reactance of the antenna}}. \tag{1.1}$$

For an electric dipole of length l and with capacitive loading at each end through conducting disks of radius a, the radiation resistance and the capacitance between two plates, in distance l to each other, are given by $R_{rad_e} = 80\pi^2(l/\lambda)^2$ and $C = \epsilon_0\pi a^2/l$, respectively. For the magnetic dipole (realized with a wire loop) with N_l turns, length l, and radius a, the radiation resistance and the approximate inductance are $R_{rad_m} = 320N_l^2\pi^6(a/\lambda)^4$ and

[1] This subsection is mainly adapted from [10–12].

$L = \mu_0 N_l^2(\pi a^2/l)$, respectively. For these two basic antennas, the radiation power factors follow respectively as:

$$\mathrm{RPF}_e = R_{rad_e}\omega C = \frac{4}{3}\frac{\pi^3 a^2 l}{\lambda^3}, \tag{1.2a}$$

$$\mathrm{RPF}_m = \frac{R_{rad_m}}{\omega L} = \frac{4}{3}\frac{\pi^3 a^2 l}{\lambda^3}, \tag{1.2b}$$

where ω is the angular frequency. These radiation power factors are related to another figure of merit, the Q parameter, which, for a resonating circuit is defined as:

$$Q = \frac{\omega(\text{average energy stored in resonant circuit})}{\text{average energy dissipated per second}}. \tag{1.3}$$

The advantage of the Q is that it can be related to a simple circuit model. For an RLC circuit (with an inductor of L in series with resistance R) with current I, the magnetic energy stored in the magnetic field of the inductor and the average power dissipated in the resistor are given by $W_m = I^2L/4$ and $P_L = I^2R/2$, respectively. Then the Q can be expressed as

$$Q = \frac{\omega L}{R} = \frac{2\omega(I^2L/4)}{I^2R/2} = \frac{2\omega W_m}{P_L} = \frac{\omega(W_m + W_e)}{P_L}. \tag{1.4}$$

Q is approximated (exact for RLC circuits) as

$$Q \simeq \frac{\omega dX/d\omega}{2R}. \tag{1.5}$$

Here it is assumed that the derivative of equation (1.5) is always positive. The Q can be used for limits of bandwidth of small antennas, and in general, for all antennas. The Q of an antenna is a direct indication of the relative bandwidth of an antenna [12], it is a cornerstone parameter of the treatment of the dipole in this thesis.

1.3 Antenna Arrays

There is no methodology for the design of compact MEAs suitable for the three-dimensional (3D) nature of the propagation in mobile communications. The only classical guidelines available for design are from array theory, where elements are often placed about a half-wavelength apart, or more, in a trade-off between fully sampling the space (an element spacing of a half-wavelength or less) and minimizing the mutual coupling (as large a spacing

as possible). The difference between an array and an MEA is laid out in [13] [2].

Arrays are normally used to help direct the antenna pattern, including minimizing it for unwanted directions, such as those featuring interference, or maximize gain in a wanted direction.

Two-element, and three-element linear and circular arrays, are convenient for analytic study. Motivated by designs for mobile communications antennas, or fixed arrays operating in dense multipath, the interest is in the relationship between the phase shift (weight) and the element spacings for array patterns that are orthogonal to the pattern of the array without any phase shifter (i.e., a zero phase, or some other fixed reference phase value). Such beamformed patterns can be deployed for diversity/MIMO. Pattern-reconfigurable antennas that are simple, are in particular demand for MIMO communications.

When the radiation coverage of the antenna is full, i.e., covering the whole sphere, the correlation coefficient between the antennas determines their mutual coupling, e.g., [14]. For spherical coverage or hemispherical coverage (uniform and some special case functions), there is a closed form solution to the pattern correlation integrals. But for partial coverage, the integration requires numerical methods.

In this thesis, the formulations are provided, and the results for the arrays of isotropic and dipole antennas are included. Also, the directivity of the two-element linear array factor is presented, demonstrating interesting and unintuitive results from even the simplest array.

Mutual coupling is not explicitly considered here. For most of the configurations of interest, a sufficiently large element spacing is the main configuration of interest, meaning that the mutual coupling can be neglected.

1.4 The Analogue Path to Digital Communications

The ultimate goal of a wireless communications system is to provide high-throughput of digital data, e.g., [15]. The required communications techniques are well established, and this aspect is not in the scope of this thesis. Nevertheless the link between the physical channel and configuring the digital communications techniques remains problematic, especially for optimizing the design of a communications system. This is because the performance metric

[2] In short, array antennas are special cases of MEAs, with identical and usually equally spaced elements. MEAs might include different elements which can be placed in any arbitrary orientations or distance from each other.

(actual throughput and bandwidth usage in a multiple user system) of a practical digital communications system is too complicated to directly optimize. The digital communications parameters must be optimized indirectly, using idealized, often information-theoretic metrics, instead of practical metrics. To optimize the digital communications parameters, the physical channel is represented by a complex signal which can be transformed to represent the instantaneous SNR, or signal-to-interference plus noise ratio (SINR). This signal is a vector for MIMO communications.

Part II of this thesis primarily concerns the generation and processing of this signal. The signal performance metrics for multiple antenna systems are optimized by setting the weights of the antennas. An antenna weight can be just a simple number, or scaling, for narrowband communications, but for general wideband channels, it would be a tapped delay line (TDL).

The MIMO works by the digital communications systems adapting to the varying channel. In a general configuration of MIMO communications, the channel must be sounded and the information interchanged between all of the users, and so a supporting protocol is needed for this. The protocol consumes the available spectral resources and so it should also be adaptive in order to avoid unnecessary sounding of the channels (i.e., unnecessarily using the spectrum for sounding instead of transmitting data payload) that have not changed significantly.

For high capacity, or spectral efficiency, the modulation must be adaptive, and the data coding, such as forward error correction (FEC), can be adaptive as well. The situation for digital communications is summarized in Figure 1.1. Figure 1.1 shows the 7-10dB minimum capacity penalty which is the result of using uncoded M-QAM and finite block codes. Here, the use of just one digital modulation constellation is seen to have a very small range of SNR just a few dB - where it is closest to the information-theoretic capacity, e.g., [16]. But typical single-antenna wireless systems experience fluctuations of several tens of dB over short distances, and perhaps a hundred dB over a longer trajectory. Figure 1.3 illustrates a calculated SNR along a trajectory of about 1100 wavelengths in Downtown Ottawa. The trajectory of the mobile receiver is shown in Figure 1.2 with a red line, and the transmitter is shown with a red dot. The physical modeling of this urban scenario has been performed by Communications Research Centre of Canada (CRC). The maximum fluctuation of the signal power along the trajectory is over 90dB, and for a distance of 100λ (i.e., 30m), the fluctuation of the signal power exceeds 60dB. From Figures 1.1 and 1.3, it is inferred that by

sticking to one modulation, staying close to its information-theoretic limit is not possible. Using variable (different) coding rates shifts the capacity curves of Figure 1.1 by a few dB, especially where the (single channel) SNR is in proximity of the Shannon bound. But the coding does not move the capacity curves closer to the Shannon capacity.

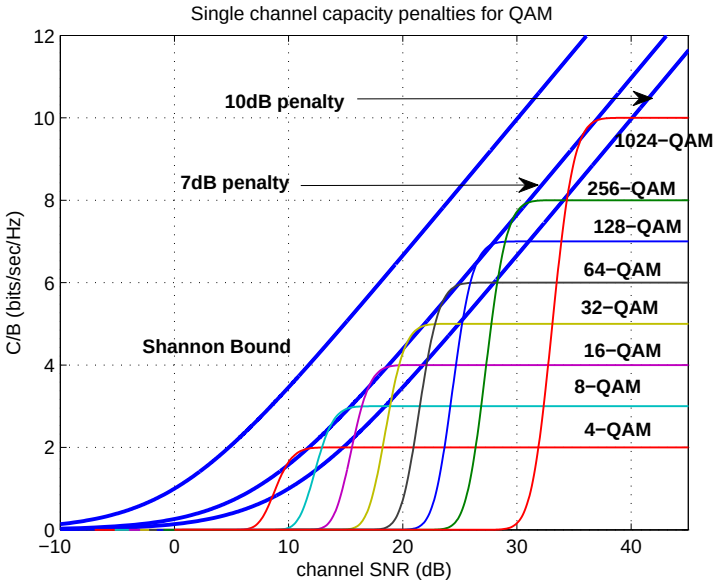

Figure 1.1: Penalties of the single channel practicable capacity for M-QAM (quadrature amplitude modulation) versus single channel SNR using non-adaptive modulation.

The performance metrics in digital communications are usually an information-theoretic capacity, such as the Shannon capacity, and an error rate. The two often work against each other which explains the need for both. The practical problem with the information-theoretic type capacities is that they refer to a transmit situation, i.e., they give a limit for how much information can be transmitted, rather than how much can be detected. In practice, it is of more interest to understand the receive possibilities. To this end, a practicable capacity is of interest, for example, based on the rate of correctly detected bits at the receiver. Such a metric therefore combines an information-theoretic capacity and the error rate. A practicable capacity and an information-theoretic capacity behave differently in optimization, so optimizing the digital communications system for an information-theoretic capacity is unlikely to be optimum for a practical system. But a general practical system is too complicated to optimize, and consequently the default approach is to optimize multi-user

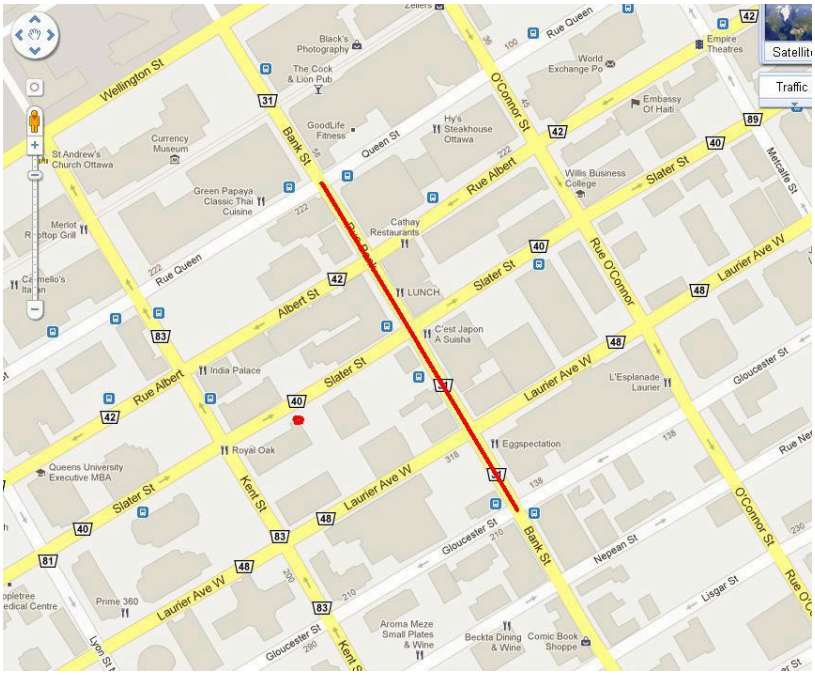

Figure 1.2: The receiver trajectory and transmitter location for the CRC simulator, Downtown Ottawa, ON (from [17]).

MIMO systems based on an information-theoretic capacity along with an error rate for a single modulation, and with no coding. This is very different from a practical configuration.

This situation leads us to optimize multiple antenna systems using analogue metrics, e.g., SNR, and take the chance that such an optimization will be reasonable for getting high spectral efficiency, no matter how the digital communications parameters are derived and optimized. So the antenna signals are treated as being combined before the detection and other processes of the digital communications. These signals are referred to as analogue in order to differentiate them from a discrete bit- or symbol-based quantity. But they are likely to be implemented in digital form, i.e., in an adaptive antenna the signal combining can take place after digitization, but before detection. A reduced-cost system can employ some form of analogue combining or antenna reconfiguration, which has fewer radio frequency (RF) chains.

Figure 1.3 also shows the distance between the transmitting and receiving antennas (red dashed line) and the received SNR along the trajectory. The SNR is higher for the part of the trajectory which is closer to the transmitter and especially where there is a line of sight,

see Figure 5.3.

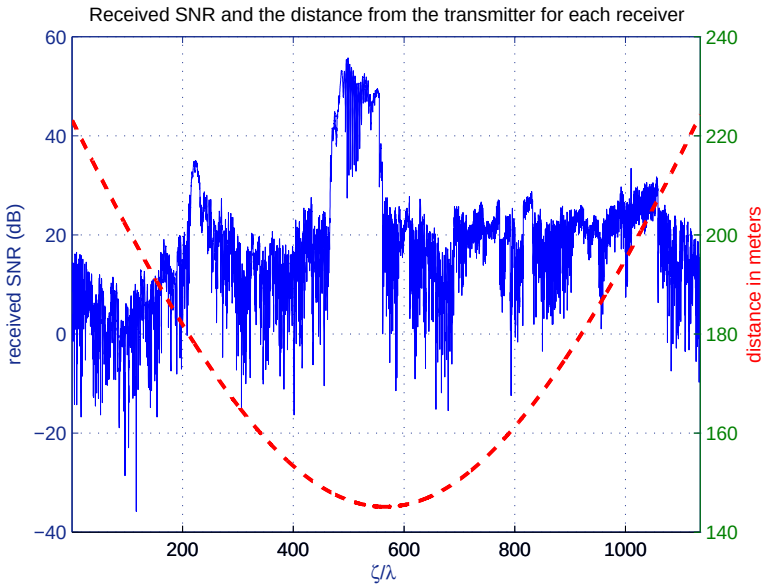

Figure 1.3: The received SNR (solid line), and the distance (in meters) between each receiving point and the transmitter (dashed line), against antenna positions in wavelengths, ζ/λ , see Figure 5.3.

1.5 Signal Processing: Analysis of the Physics-Based Simulation

1.5.1 Channel Signal Generation

Different methods have been used to generate channel signals for evaluating digital communications by MIMO. For example, physical measurement is the method that records and stores the channel signals in time (or distance), whereas statistical generation of the channels allows for convenient, repeatable channel signals with precise and statistically controlled parameters.

The advantage of the stored channel is maintaining the ground-truth nature of the signal. But the antennas cannot be changed once the physical measurement has been undertaken,

and a new measurement is required for a different antenna or a different environment. Physical experiments can seldom be exactly repeated owing to changing environments and interference conditions. Reverberation chambers offer one approach but the spatial conditions are seldom well related to real-world conditions.

For the purely statistical channel approach, there is difficulty in changing the types of antennas or environments in the sense that the relationship between the statistically generated signals and the antenna configurations is nontrivial, so the approach is not directly suited to adaptive antenna design.

The physical modeling is in many ways a combination of the above techniques for the channel signal generation process, e.g., [18,19]. The ray-tracing is a robust physical modeling technique and its data may be applied to different antennas, *cf.*, the two-dimensional (2D) double-directional channel [20]. The interest here is in the three-dimensional (3D) channel, but the principles are the same.

Different ray-tracers use different techniques. For example, one tracer may calculate up to 8 planar reflections only and up to 10 rays only, while another may instead calculate rough surface reflections and diffractions up to the number where the contributions are less than say 160dB below the transmit level. This means that different simulators will give different channels for the same geometry or environment data file.

The simulated channel data have been provided to us by two different research centers, the Communications Research Centre Canada (CRC) and the Braunschweig Institute for Communications Technology (BTU). Different ray-tracing techniques are used by the two simulators.

1.5.2 Channel Parameters for a Physics-Based Simulated Channel

The physics-based simulated data of the wireless channel provides more flexibility compared to the measured channel data. Here, the interest is restricted to the issues of the channel parameters, such as local mean, power delay profile (PDP) and delay spread (DS), angular spread and channel correlation. Examples of effects of the averaging, time-alignment, filtering and sampling (binning) are presented.

Physics-based simulation, i.e, ray-tracing, is still limited, but can be expected to improve as extra terms from the scattering processes become incorporated and conveniently calculable. The following goals are sought from the ray-traced channel data files:

- extraction of the mobile channel from physics-based simulation and its pitfalls,
- characterization of the mobile channel based on the extracted signal,
- signal use for communications applications performance evaluation,
- extraction of modeled communications detail, i.e., tapped delay line.

1.5.3 MEA Performance Evaluation in a Ray-Traced Channel

A design method is presented to estimate the performance of a multi element antenna in a typical wireless channel. For simplicity, a basic diversity system is considered. But the methodology can be used for scenarios with any number of antennas with arbitrary patterns, arbitrary 3D environments, interference, and arbitrary communications techniques.

The approach includes the modeled physical environment, and this is different from the idealized channels of statistical models, e.g., [21], and of reverberation chambers e.g., [22,23]. This is a flexible software approach with full control of the modeling parameters and the potential of embedding the information of the sounded channel.

This method is the most powerful available for design and planning, and has the potential to become a standardized technique for the evaluation of large-scale MIMO systems required for future wireless communications.

1.6 Summary of Contributions

The theoretical Chu bounds for the thin electrical dipole with excitation gap is new and has not been researched before. The results for the ohmic loss of a dipole are new and topical, considering the industrial trend to higher frequencies, e.g., the millimeter-wave frequencies typically above 60GHz. The incorporation of ray-traced channel for MEA performance evaluation is new and has not been treated before.

The contributions of this thesis include:

- comparing the results for the impedance from different solution techniques (reported in Chapter 2 and published in [4]),
- comparing the theoretical impedance methods for a zero gap dipole (reported in Chapter 2 and published in [3]),

- establishing new Q bounds and bandwidth limits from theory, simulation and measurement (reported in Chapter 3 and published in [7] and presented in [24]),
- reviewing the most significant works on the impedance evaluation of the dipole, implementing the model in different numerical solver softwares, using an old theoretical technique and developing it for the impedance of a dipole with excitation gap (reported in Chapter 3 and published in [25]),
- evaluating the dipole antenna ohmic loss and therefore radiation efficiency from a theoretical approach (reported in Chapter 3 and published in [9]),
- deriving the orthogonality conditions between array patterns in terms of the spacing and the phase shift (reported in Chapter 4 and published in [26]),
- estimating the power delay profile and delay spread for the ray-traced channel (reported in Chapter 6 and published in [27]),
- evaluating the performance of an MEA from physics-based simulation in a diversity link (reported in Chapter 7 and published in [28]).

1.7 Thesis Layout

The thesis has eight chapters. **Part I** contains the introduction and three other chapters and **Part II** contains four chapters where the last one is conclusions and suggestions for future works.

- **Part I:** Theory of Dipoles and Array Factors (**Chapter 1**, **Chapters 2**, **3** and **4**)
  - **Chapter 1** has introduced the theme of the thesis. The motivation for the problems addressed and the objectives and contributions of this work are summarized.
  - **Chapter 2** summarizes the significant works on dipole impedance and studies the solution techniques for impedance. The theories and numerical solutions are applied for the impedance of a center-fed electric dipole with and without excitation gap.

- **Chapter 3** presents the results for Q factor and bandwidth of the thin dipole antenna from different theoretical and numerical methods. The remainder of **Chapter 3** discusses the ohmic loss for the electric dipole. The ohmic loss is calculated for a half wavelength dipole.
- **Chapter 4** addresses phased-array antennas. The spaced elements such as dipoles with fixed beamformers for pattern orthogonality are studied. The modeled correlation coefficient between antenna patterns is considered as the metric for quantifying the orthogonality.

- **Part II:** Multi-Element Antennas with Physics-Based Propagation for Mobile Communications (**Chapters 5**, **6**, **7** and **8**)
  - **Chapters 5** introduces methods for evaluating the wireless propagation channel and discusses the limitation of each method. The signal processing is addressed for physics-based simulations (as opposed to statistical simulations of communications channels, or electromagnetic (EM) solvers for antennas) for channel and diversity evaluation.
  - **Chapter 6** offers physics-based simulation (ray-tracing) of radio channels as a powerful technique for propagation analysis and estimation of channel parameters. These simulations are not discussed, but some of the processing is addressed which is required to synthesize channels that have similar properties to physically measured ones.
  - **Chapter 7** incorporates the ray-tracing in order to evaluate the MEA performance in a wireless channel. The performance metric is the diversity gain. The results are presented for a typical urban scenario and a random MIMO antenna.
  - **Chapter 8** summarizes and concludes the thesis and proposes some future works for this research.

Chapter 2

Impedance of an Electric Dipole

2.1 Motivation for Research on Dipole

The dipole is the fundamental elemental antenna and the wire electric dipole and its monopole equivalent are still widely used in practice. Despite the long history of dipole research, its complete impedance behaviour remains elusive because of long-standing shortfalls in modeling the feed.

There are several analytical and numerical methods to treat the impedance of the wire dipole. The available analytic approaches are the wave structure method and the induced EMF method. The wave structure method does not lend itself to feed gap detail, but reveals the impact of dipole thickness and length on the impedance of dipoles which is not readily available from other approaches. It is restricted to an infinitesimal feed gap, i.e., different from a practical dipole antenna. The induced EMF method is accurate for short and impracticably thin (for self-supporting) wire antennas. Numerical techniques can be used for practical dipole thicknesses, but no theory is available to benchmark the results.

This chapter includes a review of previous work to acknowledge the rich history of dipole research and provides context for current research; as well as new analysis and new impedance results for a range of dipole lengths. In summary, this chapter contains the following subjects:

- brief review of the classical work on dipole impedance/admittance (see Sections 2.2 and 2.4),
- study of numerical solutions for dipole impedance, with new results for a finite feed

gap of size less than a tenth of a wavelength (see Section 2.3 and Section 2.6),

- modification to the induced EMF method for the impedance of the dipole with a feed gap (Section 2.5.1).
- comparison of the impedance results from different numerical and theoretical techniques, with new results for the impedance of the finite gap dipole (Section 2.6). This type of comparison has not been published before.

2.2 Dipole Impedance and Feed Excitation as Longstanding Problems

The wire dipole is particularly practical at its resonance length of about a half wavelength not only because of its simplicity, but also because its radiation resistance lends itself to matching and baluns. The accurate modeling of the feed remains a challenge in both antenna-theoretic and practical senses. A gap voltage feed can be expected to give a well-defined radiation conductance, but a susceptance which is dissimilar to that of a realized antenna; whereas an impressed current feed can give a well-defined radiation resistance, but dissimilar reactance. The reason is that neither of these feed configurations accurately model the input region of a practical dipole. The bandwidth is governed by the reactive part and so the modeling of the feed region is important for understanding basic dipole behavior, including bandwidth limits.

It is convenient to refer to the feed as having no gap (for current excitation), an infinitesimal gap (for voltage excitation), or a finite gap. The finite gap allows a voltage feed and seems suitable for a transmission line feed, or a direct connection to a balun. The infinitesimal gap is widely used for numerical feed modeling, but the no gap and finite gap cases relate better to practical situations. However, from an antenna-theoretic viewpoint, the transmission line, balun, etc., are not modeled, a central assumption with antenna feed region treatment for feed point impedance calculation.

In the last couple of decades, commercial electromagnetic/antenna packages for simulation have prevailed for analysis and design of antennas. Different packages lead to different impedance answers, and there is seldom a checking benchmark (at least for dipoles) for the results of these solvers. In any event, the numerical solvers rely on the mathematical models, so understanding the accuracy of the underlying models maintains a relevant and important

role in antenna theory. In this research, different simulation packages have been used, such as: WIPL-D [29]; NEC [30]; CST Microwave Studio [31]; HFSS; and an FDTD [32, 33] method, *viz.*, [34]. These results are checked against those of the induced EMF method. The numerical simulations were submitted to all the vendors and the WIPL-D and HFSS results were confirmed by their customer support.

The different theoretical models also produce different theoretical impedance results, although for the half wavelength dipole with no gap, the results from the wave structure [35] and the induced EMF methods, concur well [14]. For the infinitesimal feed gap case, the results agree with known results, e.g., [36–38].

For a transmission line feed, the problem of gap impedance evaluation has been tackled from different theoretical approaches, e.g., [39, 40]. However, the impact of the gap size on the dipole impedance has not been previously treated. Also, the modeled loss for different conductors are included since this affects the resistance at higher frequencies, e.g., for the recently approved mm-wave bands.

While the principal interest is in theoretical limits of the dipole structure, rather than the results from commercial solvers, some results from commercial solvers are nevertheless included. The benchmark results for the impedance bandwidth of the thin dipole with a sinusoidal current distribution are theoretical, from a modified induced EMF method.

2.3 Background on Dipole Impedance

2.3.1 Background: The Input Region at the Terminals of a Dipole

Schelkunoff [41] seems to have been the first to address the feed region, or 'input region' of a dipole – the region of transition between the feed line and the antenna. The detail of this region has a dominant impact on the reactive component of the input impedance or admittance, as also noted in [42]. Schelkunoff offered little elaboration on the input region, but it has since become well established that the feed configuration affects the input impedance of most antennas e.g., [36, 43, 44], including the dipole. The feed configuration in turn affects the modeled performance of any communications or sensing system that uses the antenna. This is because errors in the modeled impedance calculation lead to a (modeled) mismatch which is different to the implemented mismatch.

Because of the inaccurate modeling of the input region used by theory and simulation,

the practical design of dipoles – and other elemental antennas – normally sees theoretical considerations discarded in favour of a cut-and-try (numerical and physical) approach. Achieving resonance and matching is seldom a design problem for wire of printed dipoles, but the bandwidth of most designs appears to fall well short of the theoretical limits presented below. This adds to the motivation for an ongoing look at the input region of the basic dipole using an antenna-theoretic approach, and to compare the results with existing solution techniques. Here, the ensuing theoretical impedance bandwidth is of primary interest.

In a practical situation, there is a gap between the dipole feed terminals. These terminals are usually connected directly to a transmission line. The transmission line detail is not addressed here except for the following comments. A pair of conductors forming a free space transmission line at right angles to the dipole (in order to minimize their impact on the dipole radiation and impedance characteristics) can be used, and this configuration has traditionally been also used for practical reference dipoles, e.g., [45]. Owing to the small electrical distance between the transmission line conductors, such a transmission line is restricted to a characteristic impedance of more than about one hundred ohms. Another practical architecture is a balun within or near the input region and connected to a coax line , e.g., [46]. The coax can be at right angles to the dipole. An alternative is a sleeve balun but this does not readily allow for either thin conductors which need mechanical support or a finite feed gap.

For physical measurements, the equivalent monopole on a groundplane is more convenient than the dipole. The monopole allows a direct coaxial feed through the groundplane or else connection to a planar transmission line on the groundplane. A very large groundplane is required if the impedance is to be compared with high accuracy to theoretical dipole results [47]. The monopole feed can be modeled either by an impressed current in the wire at, or close to, the groundplane position, or by a magnetic frill at the groundplane position with a size associated with the coaxial conductor spacing. Here, the dipole cross section is circular corresponding to a wire construction.

There is a capacitance arising from the feed gap, classically given by $\epsilon\frac{A}{\delta_g}$, where the permittivity in the gap is ϵ, the area of the conductors is A, and δ_g is the gap size. The reactance component from this capacitor changes with frequency of course, and the infinitesimal gap size is problematic in the sense that the capacitance becomes infinite. However, these capacitance problems can be averted if the arms of thin dipoles are separated by a

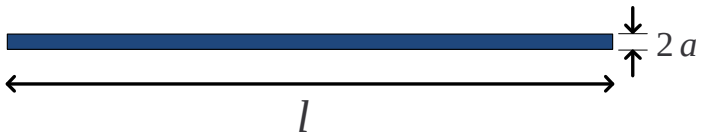

Figure 2.1: A wire dipole, with length l and radius a. This configuration is suitable for induced current excitation or excitation through a magnetic frill.

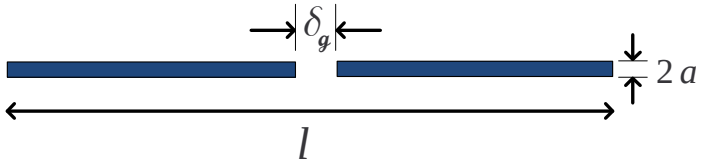

Figure 2.2: A wire dipole, with length l, and radius a and feed gap size δ_g. This configuration is suitable for voltage excitation.

relatively large gap, i.e., when $\delta_g >> a$, where $a = \sqrt{A/\pi}$ is the radius of the wire; and this is the configuration of interest here. In [48,49], an alternative gap capacitance for a uniform field distribution in a small gap is presented, and this is used in [42] for the impedance of the dipole of lengths of $0.2\lambda \leq l \leq \lambda$. For thin wires with small gap, i.e., $ka << 1$ (k is the wavenumber) and $\delta_g << a$, the same capacitance expression is assumed to be accurate in [50, 51].

Diffraction effects from the thin wire ends are not calculated explicitly. Any such effects are an implicit part of the thin wire formulation. Local effects from the truncated open ends of the dipole are ignored, although the end-cap currents are mentioned below.

Figure 2.1 and 2.2 show wire dipoles of length l, radius a and cross section area A. Figure 2.1 is a dipole without feed gap, e.g., excitation via magnetic frill, and Figure 2.2 shows a center-fed dipole with feed gap size δ_g.

2.3.2 Solution Techniques for the Impedance

Numerical methods include the method of moments (MOM) [29], finite-difference time-domain (FDTD) [32, 34], and finite integration technique (FIT) [31].

The MOM finds the discretized current distribution, but most results demonstrate that for thin wires, this current is very close to the sinusoidal form usually assumed for the induced EMF method. Discretizing the wire to an increasing number of smaller segments, does not necessarily bring greater accuracy, e.g., [52]. The MOM is well suited to wire

antennas, but the available commercial packages seem to maintain a current in the gap feed, e.g., [29]. Moreover, the associated boundary conditions along the gap are not clear but are treated as a wire, since while using the packages, it is necessary to specify a wire size for the feed gap. The algorithms and assumptions used in commercial packages are seldom available to the user.

The FDTD and FIT methods are sensitive to a large range of structural dimensions. In particular, a very thin (relative to its length) dipole creates such dynamic range related problems.

As noted above, there is insufficient information about the configurations, assumptions and algorithms supplied with most of commercial EM solvers, to be able to comment in detail on any expected shortcomings.

Physical measurement is another approach to find the dipole impedance and in some ways this is the ultimate test of accuracy of the models and solutions. But de-embedding the practical factors such as the balun and/or transmission line, the limitations in determining exactly the lengths of the thin wire, or the need for a very large groundplane for the monopole configuration, all act to compromise the precision of physical measurements of the stand-alone dipole. The configuration of the large gap dipole is a challenge to implement, and this is put aside in order to establish the theoretical bandwidth performance of the structure.

The theoretical methods are the wave structure method and the induced EMF method. The wave structure method is based on solutions for the waves on the semi-infinite wire [35], and as such it does not directly account for the input region. The current distribution is close to sinusoidal. The impedance results seem to be reasonable for dipole lengths greater than about 0.4λ [14].

The induced EMF method, which requires a modeled current distribution, is otherwise rigorous but it is well-suited only for impractically thin (in the sense of the conductor being self-supporting) wire antennas. The current distribution is usually taken as sinusoidal and this is regarded as acceptable for a thin wire antenna [37, 44]. Other current distributions include triangular, e.g. [53, 54], and the calculations (using current distributions drastically different from sinusoidal, *viz.*, triangular) indicate that this choice does not significantly change the quality factor behavior (see Chapter 3) which gives rise to the remarkable theoretical bandwidth of the thin dipole.

Below, reference results are presented for the impedance of wire dipoles with a finite gap, using a modified induced EMF method. The results are also useful for getting insight into

the bandwidth by using the quality factor. The integral formula is simple but its solution is not trivial. The induced EMF method is reported [55] without elaboration to be valid only when the length of the center-driven antenna is not much larger than a half wavelength, but here the wider band results are included, *viz.*, for dipole lengths of $0.2\lambda \leq l \leq 0.7\lambda$. An increasing (but still small) feed gap size makes the reactance curve flatter, leading to an increased bandwidth.

Silver [56] notes that when the gap is large, the current distribution along the arms of the dipole deviates from the sinusoidal distribution, while for an infinitesimally small gap the current can be assumed sinusoidal. But the statement is without elaboration and the context is that a "large" gap would imply a zero current at the feed position. It is known that the current on a long thin wire in free space must be sinusoidal, e.g., [52], and here it is assumed that it is non-zero at the feed end. In this sense, the electromagnetics of the feed detail that is not part of the dipole itself, is omitted from theoretical formulations.

As noted above, the main interest is in short dipoles, here meaning around a half wavelength. Their radiation resistance (around 70Ω) allows identification with standard coax cable characteristic impedances (50Ω and 75Ω) and the impedance bandwidth for termination with these values is also presented below.

In Table 2.1 some established methods for the impedance and the associated ranges of valid dipole lengths and thicknesses are summarized [4]. Besides the dimensional range limitations, there are other shortcomings in each of these methods. Perhaps the most important challenge is the definition of the excitation in the finite gap. For example, in WIPL-D the excitation configuration is described as a metallic apex [29] while in CST the excitation appears to use a variety of configurations (ports) for a voltage excitation.

impedance methods	**range of l**	**range of a**
induced EMF method	$l \leq 0.8\lambda$	$a \leq 10^{-2}\lambda$
wave structure method	$l \geq 0.4\lambda$	$a \geq 10^{-7}\lambda$
MOM (WIPL-D)	any l	$a \geq 10^{-3}\lambda$
FDTD (HFSS)	any l	$a \geq 10^{-3}\lambda$
FIT (CST)	any l	$a \geq 10^{-2}\lambda$

Table 2.1: Range of applicability of different methods for impedance, in terms of dipole length l and radius a [4]. These ranges are developed based on extensive numerical simulations and calculations, considering the dynamic range, the convergence of the technique, etc.

2.4 Some Works on Dipole Impedance Evaluation

The dipole impedance problem is longstanding. There has been almost a century of research on the wire dipole but few articles have addressed the dipole with a finite gap. In this section, a short overview is provided for some of the classical approaches to the impedance/admittance of a center-fed dipole antenna. It is divided into methods that did not treat the finite gap feed excitation, or provided the results for a given/fixed terminal condition; and those which tackled the effect of the gap.

2.4.1 Impedance of a Dipole without Gap

- In 1932, Carter [57] formulated an induced EMF method for finite length, thin wires (i.e., usable for dipoles) with an infinitesimal feed gap.
- In 1946, the King-Middleton iteration procedure [58] was published, giving the input admittance of the thin dipole.
- In 1956, Hallén [59] provided an exact treatment of antenna current wave reflection at the end of a cylindrical antenna.
- In 1962, Chen and Keller [60], and Fante [61] provided an analytical expression for the susceptance of an infinite dipole by considering the effect of a very small gap, with results being suitable for infinitesimal gaps.
- In 1965, King and Wu [62] presented their three-term approximation theory for the current distribution along an antenna of less than a wavelength long.
- In 1967, Andersen [35] presented the analytic wave structure method.
- In 1968, Shen, King and Wu [63] presented a simple formula for the current distribution in dipole antennas with infinite, semi-finite and finite length. The form was based on $I_\infty(z) = \frac{2jk}{\zeta_0}\int_{C_0}\frac{e^{j\zeta z}}{(k^2-\zeta^2)\tilde{K}(\zeta)}d\zeta$. This provided a relatively simple current distribution, and its accuracy was shown to be in good agreement with the experiments of Mack and Chen [64], for $\frac{l}{\lambda} \geq 0.3$, a similar range as the wave structure method.

- Also in 1968, Jordan and Balmain [65] showed that the induced EMF method is equivalent to integration of the Poynting vector on the cylindrical surface aperture of the dipole [45].

2.4.2 Impedance of a Dipole with Gap

- In 1956, King [40] analyzed the effect of the gap dimension on the admittance of a thin linear antenna by replacing a radial transmission line with a biconical transmission line having a point voltage generator at its apex. By changing the apex angle to $\frac{\pi}{2}$, some impact of the gap was revealed. King concluded that only antennas with finite gap can radiate since in the limit of $\delta_g \longrightarrow 0$, the driving point reactance becomes zero (due to the infinite capacitance problem).

- In 1962, Duncan [66] presented an electric field distribution model as $\mathbf{E}(z) = (-\frac{V}{\pi})(\frac{\delta_g^2}{2} - z^2)^{-\frac{1}{2}}$, where V is the driving point voltage, and δ_g is the gap size, and the antenna is along the z-axis with the origin at the center of the gap.

- In 1967, Miller [39] extended the work of Chen and Keller [60], calculating the admittance of an infinite cylindrical antenna as a function of the frequency and gap thickness. He showed that the Chen and Keller results were valid only for infinitesimal gaps, and as the gap approaches zero, the condition $k\delta_g = \frac{2\pi}{\lambda}\delta_g << 1$ (by Chen and Keller [60] and Fante [61]) should be used in order to create a more reasonable situation for modeling a uniform electric field across the gap. Miller's model was not limited to vanishing gaps and yielded susceptance values for an infinite dipole with larger gap sizes. The methods of [60, 61] and [39] were based on numerical evaluation of the antenna current. One of the restrictions was that the singularity of the integral at $\delta_g = 0$ does not allow an estimate of the impact of a zero gap. In short, Miller's results for the infinite antenna were based on a constant electric field in the gap, and included admittance values for a couple of antenna radii and gap thicknesses.

- In 1968, Hurd and Jacobsen [67] also presented a numerical analysis for an infinite cylindrical antenna, claiming a more realistic model for the electric field within the gap on the basis that the constant field does not satisfy the edge condition. Their model showed significant differences in the susceptance, and the conductance agreed very well with Miller's result, as could be expected.

- In 1981, Stutzman and Thiele [44] modeled and analyzed the gap feed for microstrip antennas and the terms *proximity*, *noncontacting*, and *gap feed* were used to describe the electromagnetic coupled feeds. In a sense, this extended the work of Silver [56] who discussed the general feed problem in detail. However, the effect of a feed gap on antenna impedance was not treated in either case.

- In 1989, MacPhie [45] presented the inclusion of a wire pair transmission line to the finite gap dipole. The fields were found from the contributions of the four wires, but the impedance was not investigated. Also in 1989, Do-Nhat and MacPhie [42] presented their results for the admittance of a center-fed dipole with finite gap in a finite waveguide, terminated in an infinite groundplane. This model avoids the divergence of the susceptance.

Despite decades of research, this subject remains topical, e.g., [68–73], with multiple new works appearing typically each year. This section contains some representative references only, with some others in different sections.

2.5 Theoretical Approaches for Dipole Impedance

For a current excitation, the radiation resistance of a lossless antenna can be well defined by equating its radiated power, calculated from the far fields, to its circuit model feed point power, e.g., [38, 74]. The input resistance is then calculated from the radiation resistance and the current distribution evaluated at the feed. But the near field which supports the reactive energy storage is needed to find the reactance, e.g., [43]. The dipole antenna is assumed lossless. However, using conductors such as silver and copper, and even stainless steel, does not affect the results much at low frequencies [9]. For example, at 1GHz, the ohmic resistance is less than 10Ω for $a = 10^{-4}\lambda$ and is less than 1Ω for $a = 10^{-3}\lambda$. At millimeter-wave frequencies, for example 60GHz, gold would typically be used, and for $a = 10^{-3}\lambda$, the ohmic resistance is a couple of ohms, but for thinner wires of $a = 10^{-4}\lambda$, the ohmic resistance approaches the radiation resistance [9].

The end current of the dipole is neglected. For a solid conductor, current will flow across the end of the wires, and neglecting this current introduces an error in the impedance of the order of ka, e.g., [52]. Since a is assumed to be small ($a = 10^{-4}\lambda$), the error will be in the order of a few times 10^{-4}. This is negligible in the context of the impact of other

approximations in the induced EMF method.

Similarly, circumferential currents are neglected. In the context of theoretical excitations along the axial direction, there is no mechanism for exciting circumferential currents as long as the feed and structure are azimuthally symmetric. In practice, for thin wire dipoles, the circumferential current, if present at all, has negligible impact.

2.5.1 Theoretical Approach: Impedance of the Dipole without Gap

Using the Induced EMF Method

The induced EMF method was presented in 1922 by Brillouin [75] as a means of calculating the impedance of an antenna from a given approximation to current, [43, 76]. It has been shown that the mathematical form of the induced EMF equation is almost exact [76]. The formulation does not feature an explicit feed model (although it can be implied – the usual formulation is for the no gap case). The sinusoidal current model holds well for short dipoles, but the assumption breaks down for full wavelength dipoles – here the sinusoidal form of the center feed current would be zero, and the center feed point impedance would become infinite, which does not happen in practice. More refined formulas for the current are available, e.g., [77].

For the no gap feed, an impressed current excitation is intuitively preferred over infinitesimal gap voltage excitation, and such an excitation is used here to offer consistent results with previous EMF method solutions. It should be noted that such an excitation current has no physical support in the context of a dipole with a central gap. A magnetic frill would give similar excitation, but again there is no physical structure for supporting the frill. These issues are typical in discussions of modeling the feed region. For example, in numerical techniques, it is noted in [52] that the gap voltage should be the integral of the electric field across the gap, which with the feed current, allows a feed impedance to be defined. But the current distribution now needs to support this gap field, and with the numerical sample points being only on the wire (i.e., the fields within the gap are not sampled), the ensuing linear equations become non-unique [52]. One approach is to set the gap field to be given by the gap voltage over the gap size, but perhaps because of the non-uniqueness, the impedance results are reported as unreliable [78]. The feed excitation modeling is still an active topic in antenna research and new feed models are continually being published, e.g., [73].

Using the assumed sinusoidal current excitation for a center-fed dipole of length l, yields the well known following form (for a dipole along z-axis), e.g., [37] (a more detailed explanation is found in Appendix A),

$$E_z = \frac{-j\eta I_{max}}{4\pi}\left(\frac{e^{-jkR_1}}{R_1} + \frac{e^{-jkR_2}}{R_2} - 2\cos\left(\frac{kl}{2}\right)\frac{e^{-jkr}}{r}\right), \tag{2.1}$$

where R_1 and R_2 are the distances to the both ends of the dipole and r is the distance of the observation point to the origin. The input impedance referred to the current maximum, I_{max}, is

$$Z_m = -\frac{1}{I_{max}^2}\int_{-\frac{l}{2}}^{\frac{l}{2}} I_z(\rho = a, z = z^{'})E_z(\rho = a, z = z^{'})dz^{'}, \tag{2.2}$$

where I_z is the current distribution along the wire dipole. Equation (2.2) with the embedded E_z has the trigonometric integral format (see Appendix B) and cannot be solved analytically and in fact its numerical calculation has pitfalls. Here the numerical integration methods are carefully applied, e.g., [79]. Referred to the feed point using the assumed sinusoidal form of the current, the impedance is

$$Z_{in} = R_{in} + jX_{in} = \frac{Z_m}{\sin^2(\frac{kl}{2})} = \frac{R_m}{\sin^2(\frac{kl}{2})} + j\frac{X_m}{\sin^2(\frac{kl}{2})}. \tag{2.3}$$

Solving equations (2.2) and (2.3), for a zero gap dipole, the reactance is a function of dipole thickness, but when the dipole length is a multiple of the half-wavelength, the reactance is independent of the dipole thickness. From the induced EMF method, the half-wavelength dipole has reactance of 42.5Ω.

Figure 2.3 represents the input reactance of a thin wire dipole, with sinusoidal current distribution, calculated from the induced EMF method. The increasing dipole thickness gives decreasing resonance frequencies (the resonance is defined here for convenience by a zero reactance, rather than by the maximum resistance which is more practical). From the figure, it is observed that increasing the thickness of the wire dipole leads to a decreasing slope of the reactance curve, and to the higher bandwidth. This is in accordance with the established results, e.g., [56, 80]: a thinner dipole provides lower bandwidth.

Using the Wave Structure Method

Andersen [35] gave a general treatment to evaluate the admittance of the monopoles and dipoles depending on the thickness. Related approaches are also given in [52, 63]. The wave

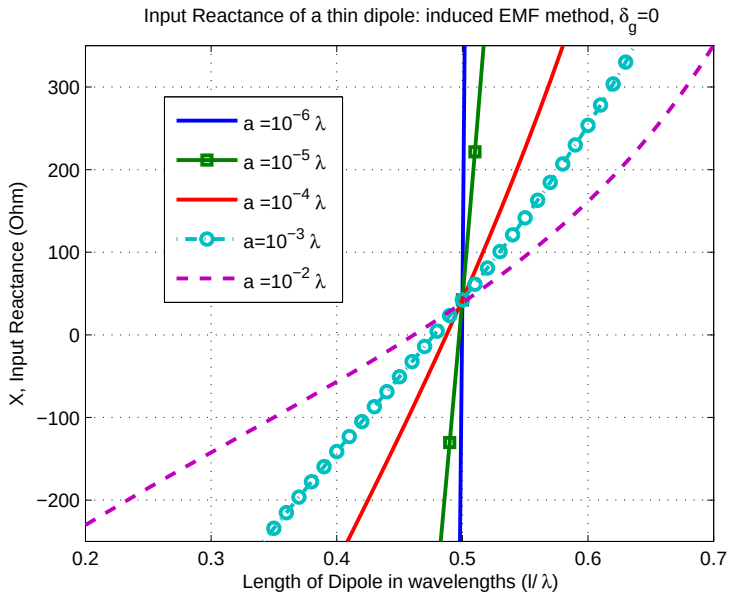

Figure 2.3: Dipole reactance from the induced EMF method for varying thicknesses. All the curves intersect at $l = 0.5\lambda$ and $X = 42\Omega$.

structure method is well suited for a monopole on an infinite ground plane with a coax feed as well as its dipole equivalent with a magnetic frill [14, 35, 52]. For lossless monopoles of length l_m (the equivalent dipoles have total length $l = 2l_m$) the input admitttance is

$$Y = \frac{-2\pi}{Z_0 \log(ka\Gamma/2)} + \frac{4\pi}{Z_0 \log(\frac{a}{2l_m})(\exp(j2kl_m) + 1 + \log(j4kl_m\Gamma)/(2\log(ka)))}, \tag{2.4}$$

where $\Gamma = \exp(C_{Euler}) = 1.781$ [1] and Z_0 is the intrinsic impedance. Equation (2.4) is valid, in principle, for a monopole length greater than 0.2λ and for wire thicknesses of $a \leq 0.01\lambda$, [4, 14]. Figure 2.4 shows the reactance of the dipole calculated by wave structure method. Here also, the thicker wire makes the reactance curves flatter, and the antenna impedance bandwidth becomes higher. The increasing dipole thickness again leads to a decreasing resonance frequency.

Comparing Figures 2.3 and 2.4, the reactance curves from the induced EMF method

[1] C_{Euler} is the Euler constant. It is defined as $\lim_{n\to\infty}\left(\sum_{k=1}^{n}\frac{1}{k} - \ln(n)\right)$, and is to 10 decimals approximately 0.5772156649.

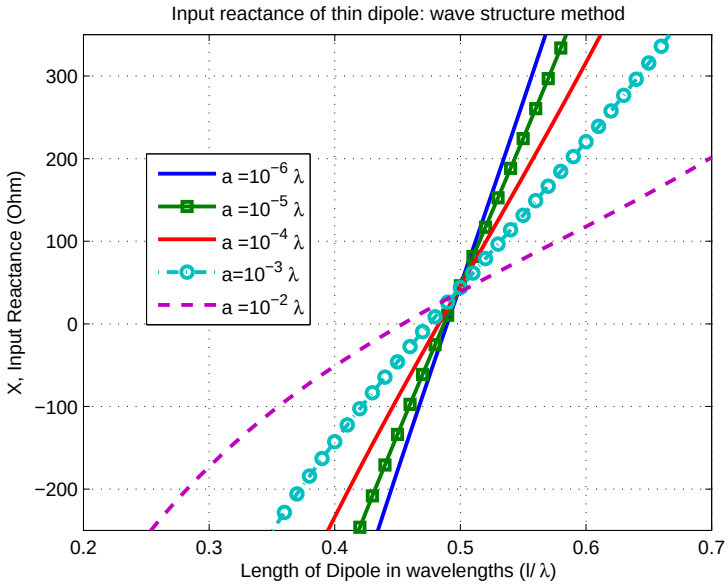

Figure 2.4: Dipole reactance from the wave structure method for varying thicknesses.

have convex form, while the wave structure method results are concave. These forms govern the form of the quality factor (chapter 2).

Figures 2.5(a) and 2.5(b) depict the impedance of a lossless, half wavelength dipole from the induced EMF method and from the wave structure method, respectively. These figures show the effect of the wire thickness and the length, and this cannot be reliably calculated from currently available numerical methods such as MOM [14]. The resistance from the induced EMF method is not sensitive to the wire thickness, while for the wave structure method, for thicknesses of $a < 0.005\lambda$, the resistance has sharp changes with respect to the thickness change. These figures do not indicate the concavity/convexity trend in Figures 2.3 and 2.4.

2.5.2 Theoretical Approach: Impedance of the Dipole with Finite Gap

In the previous section the two theories for the impedance of a dipole without a gap were reviewed. In this section, the induced EMF formulation is modified and developed for the finite gap case.

The wave structure method does not readily support a gap feed. However, a transmission line model is used to modify the method for a finite gap. The gap is modeled as a section of

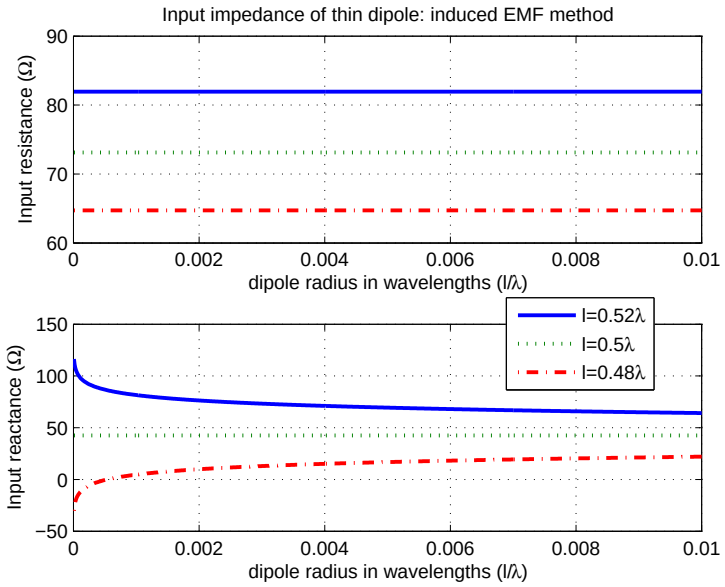

(a) Induced EMF method

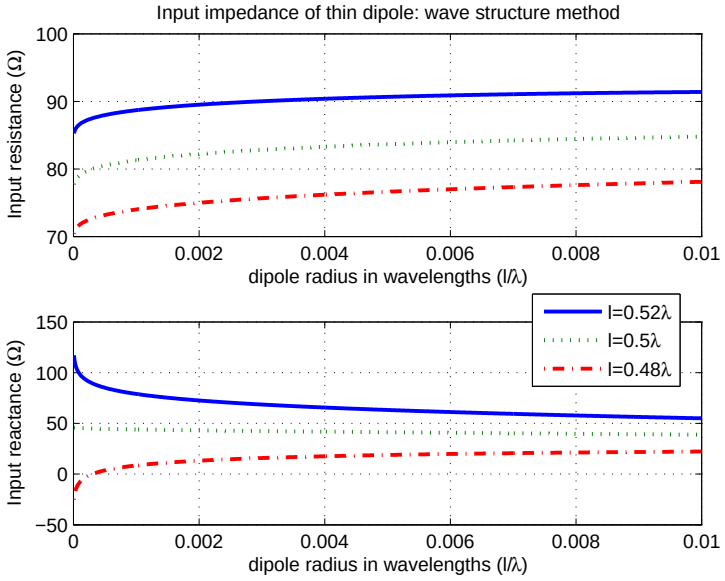

(b) wave structure method

Figure 2.5: Lossless dipole impedance from the induced EMF and wave structure methods, showing the effect of the wire thickness, which is difficult to calculate from any other method.

free space "transmission line" inserted across the center of the dipole gap, followed by the arm of the dipole (a load with known impedance). The resulting reactance matches well with those of the MOM (not shown). However, the induced EMF method, with gap (not shown) does not agree so well or follow the same trend [4], see below.

For a center fed dipole with gap size δ_g and sinusoidal current distribution, the input impedance can be interpreted as:

$$Z_m = -\frac{1}{I_{max}}[\int_{-\frac{l}{2}}^{-\frac{\delta_g}{2}} \sin[k(\frac{l}{2}+z^{'})]E_z(\rho=a,z=z^{'})dz^{'} + \int_{+\frac{\delta_g}{2}}^{+\frac{l}{2}} \sin[k(\frac{l}{2}-z^{'})]E_z(\rho=a,z=z^{'})\ dz^{'}]. \quad (2.5)$$

Equation (2.5) is similar to equation (2.2), but requires an even more demanding numerical computation. The gap is in the integral limits, based on electromagnetic theory. The idea is that in the antenna-theoretic model, the antenna radiation stems from the current distribution only on the dipole. Any direct radiation from the feed depends on the feed model, and the feed is not a part of the dipole structure for theoretical antenna impedance purposes.

In [45], the current is normalized by the feed point value, rather than at the center of the gap, as in (2.5). The worst case difference turns out to be about 5% in the current value.

The impedance resulting from (2.5), with dipole radius $a = 10^{-4}\lambda$ and various gap sizes, is depicted in Figures 2.6(a) and 2.6(b). This structure is too thin for a self-supporting wire but is realizable using dielectric mechanical support. The results show that over the range of gap sizes $0 \leq \delta_g \leq 10^{-2}\lambda$, there is no noticeable change in the resistance. But when the gap size is increased to $10^{-1}\lambda$, the change in resistance becomes noticeable, for example by about 20Ω at $l = \frac{\lambda}{2}$, and even more for a longer dipole. On the other hand, the reactance behavior, which governs the antenna bandwidth, is sensitive to the gap size. When the gap becomes larger, the reactance curve tends to be flatter, implying a larger theoretical bandwidth. For a very large gap (here for $\frac{\delta_g}{\lambda} = 0.1$), the resonance behavior ceases in the sense that the reactance remains positive.

Figures 2.7(a) and 2.7(b) show the same curves as an admittance, offering a different view of the (anti-) resonance. MacPhie [45] also notes a widening of the conductance curve with increasing gap size, and relates it to "the general theory of broad-band antennas".

For the half-wavelength dipole, the effect of finite thickness of the wire and the effect of the gap size are presented in Figures 2.8(a) and 2.8(b) which show the impedance from the

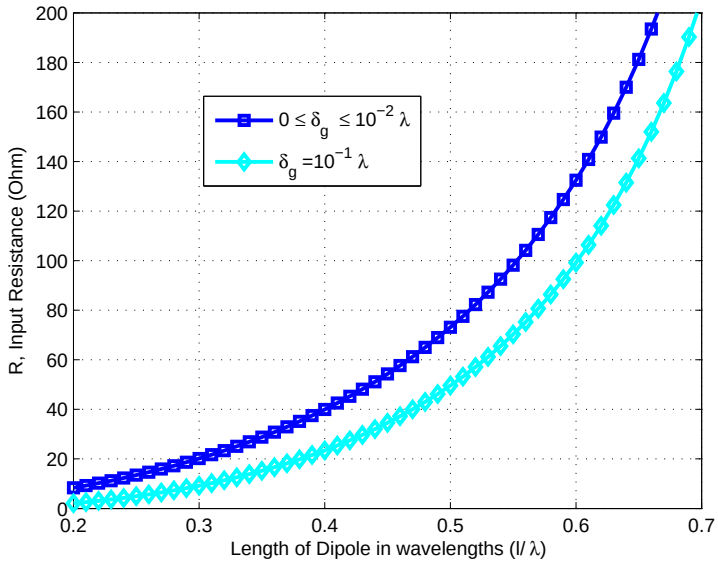

(a) Resistance

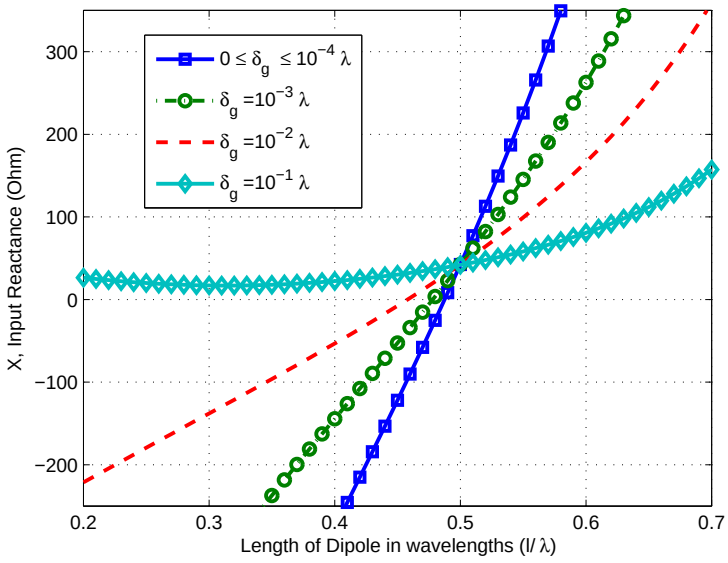

(b) Reactance

Figure 2.6: Dipole impedance from the induced EMF method for varying feed gap size and $a = 10^{-4}\lambda$. The diamond lines are for the largest gap ($\delta_g = 10^{-1}\lambda$, almost 20% of the half-wavelength dipole), calculated for a sinusoidal current distribution [4].

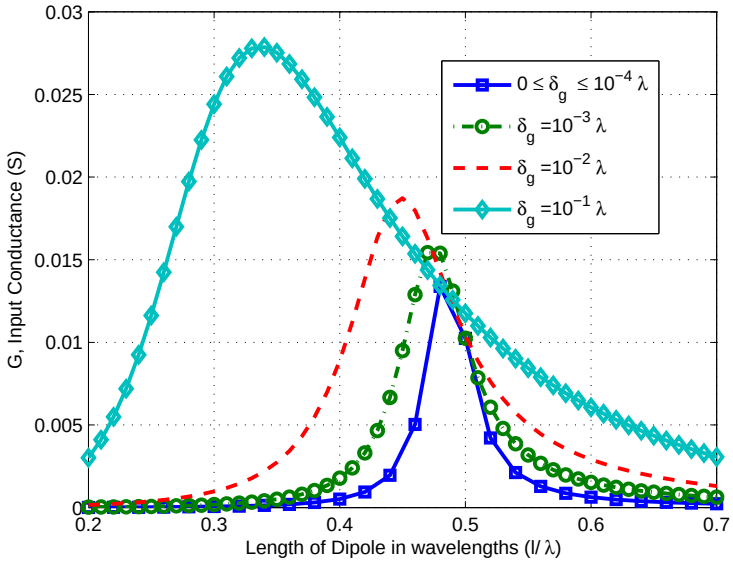

(a) Conductance

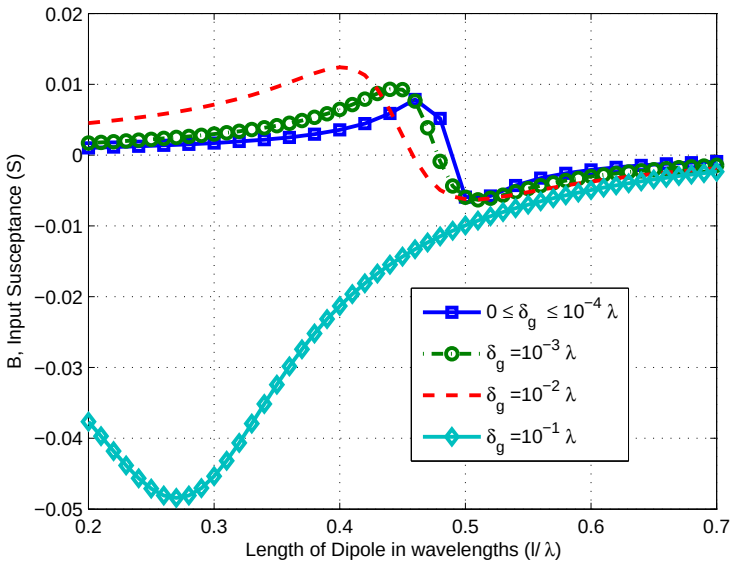

(b) Susceptance

Figure 2.7: Dipole admittance from the induced EMF method for varying feed gap size and $a = 10^{-4}\lambda$, calculated for a sinusoidal current distribution [4].

induced EMF method of (2.5). The resistance is constant for $\delta_g \leq 10^{-4}$ and the reactance is constant for $\delta_g \leq 10^{-2}$.

2.6 Numerical Methods to Evaluate the Impedance of a Dipole with Finite Gap

There are several numerical simulation packages but not all of them are suitable for treating the effect of the gap on the impedance. Different numerical methods have been applied as noted above. The FDTD result is from O.Franek [34]. Franek's rendition of FDTD allows only homogeneous mesh with one cell size throughout the domain. Since the δ_g gap must be equal to one cell, then the whole simulation has a cell size according to the desired gap. FDTD is compromised by a large dynamic range of dimensions, so a very thin dipole (with a large length to thickness ratio) is a difficult problem for this type of solver. Some further discussion on this is in [4].

The resistance curves from different methods are similar, but there are major differences in reactance results, no doubt reflecting the different feed models deployed. Figures 2.9(a) and 2.10(a) depict the resistance and conductance of the thin dipole with radius $a = 10^{-4}\lambda$ and gap $\delta_g = 10^{-1}\lambda$ from different methods. The resistance from FDTD is much higher than the other methods, while the conductance from the induced EMF is above the FDTD curve for the large gap size, i.e, $\delta_g = 10^{-1}\lambda$. Figures 2.9(b) and 2.10(b) depict the reactance and susceptance of the thin dipole with radius $a = 10^{-4}\lambda$ and gap $\delta_g = 10^{-1}\lambda$. Both induced EMF and FDTD curves yield almost the same quality factor.

The closest results (to those of induced EMF methods) from other methods are those from Franek's FDTD [34]. Both FDTD results and the induced EMF results have a higher theoretical impedance bandwidth for a larger gap. This is most easily seen directly from the reactance curves.

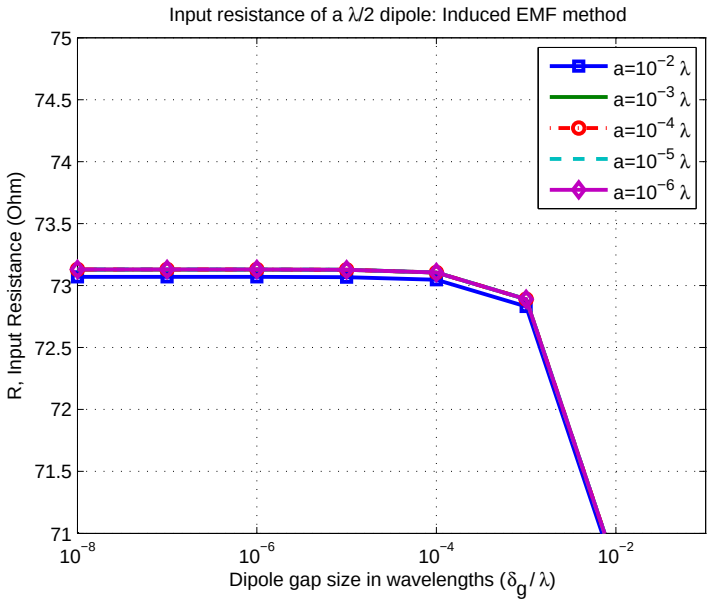

(a) Resistance

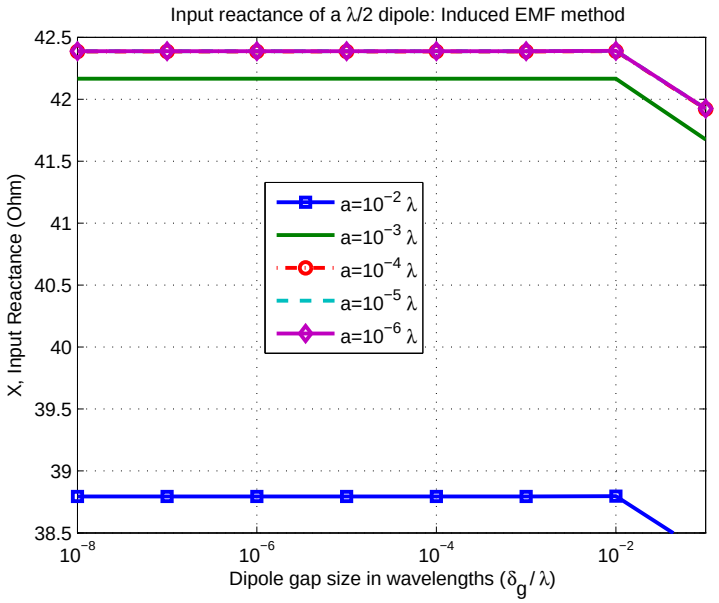

(b) Reactance

Figure 2.8: The impedance of a center fed, half wavelength dipole, showing the effect of the gap size and wire thickness.

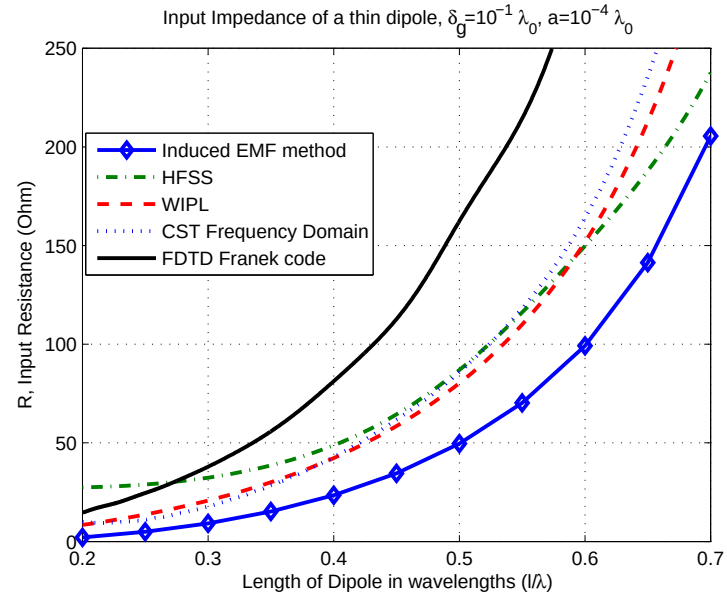

(a) Resistance

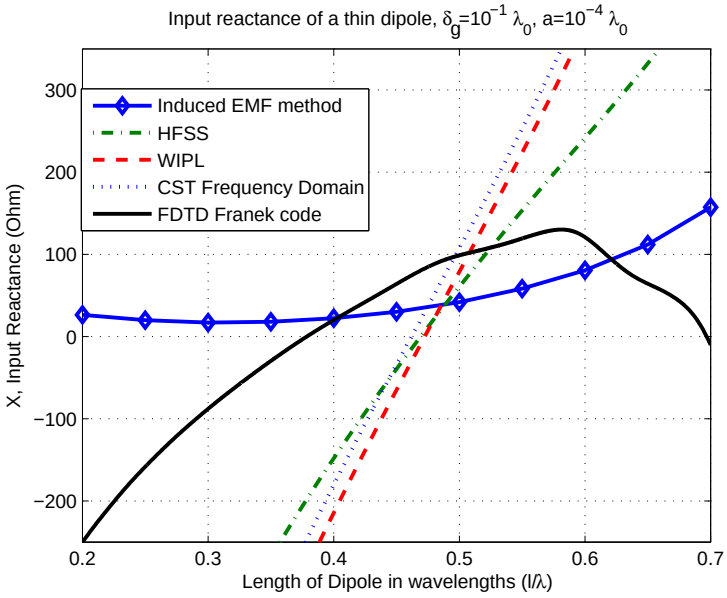

(b) Reactance

Figure 2.9: Resistance and reactance of a thin dipole of $\delta_g = 10^{-1}\lambda$ and $a = 10^{-4}\lambda$, from different numerical and theoretical methods [4].

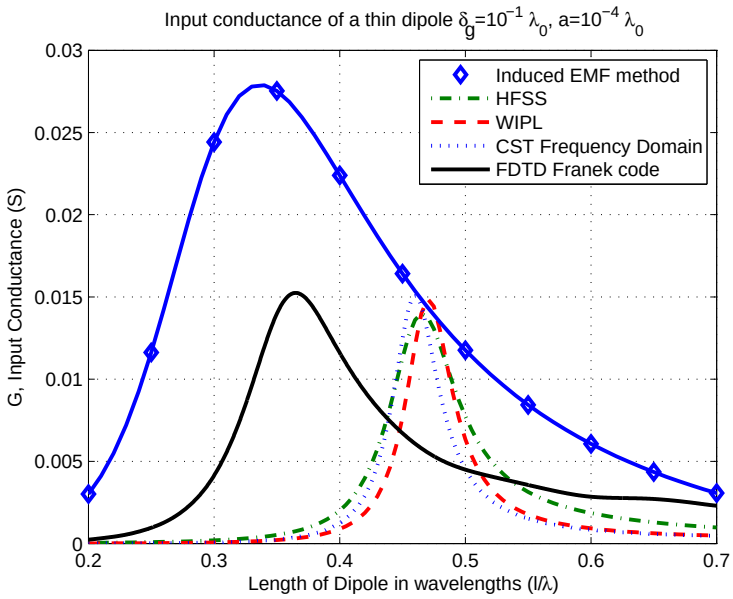

(a) Conductance

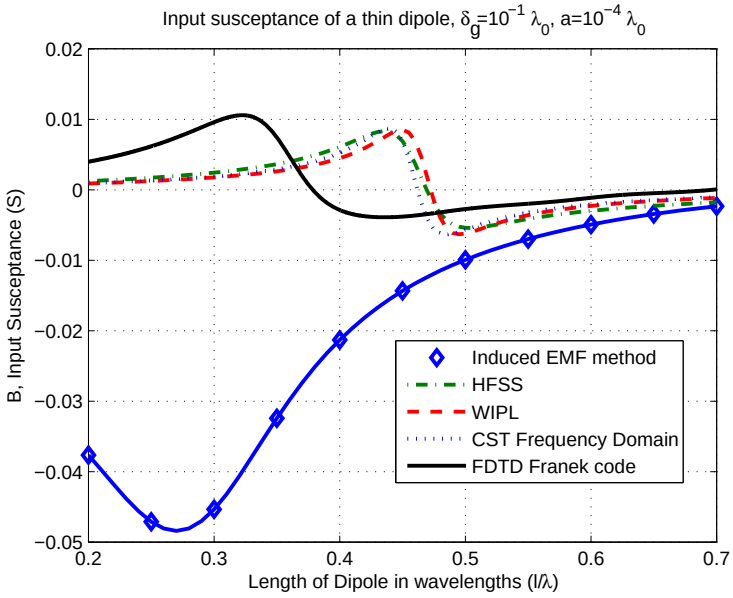

(b) Susceptance

Figure 2.10: Conductance and susceptance of a thin dipole of $\delta_g = 10^{-1}\lambda$ and $a = 10^{-4}\lambda$, from different numerical and theoretical methods [4].

Chapter 3

Quality Factor and Ohmic Loss of the Dipole

3.1 Introduction on Q and Radiation Efficiency

This chapter looks to the quality factor and theoretical bandwidth of a wire dipole. The Q is determined from different analytical and numerical methods and published measured results. The dipole radiation efficiency is also addressed in this chapter. Antenna efficiency directly impacts the efficiency of communications applications, and the emerging use of high frequencies has renewed interest in its mechanisms and estimation. This chapter includes the following subjects:

- The bandwidth results expressed via Q bounds from the induced EMF method (see section 3.2), the impact of the feed gap on the quality factor and impedance bandwidth of the thin dipole (see section 3.4).
- Different Q bounds from various numerical and theoretical methods, as well as the recent and the conventional bounds on Q (see section 3.3).
- Ohmic loss and radiation efficiency of a half-wavelength (as a reference length) dipole (see section 3.5), evaluation of the ohmic loss of a short dipole, i.e., $0.2\lambda \leq l \leq 0.7\lambda$, (see section 3.5.8).

3.2 Quality Factor of an Antenna

Following the classical treatment of Q, e.g., [81], adapted for antennas, e.g., [14, 80], the quality factor can be found and related to a theoretical bandwidth. The "exact" and "approximate" expressions for the quality factor and bandwidth of a general antenna have been found, e.g., [82, 83]. It has been shown that for medium-bandwidth antennas the derivative of Z_{in} with respect to frequency is approximately proportional to Q, and Q is approximately inversely proportional to the bandwidth of the antenna. This approximate expression is used here to evaluate the quality factor of the dipole. The recent bounds on linearly polarized antennas [6] also show how increasing the thickness of the dipole increases the bandwidth. From [81], the quality factor of a circuit, Q, is defined as

$$Q = \frac{\text{energy stored}}{\text{energy dissipated per cycle}}. \tag{3.1}$$

Near resonance, a simple circuit model has a Q that can be expressed in terms of the slope of the reactance, e.g. [12],

$$Q = \frac{\omega}{2R}\frac{\partial X}{\partial \omega}. \tag{3.2}$$

This Q is called the signed quality factor because the factor $\frac{\partial X}{\partial \omega}$ can be negative when the slope of the reactance versus frequency curve is negative. (Foster's reactance theorem [84] for lossless networks shows that the slope of the reactance must always be positive, but radiation "losses" mean that the slope can be negative [14].) A traditional fix is to take the absolute value of the derivative, ensuring a positive Q, as in equation (3.1). The unsigned quality factor is also evaluated using the approximate formula in [82],

$$Q = \frac{\omega}{2R}\left|\frac{\partial Z}{\partial \omega}\right|. \tag{3.3}$$

A resonant frequency can be defined by taking the peak of the resistance, where the slope will be zero. In the case of a resonant RLC circuit, at the resonance frequency, ω_{res}, the following equality holds,

$$\frac{\partial Z_{in}}{\partial \omega}|_{\omega_{res}} = \frac{\partial X_{in}}{\partial \omega}|_{\omega_{res}}, \tag{3.4}$$

so the two approaches are equivalent in this sense. But with real-world circuits, and some numerical solutions, the impedance form tends to give smoother curves.

The impedance from the induced EMF method is now used for finding the impact of the gap size on Q. Figure 3.1 shows the quality factor as a Chu graph of a thin dipole

with different gap sizes. According to, for example, [85], the Chu limit is applicable for electrically small antennas. There is no universal definition for electrically small antennas, but often having an inscribing sphere of radius $kr \leq 1$ is taken, although some authors prefer $kr \leq 0.5$. The Chu limit [5] on quality factor was derived in [86] and also in [83] from a different method. This limit is exact (under the assumptions of its formulation), and is

$$Q_{Chu} = \frac{1}{(kr)^3} + \frac{1}{kr}, \tag{3.5}$$

where kr is the electrical radius of the inscribing sphere. Hansen and Collin [87] noted that the formula can be applied to any antenna configuration fitting inside the sphere and excited by a single mode. There is also Chu's approximate formula [88, 89], and this was later corrected to [83, 90],

$$Q_{Chu_{AC}} = \frac{1 + 2(kr)^2}{(kr)^3[1 + (kr)^2]}. \tag{3.6}$$

In the context of the thin dipole of length l, the radius is $r = \frac{l}{2}$. If the dipole becomes significantly thick, then the radius of the inscribing sphere will increase, i.e., $r = \sqrt{(\frac{l}{2})^2 + a^2}$, leading to a lower Q and a higher bandwidth. For example, for a radius of $a = 0.1\lambda$ there is a decrease in Q_{Chu} of about 60% and 18% for dipoles with $l = 0.2\lambda$ and $l = 0.5\lambda$, respectively. But for the thin dipoles treated here, the thickest case is $a = 10^{-2}\lambda$ which corresponds to decrease in Q of less than 1% over the range of the dipole lengths considered.

The Chu limit offers a useful framework for comparing the spherical compactness of different practical antennas, e.g., [14, 91].

3.3 Review of Bounds for Q

The limitations on the radiation Q has been the subject of several treatments, *cf.*, [92]. In this section the Q is found from the available approaches for lossless, thin dipoles with and without a finite feed gap. The interest is in dipoles of around a half wavelength. Classical treatments of Q, e.g., [81] for the bandwidth allow the calculation of Chu curves for resonant-like antennas. The approximate expression, e.g., [82], is used here for the Q. It gives similar, but not identical, results to the classical approach. Recent bounds [6] for linearly polarized antennas with arbitrary shapes are included, showing how increasing the thickness of the dipole increases the bandwidth. Numerical results from the MOM, FDTD, and the FIT,

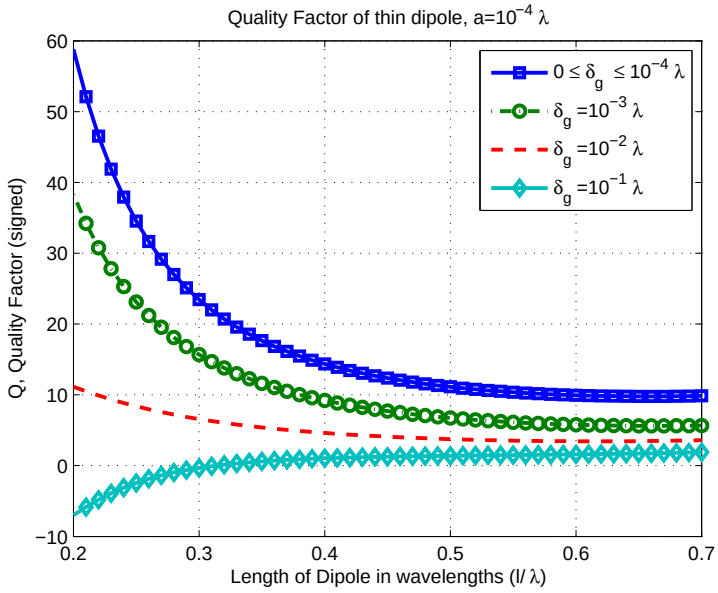

(a) Signed quality factor, from (3.2), for induced EMF method.

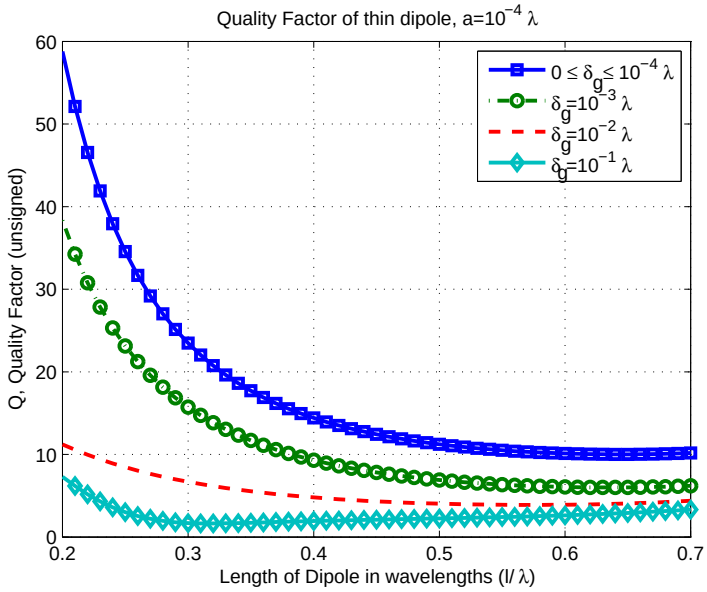

(b) Quality factor, from (3.3), for induced EMF method.

Figure 3.1: The quality factor of a thin center-fed dipole, i.e., $a = 10^{-4}\lambda$, for different gap sizes. The impedance is from induced EMF method, and the signed and unsigned Qs are calculated from (3.2) and (3.3), respectively.

using commercial solvers have been used. The FIT results are not included here. They are close to the results from the MOM. The lowest Q arises from the induced EMF method where a larger feed gap leads to a larger theoretical bandwidth for thin wire elements. This method is known to be rigorous but it is a challenge to check the result because no other theoretical or numerical methods are suitable for such thin structures, and it is difficult to realize this gap feed for a physical measurement. The results for thicker dipoles, from the usual solvers, are also included in this chapter.

In [6], Gustafsson et al. presented new bounds for arbitrarily shaped volumes. From [6] new bounds can be interpreted to be based on the principles of primitive causality, time-translational invariance, and reciprocity, and these bounds are not restricted to the sphere but hold for arbitrary antenna volumes. For the cylindrical dipole, these bounds turn out to be looser than the classical Chu bounds, e.g., [5, 10], see below. For a z-directed dipole, this bound is

$$Q_{Gustafsson} = D\frac{3}{2\eta k^3(\frac{l}{2})^3}\frac{\ln\frac{l}{a}-1}{|\hat{\mathbf{e}}\cdot\hat{\mathbf{z}}|^2}, \tag{3.7}$$

where D is the directivity, η is the absorption efficiency, and $\hat{\mathbf{e}}$, is the electric polarization vector. This quality factor bound is included below for $\eta = 0.5$ [93] and maximum directivity of a dipole $D = 1.64$.

Figure 3.2 shows the various Chu bounds, simulations and measurements [80] (see Appendix C), Gustafsson's 2009 bound [6], and results from [61, 83, 85–87, 89, 90], along with our results from the induced EMF method, and some of our numerical experiments. There is a great deal of information here, so the features of interest are bullet pointed below. It is noted here that a comparison of the several minimum Q formulas for a spherical volume and linear polarization (including equations (3.5) and (3.6)) has been recently presented in Figure 1 of [90], highlighting their similarity.

- The Chu approximate limit (lowest curve), e.g., [83], is the tightest bound; and the Gustafsson limit is the highest curve, here for the case $a = 10^{-4}\lambda$, and the loosest bound in the sense that below this value it cannot be operated (under the assumptions of the formulation). This behaviour is expected due to the fact that the Gustafsson limit is based on the volume of the dipole only, and the Chu limit caters for the much larger spherical volume. However, practical, low loss dipoles indeed operate below their Gustafsson curves, as noted below.

- Samples of the MOM solution using WIPL-D (circle solid line for case $a = 10^{-4}\lambda$, and

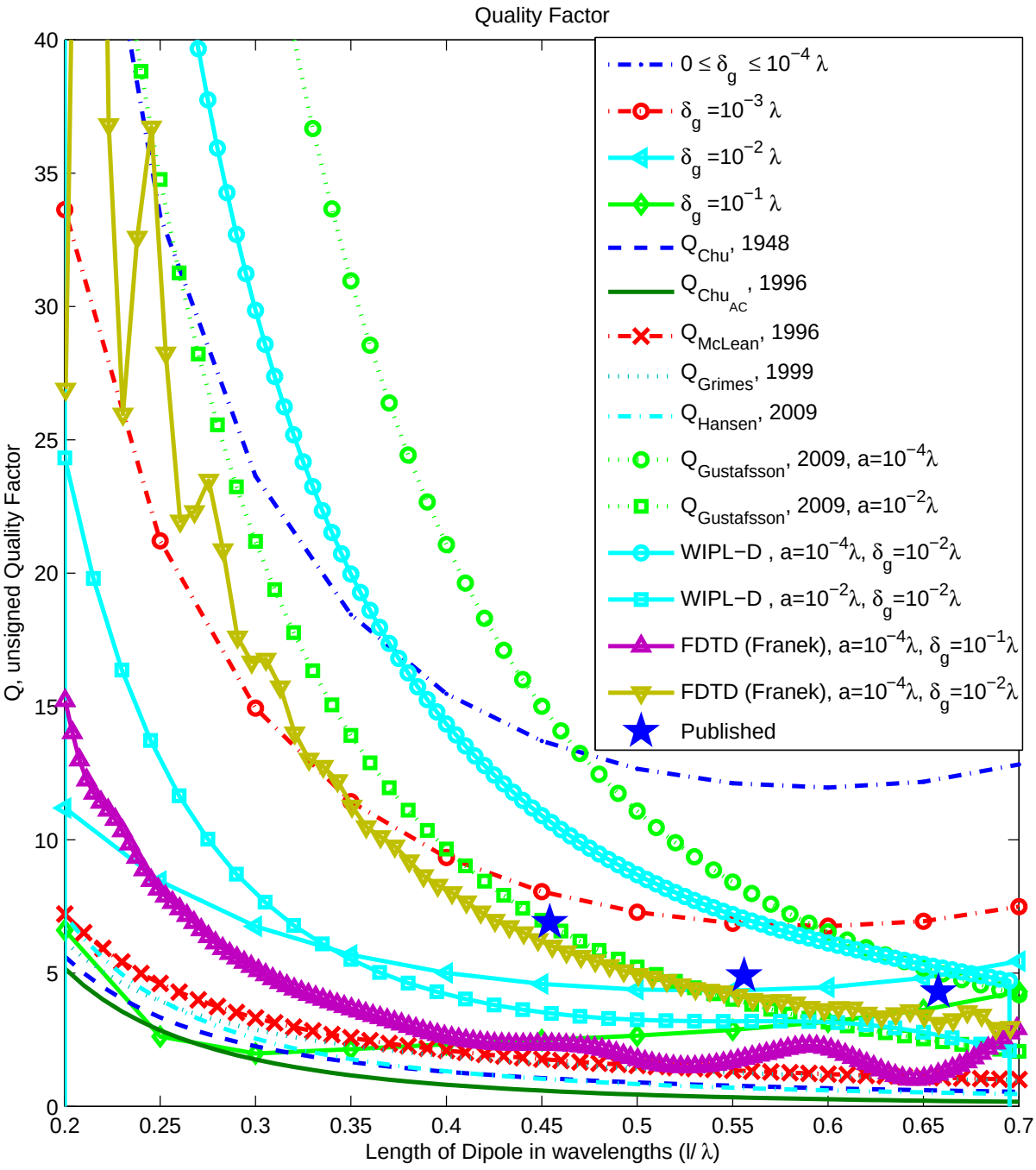

Figure 3.2: The Q bounds from various methods. The first four entries in the legend (for different gap sizes, and $a = 10^{-4}\lambda$), are from the induced EMF method. The "Published" results are from MOM and physical experiment presented in [80,82] (see Appendix C, (C.2) to (C.5)).

square-solid lines for case $a = 10^{-2}\lambda$) show smooth curves and insensitivity to the gap size for the thin wire case. For the thicker wire, a larger gap gives a higher Q, and this is in contrast with the FDTD results and the induced EMF method. But it is recalled here that the gap size is not well-defined in the MOM, in the sense of the discussion above. The gap size is taken to be the same as the radius for the curve shown. The thicker dipole is closer to the Chu limit, i.e., has larger theoretical bandwidth, as expected, and the changing bandwidth is available from the curves (see below).

- A previously published MOM solution, which used NEC [30], and which has concurring physical experimental points, is given in [80] and [82]. This data is re-expressed for the Chu diagram and shown using the star symbols (three points only), Appendix C, (C.5). These examples have radii ranging from $a = 1.3 \times 10^{-3}\lambda$ to $a = 1.9 \times 10^{-3}\lambda$, (C.4b), implemented as a copper monopole on a large groundplane, so there is no gap. The result is consistent with our WIPL results.

- Examples of the FDTD solutions, using the Franek code [34], for different gap sizes (apex-up-triangle-solid line, for $\delta_g/\lambda = 10^{-1}$, and apex-down-triangle-solid line for $\delta_g/\lambda = 10^{-2}$ and the thin dipole). The larger gap size gives a smaller Q, which is similar to the results of the induced EMF method. Again, it should be noted that the gap size is not well-defined. The larger gap gives smoother curves for shorter lengths, whereas the smaller gap has ripples for the shorter lengths (and smoother curves for longer lengths).

- Examples of the Chu-type bounds, labeled Q_{Chu} (equation (3.5)), $Q_{Chu_{AC}}$ (equation (3.6)), Q_{McLean} [83], Q_{Grimes} [94] and Q_{Hansen} [87], for the ideal case of a no-gap dipole using a sphere of radius $r = \frac{l}{2}$ inscribing the dipole, all provide Qs which, especially for lengths shorter than a half wavelength, are about the same as those of the induced EMF method and FDTD.

- The curve for induced EMF method for the largest gap considered, $\frac{\delta_g}{\lambda} = 10^{-1}$, is not smooth, but essentially tracks the Chu limits for small lengths, ($\frac{l}{\lambda} < 0.4$). For larger dipole lengths ($\frac{l}{\lambda} > 0.6$), all the induced EMF curves tend to feature a decreasing Q for decreasing dipole length. The mathematical mechanism for this behavior is seen in Figure 2.6(b) where the slope of the reactance (for the different gap sizes) is essentially constant but the resistance is increasing with increasing dipole length. In Figure 3.2

there is one point around $\frac{l}{\lambda} = 0.25$, where the calculated result goes below the Chu curve. Here, the gap is about the same size as the dipole arms, and the formulation, or at least the modeled current distributions on the arms, might be considered suspect because the situation is relatively widely separated short conductors.

- For a half wavelength dipole, the Q from the results in [82,85,95], for center-fed, tuned, lossless straight wire (no gap) antennas, is about 10. From the induced EMF method, Q ranges from 3 to 15 for different gap sizes.

3.4 Bandwidth

The half power (3dB) impedance bandwidth of an antenna (near resonance) relates to the quality factor, as [81],

$$BW_{3dB} = \frac{\Delta\omega_{3dB}}{\omega_C} = \frac{1}{Q}, \tag{3.8}$$

where ω_C is the resonant frequency, which is often taken as the center-of-band frequency.

Q relates to an unloaded port, which is why the bandwidth is referred to as theoretical bandwidth. In practice, the bandwidth would be measured with a load, and certainly a working antenna would be loaded. This load is considered fixed, meaning that its impedance, including the effect of any associated matching circuit, is fixed.

With a fixed load, the behavior of the reflection coefficient around resonance is used to define a loaded, double-sided, 3dB relative bandwidth, $BW_{3dB}^{(L)}$, and a "resonance" frequency where the reflection coefficient is a minimum, here denoted $\omega_C^{(L)}$. Again, this is often taken as the center-of-band frequency. This loaded 3dB bandwidth corresponds to a loaded quality factor, Q_L *viz.*, $BW_{3dB}^{(L)} = \frac{1}{Q_L}$, and if the load and antenna are perfectly matched, then $Q_L = \frac{Q}{2}$. Consequently for a load matched to the antenna, the loaded bandwidth is twice the theoretical bandwidth, i.e., $BW_{3dB}^{(L)} = 2BW_{3dB}$ (matched). The practical ramification is that a measured impedance bandwidth can be made larger by including a larger load, or extra loss in the antenna. In measurements, for finding Q, unmatched antennas (at the center frequency) can still be used, and values other than 3dB for defining the reflection coefficient bandwidth can be used, e.g., [14, 91].

Figures 3.3(a) and 3.3(b) show the loaded theoretical relative bandwidth, $BW_{3dB}^{(L,T)} = \frac{2}{Q}$ (i.e., this is assumed to be perfectly matched to its load at the center frequency) and the Q is from Figure 3.1. The curves are similar except for the large gap case. For the large gap,

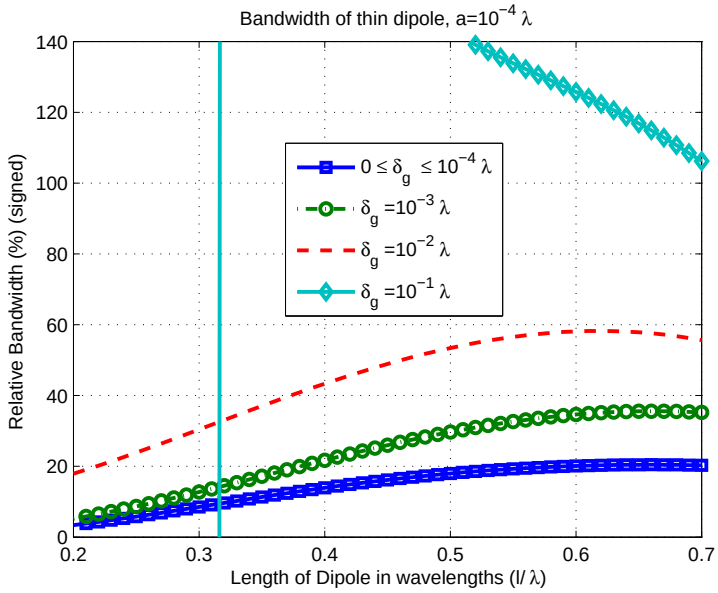

(a) Loaded theoretical relative bandwidth of the center-fed thin dipole, i.e., Q from (3.2)

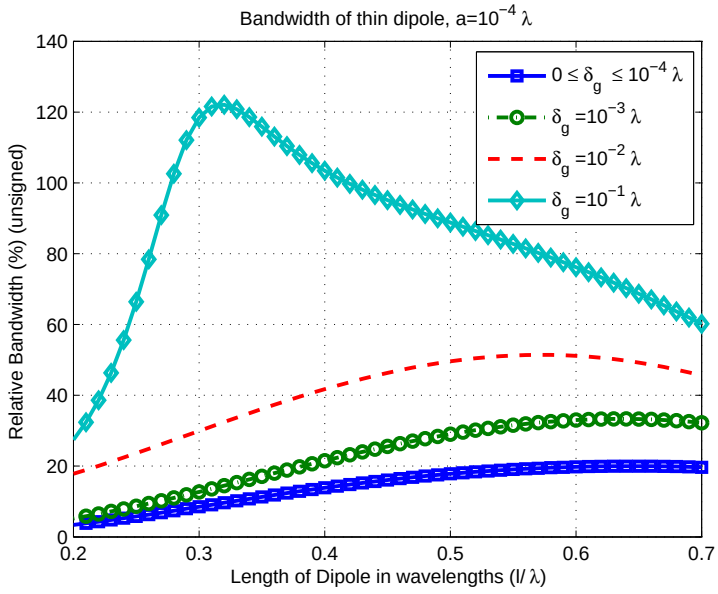

(b) Loaded theoretical relative bandwidth of the center-fed thin dipole, i.e., Q from (3.3)

Figure 3.3: Loaded theoretical bandwidth of a thin dipole for different gap sizes corresponding to the Qs from Figure 3.1.

the upper curve has an abrupt change in its bandwidth from the sign change in Q using equation (3.2); and the resistance derivative included in the lower curve has the effect of reducing the bandwidth significantly.

Figure 3.4 shows the power reflection coefficient, $|\Gamma_{refl}|^2$, for a dipole of radius $a = 10^{-4}\lambda$, connected to 50Ω, for different gap sizes. There is no matching circuit. The associated loaded impedance bandwidth increases with increasing gap size.

In Table 3.1, the 3dB loaded bandwidth results are summarized for different gap sizes, a radius of $a = 10^{-4}\lambda$, and load impedances of 50Ω and 75Ω. As a comparison, the impedance bandwidth from the FDTD impedance results are given in table 3.2, showing good agreement. The results are consistent with Figures 2.9(b) and 2.10(b), in the sense that the slopes of the reactance curves from the FDTD method indicate a larger bandwidth for larger gap sizes. The bandwidths in table 3.1 appear insensitive to the load resistance choices, 50Ω and 75Ω, but this is because the dipole resistance is reasonably close to both of these values, and the antenna is matched. The bandwidths are in agreement with the loaded theoretical values in Figure 3.3(b), and this is expected since they are both based on the dipole impedance behavior. However, in Figure 3.4, the impedance behaviour is across a band, whereas in Figure 3.3, the impedance bandwidth is inferred from a single frequency.

δ_g/λ	f_c in GHz 50Ω line	3 dB BW % 50Ω line	f_c in GHz 75Ω line	3 dB BW % 75Ω line
10^{-1}	0.9850	76.63%	1.07110	74.22%
10^{-2}	0.9520	43.57%	0.98530	51.88%
10^{-3}	0.9666	24.16%	0.9830	29.73%
10^{-4}	0.9750	14.87%	0.9827	18.35%
zero gap	0.9750	14.07%	0.9827	17.32%

Table 3.1: The loaded relative bandwidth, $BW_{3dB}^{(L)}$, for a center-fed thin dipole of radius $a = 10^{-4}\lambda$ with different gap sizes, and for loads of 50Ω and 75Ω. The impedance is from the Induced EMF method.

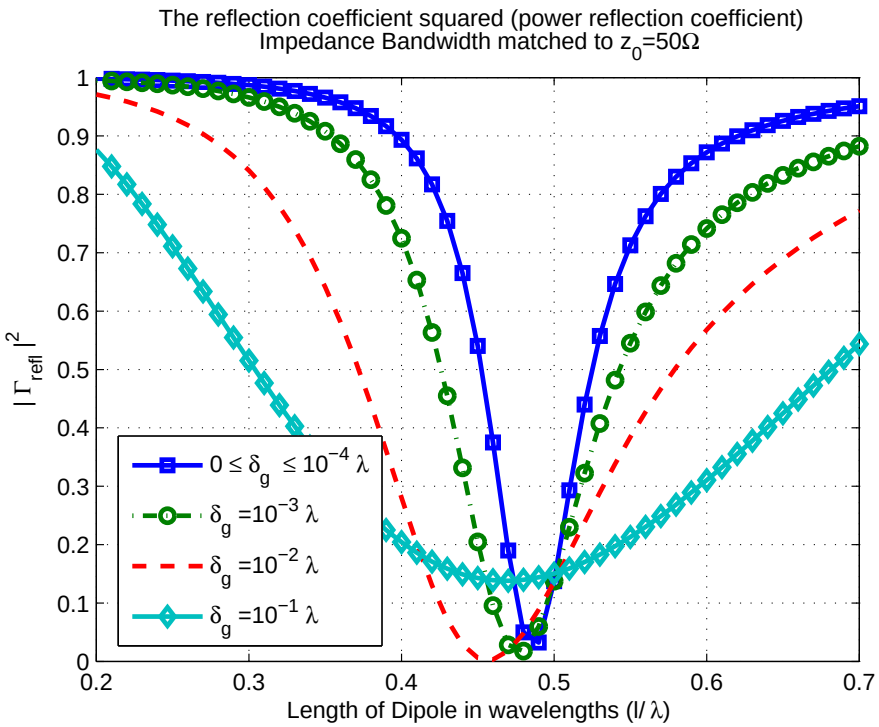

Figure 3.4: Power reflection coefficient, $|\Gamma_{refl}|^2$, of a lossless thin dipole with finite gap versus antenna length in wavelength from induced EMF method.

3.5 Ohmic Loss in a Dipole

3.5.1 Antenna Efficiency Factors

The antenna gain is a fundamental parameter in a wireless link, and is also the capacity-limiting part of the wireless system which can be controlled by the link designer [91]. When perfect line-of-sight (LOS) between the transmitting and receiving antennas exists, the instantaneous power received at the receiving antenna, P_R, is a function of the nominal distance of direct line between the phase centers of the two antennas, i.e., d_{TR}, and can be interpreted as follows using the Friis transmission equation, e.g., [14],

$$P_R(d_{TR}) = \eta_{total} P_T G_T(\theta_T, \phi_T) G_R(\theta_R, \phi_R) G_{path}(d_{TR}), \tag{3.9}$$

where P_T is the transmitted power, $G_T(\theta_T, \phi_T)$ and $G_R(\theta_R, \phi_R)$ are the directional gains for the transmitting and receiving antennas, respectively; (θ_T, ϕ_T) and (θ_R, ϕ_R) are the zenith and azimuth angles of the signal in the coordinates of the transmitting and receiving

δ_g/λ	f_c in GHz 50Ω line	3 dB BW % 50Ω line	f_c in GHz 75Ω line	3 dB BW % 75Ω line
10^{-1}	0.8566	59.42%	0.9912	81.46%
10^{-2}	0.9685	29.65%	0.9985	38.10%
10^{-3}	0.9717	19.54%	0.9850	24.72%
5×10^{-4}	0.9752	17.40%	0.9845	21.86%

Table 3.2: The loaded relative bandwidth, $BW_{3dB}^{(L)}$, for a center-fed thin dipole of radius $a = 10^{-4}\lambda$ for different gap sizes, and loads of 50Ω and 75Ω. The impedance is from the FDTD method by Franek [34].

antennas, respectively. $G_{path}(d_{TR})$ is the "path gain" at distance d_{TR} from the transmitting antenna and is governed by the propagation environment, e.g., [96]. The antennas' losses are separated from other losses (or gains) in the Friis equation, and indicated by η_{total}, i.e., total efficiency of the transmitting and receiving antennas. For an antenna, the total efficiency factor can be broken down to the product of several other efficiency terms, e.g., as follows,

$$\eta_{total} = \eta_{pol}\eta_{imp}, \tag{3.10}$$

where η_{pol} is the polarization efficiency, η_{imp} is the impedance (mis)match efficiency. The antenna radiation efficiency (η_{rad}) accounts for the ohmic losses in an antenna and is directly embedded in the gain of the antenna [14].

The antenna efficiency incorporates directly in the power, i.e., SNR (or more specifically for digital systems, E_b/N_0) - the basic parameter for communications efficiency - is proportional to the antenna efficiency [1]. For noise-limited systems, e.g., some satellite links, the extra thermal noise introduced by the antenna ohmic resistance compounds the reduction in SNR. In such cases, the antenna efficiency can have a "double" effect on the SNR and the communications efficiency. For example a 3dB radiation efficiency may result in a reduction of the SNR by 6dB.

3.5.2 Ohmic Loss

In this part, the efficiency formulations for a wire antennas are reviewed and evaluated for the half wavelength dipole as a reference. Often, instead of center-fed dipoles, monopoles

[1]Economic metrics of communications, i.e., $\frac{C}{B} = \log_2(1 + \eta_{total}\text{SNR})$ when there is only one antenna at transmitter or receiver, $\frac{C}{B}$ is the capacity efficiency (bits/sec/Hz).

mounted on groundplanes are used and fed via a coaxial connection through the groundplane, or via a surface waveguide structure along the groundplane. The groundplane part of the antenna will contribute extra losses, and the efficiency can be expected to be lower than the equivalent dipole. The dipole structure results are optimistic for wire antennas in this sense. Losses from associated components, such as feed lines, baluns and matching circuits, also become significant, and optimal system design requires a look at all of these. For complete applications, the signal processing must also be taken into account for an optimization. Here only the antenna is addressed.

To calculate the radiation impedance, a model (or some other estimates) of the current distribution is required, e.g., [97]. Circular wire antennas are still very common owing to their simplicity, also, they have well-established theoretical basis and models. The theories are only accurate for short wires - which is luckily the practical situation - and in the case of the induced EMF method, only for impracticably thin wires. Simulation techniques all rely on models of course. For very thin wires, FDTD- and FEM-type (finite element method-type) results tend to be inaccurate and the large ratio of dimensions (large length and small "width") creates numerical problems. A similar problem occurs in moment methods, for which it also is difficult to model a practical feed.

From basic physical principles, current flow at high frequency is concentrated at the surface, e.g., [97]. This distribution influences the impedance variation with frequency, and in particular the ohmic resistance. The common simple model for the current distribution is to confine it to the skin depth, e.g., [41]. If the longitudinal antenna dimension is much larger than the cross section dimension, then the current flow direction can be taken as parallel to the long dimension. So for thin wire antennas, there is no axial current component around the wire, and this is a powerful simplification. The actual current is a maximum at the surface of the conductor and decays exponentially into the conductor, e.g., [97]. The skin depth, δ_S, is the depth of the conductor at which the current reduces to $\frac{1}{e}$ [2] or 37% of its surface value, e.g., [97, 98]:

$$\delta_S = \sqrt{\frac{2}{\omega\mu\sigma}} = \frac{1}{\sqrt{\pi f \mu\sigma}}, \tag{3.11}$$

where ω is the angular frequency, μ is the permeability and σ is the conductivity of the conductor. For a perfect electric conductor, the conductivity σ is infinite, or the resistivity is zero.

[2] e is the Euler number (also called Napier's constant), approximately 2.718281828.

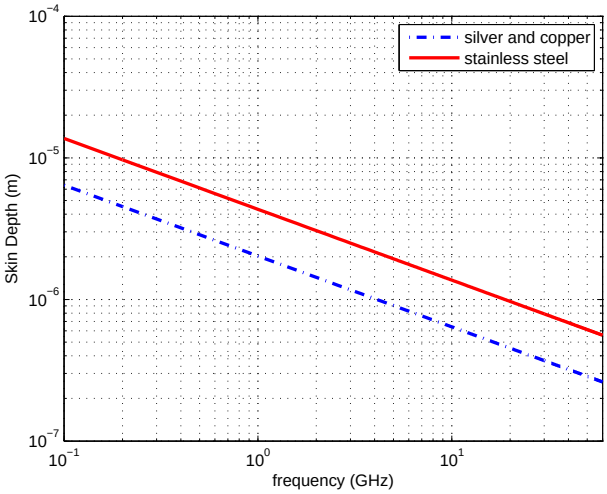

Figure 3.5: Skin depth of silver, copper and stainless steel versus frequency.

Figure 3.5 depicts the skin depth for three different conductors, silver, copper and stainless steel with conductivities of $6.17 \times 10^7 Sm^{-1}$, $5.8 \times 10^7 Sm^{-1}$ and $1.35 \times 10^7 Sm^{-1}$ respectively [99]. Silver and copper are the best metallic conductors, and their curves are indistinguishable on the scale shown. Gold (with a conductivity less than silver and copper, $4.52 \times 10^7 Sm^{-1}$) can be used for coating chip fabricated antennas for high frequencies, and here it is indicated that the skin depth is 0.5μm at 60GHz. This depth is much larger than sputtering processes produce, with each sputtering layer being in the order of 0.02μm. The inner layers of the antenna wire are much lossier, e.g. chromium or titanium (conductivities of $7.74 \times 10^6 Sm^{-1}$, $2.34 \times 10^6 Sm^{-1}$, respectively), and the supporting dielectric is very lossy as well at the high frequencies suitable for chip-mounted antennas.

Consequently, in practical constructions of chip-fabricated antennas, the skin depth is not easily achieved for a good conductor (gold) and the antennas are extremely inefficient owing to the high loss of the inner materials. Here, it is nevertheless assumed that the the skin depth is available for the good conductor. The high frequency results presented therefore represent limits, and these may not be easy to realize with chip-born antennas.

3.5.3 Skin Depth and Penetration of Electromagnetic Fields in Good Conductors

The current distribution is required to find the ohmic resistance of the dipole. Ohm's law, i.e., $\mathbf{J} = \sigma\mathbf{E}$, where $\mathbf{J}$ is the current density vector and $\mathbf{E}$ is the electric field vector, with a Maxwell's equation gives:

$$\nabla \times \mathbf{H} = (\sigma + j\omega\epsilon)\mathbf{E}, \tag{3.12}$$

where $\mathbf{H}$ is the magnetic field and ϵ is the permittivity ($\epsilon = \epsilon_r\epsilon_0$). $\omega\epsilon$ is negligible in comparison with σ in good conductors, and the displacement current is much less than conduction current. Another manipulation gives the field penetration in the form

$$\nabla^2\mathbf{E} = j\omega\mu\sigma\mathbf{E}. \tag{3.13}$$

If the electric field vector is in the z direction, (3.13) becomes

$$\frac{d^2E_z}{dx^2} = j\omega\mu\sigma E_z = \tau^2 E_z, \tag{3.14}$$

where $\tau^2 = j\omega\mu\sigma = (1+j)/\delta_S$. The complete solution is

$$E_z = C_1 e^{-\tau x} + C_2 e^{\tau x}, \tag{3.15}$$

but here C_2 is zero. C_1 can be the field at the surface if $E_z = C_{E_o}$ when $x = 0$, then

$$E_z = C_{E_o} e^{-\tau x} = C_{E_o} e^{-x/\delta_S}\ e^{-jx/\delta_S}. \tag{3.16}$$

For a wire antenna along z-axis, the Maxwell equations give the current distribution through

$$\frac{\partial^2 I_z(r)}{\partial r^2} + \frac{1}{r}\frac{dI_z}{dz} + \tau^2 I_z(r) = 0, \tag{3.17}$$

where $I_z(r)$ is the current flow parallel and in distance r to the z-axis. The boundary conditions result in the solution, e.g., [97] and [100]:

$$I_z(r) = \frac{I_0 J_0(\tau r)}{J_0(\tau a)}, \tag{3.18}$$

where J_0 is Bessel function (not to be confused with the current density on the surface, also denoted by J_0, as in the coefficient C_{J_0}), and a is the antenna radius. Numerical techniques are used here for the calculation of the Bessel function with complex argument, e.g., using Maple.

3.5.4 Ohmic Loss for a Half-Wavelength Dipole

The two cases of interest are (i) skin depth is much less than the antenna radius ($\delta_S << a$), and (ii) skin depth comparable with or larger than the antenna radius, ($\delta_S > a$). In [97] there is an analysis which yields that for $\frac{a}{\delta_S} \geq 7.55$ the modeled current distribution, $|I_z(r)/I_0| = \exp\frac{-(a-r)}{\delta_S}$, is almost exact. But for the case $\frac{a}{\delta_S} < 7.55$, the accurate current distribution should be used. It is noted here that according to [100] the asymptotic expression for current distribution is $|I_z(r)/I_0| = \sqrt{\frac{a}{r}}\exp\frac{-(a-r)}{\delta_S}$. Here, the results for the ranges mentioned in [97] are followed, the ranges are founds for which the accurate current distribution should be considered.

For the calculations here the dipole is half-wavelength ($l = \frac{\lambda}{2}$), center-fed and the gap between two arms of the dipole is very small. Three different dipole radii are considered: $\frac{\lambda}{10^2}$, $\frac{\lambda}{10^3}$ and $\frac{\lambda}{10^4}$, so the ratio of $\frac{a}{\delta_S}$ will be

$$\frac{a}{\delta_S} = \frac{c}{\Upsilon}\sqrt{\frac{\pi\mu\sigma}{f}}, \quad \Upsilon = 10^2,\ 10^3,\ 10^4, \tag{3.19}$$

where $c \approx 3 \times 10^8 m/s$ and $\Upsilon^{-1} = r/\lambda$ is the radius of the dipole in wavelengths, i.e., $r = \frac{\lambda}{\Upsilon}$. Figure 3.6 shows the $\frac{a}{\delta_S}$ for different antenna radii of $a = 10^{-2}\lambda$, $a = 10^{-3}\lambda$ and $a = 10^{-4}\lambda$ for different metals. At f=30GHz, $a = \frac{\lambda}{10^3}$, and respectively $\frac{a}{\delta_S} = 27.03$ for silver and $\frac{a}{\delta_S} = 12.64$ for stainless steel. This shows, for example, that for stainless steel (and the metals below it) with $a = \frac{\lambda}{10^3}$ at 30GHz the accurate current distribution should be considered to solve for the resistance. But for silver or copper the approximate current distribution is reliable enough. From Figure 3.6, it is inferred that for the thicker dipole of radius $a = \frac{\lambda}{10^2}$, the approximate current distribution is valid, since the $\frac{a}{\delta_S}$ is around 100, even for the worst case metal considered here, i.e., stainless steel, and highest frequency, 60GHz. But for thinner dipoles of $a = 10^{-3}\lambda$ and $10^{-4}\lambda$, the more accurate current distribution model should be used. Such thicknesses are typical of chip-fabricated monopole antennas. For 30GHz, $a = \frac{\lambda}{10^4}$, the ratios are $\frac{a}{\delta_S} = 2.703$ for silver, and $\frac{a}{\delta_S} = 1.26$ for stainless steel which means that for all these metals the accurate current distribution is required.

3.5.5 Skin Depth Much Less than the Antenna Radius ($\delta_S << a$)

When $\delta_S << a$, the current distribution is modeled as uniform within the skin depth, and zero elsewhere. So the loss in the conductor is equal to the loss of a uniform current I_0 following through a cross section with thickness of δ_S and conductivity of σ, e.g., [81]. The

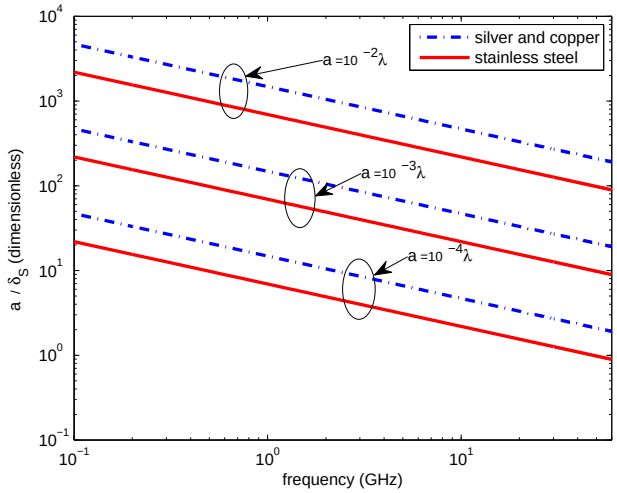

Figure 3.6: The ratio of radius to the skin depth for different antenna radii of $a = 10^{-2}\lambda$, $a = 10^{-3}\lambda$ and $a = 10^{-4}\lambda$ for different antennas materials (silver, copper and stainless steel).

radiation resistance is found by calculating the radiated power e.g., [37]. But the antenna impedance is related to three power components, the radiated power, dissipated power and stored reactive energy, e.g., [99]. If the peak current is I_0, and the antenna impedance is $Z_{antenna}$, then

$$Z_{antenna} = \frac{P_{rad} + P_{ohmic} + j2\omega(W_m - W_e)}{\frac{1}{2}|I_0|^2}, \tag{3.20}$$

where P_{rad} is the radiated power, P_{ohmic} is the dissipated power in ohmic losses, W_m and W_e are the average magnetic energy and electric energy in near field, respectively. At resonance $W_m = W_e$ and the reactance is zero. The ohmic dissipated power P_{ohmic} for a dipole of length l and radius a, with the propagation constant of k_0, can be calculated from the modeled current axial distribution as

$$P_{ohmic} = \frac{1}{2}\int_0^{2\pi} a d\phi \int_{-\frac{l}{2}}^{+\frac{l}{2}} (\frac{I_0}{2\pi a})^2 \frac{(\sin\left[k_0(\frac{l}{2} - |z|)\right])^2}{\sigma\delta_S} dz \tag{3.21a}$$

$$= \frac{I_0^2}{4\pi a\sigma\delta_S}(\frac{l}{2} - \frac{\sin(k_0 l)}{2k_0}). \tag{3.21b}$$

For a center-fed half wavelength dipole with negligible gap size the ohmic resistance is

$$R_{ohmic} = \frac{\lambda}{8\pi a\sigma\delta_S}. \tag{3.22}$$

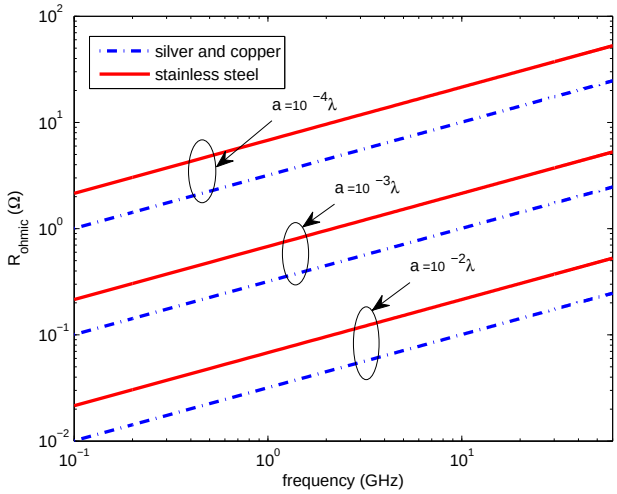

Figure 3.7: Ohmic resistance a half-wavelength dipole (the dipole radii $a = 10^{-2}\lambda$, $10^{-3}\lambda$ and $10^{-4}\lambda$) from the approximate current distribution model.

For a finite gap, δ, equation (3.21a) can be modified to

$$P_{ohmic} = \frac{1}{2}\int_0^{2\pi} a d\phi \int_{+\frac{\delta}{2}}^{+\frac{l}{2}} 2\,(\frac{I_0}{2\pi a})^2 \frac{(\sin\left[k_0(\frac{l}{2}-|z|)\right])^2}{\sigma\delta_S} dz. \tag{3.23}$$

Figure 3.7 depicts the ohmic resistance of silver, copper and stainless steel, for different thicknesses. Here, the approximate current distribution is applied, so the curves corresponding $a = 10^{-4}\lambda$ would be shifted if the calculation were done for accurate current distribution model. In general, it is observed that at frequencies below 60GHz, for a dipole with radius more than $a = 10^{-3}\lambda$, the ohmic resistance is at most 10Ω, and this is negligible comparing to the radiation resistance.

3.5.6 Skin Depth More than the Antenna Radius ($\delta_S \gtrsim a$)

In [97] the impedance from the accurate current distribution model has been calculated for the unit length. The ohmic resistance is the real part of this impedance. Using (3.18), for a half-wavelength dipole, the ohmic resistance is

$$R_{ohmic} = \text{real}(-\frac{\tau J_0(\tau a)}{2\pi a\sigma J_0'(\tau a)})\frac{\lambda}{2}. \tag{3.24}$$

In Figure 3.8 the ohmic resistance of the dipole with radius $a = 10^{-4}\lambda$ for both accurate and approximate current models has been shown. The approximate curves are the same as

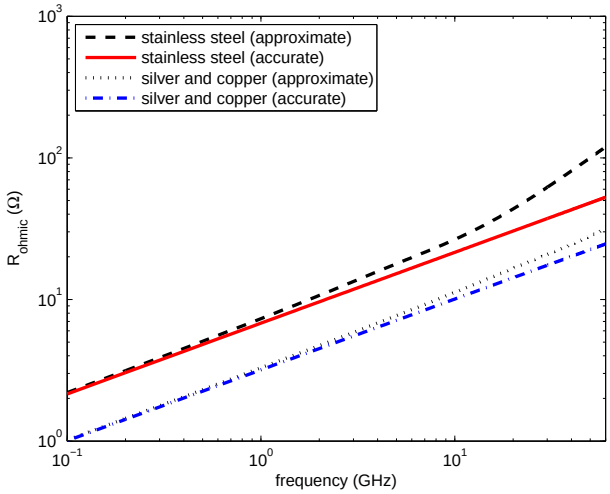

Figure 3.8: Ohmic loss a half-wavelength dipole with radius $r_0 = 10^{-4}\lambda$ from both approximate and accurate current distribution models.

the curves in Figure 3.7, but they are included in this graph for a better comparison.

The approximate current distribution model leads to higher ohmic resistance than the accurate model. For $a = 10^{-2}\lambda$ and $a = 10^{-3}\lambda$, the approximate and accurate curves are indistinguishable.

3.5.7 Efficiency Calculations

For an antenna with radiation resistance of R_{rad}, the radiation efficiency, η_{rad}, is defined in [101] as

$$\eta_{rad} = \frac{R_{rad}}{R_{rad} + R_{ohmic}}. \tag{3.25}$$

The radiation resistance, i.e, R_{rad}, of a thin center-fed half-wavelength dipole, with sinusoidal current excitation is known to be 73Ω, e.g., [37], although this value increases quickly to over 80Ω for antennas with more practical thicknesses [14]. Figure 3.9 gives the radiation efficiency for the various thicknesses. Silver and copper, even for a thickness of $a = 10^{-4}\lambda$, provide high efficiencies at 60GHz, but if the antenna is made of a less conductive metal, such as stainless steel, the efficiency for the thin dipole of $a = 10^{-4}\lambda$ at 60GHz would be around 58 percent or -2.36dB. For chromium or titanium, the efficiency is -3dB and -4.5dB respectively. Using sputtering of metals for chip-fabricated monopoles may bring this value down much more, because the sputter thickness may be less than the skin depth.

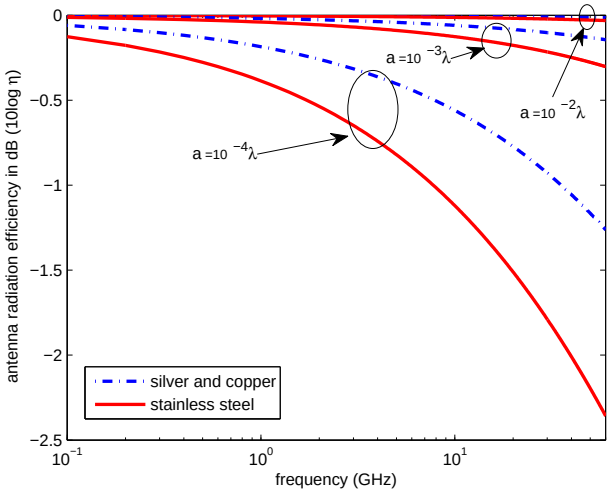

Figure 3.9: Radiation efficiency of a half-wavelength dipole in dB, for different dipole radii ($a = 10^{-2}\lambda$, $10^{-3}\lambda$ and $10^{-4}\lambda$), for copper, silver and stainless steel.

3.5.8 Ohmic Loss for a Dipole with an Excitation Gap

The ohmic dissipated power for dipole and along-axis current propagation constant $k = k_0$, i.e., the current speed along the wire is here modeled by the speed of light, whereas in practice, it is slightly slower, is calculated from the sinusoidally modeled axial current distribution and is presented in (3.21a). Therefore, for a center-fed dipole of length l and infinitesimal gap, (3.21a) gives an ohmic resistance of

$$R_{ohmic} = \frac{1}{4\pi a\sigma\delta_S}\left(\frac{l}{2} - \frac{\sin(k_0 l)}{2k_0}\right). \tag{3.26}$$

For a finite excitation gap, δ, (3.23) can be rewritten as

$$P_{ohmic} = \int_0^{2\pi} a d\phi \int_{+\frac{\delta}{2}}^{+\frac{l}{2}} (\frac{I_0}{2\pi a})^2 \frac{(\sin\left[k_0(\frac{l}{2} - |z|)\right])^2}{\sigma\delta_S} dz, \tag{3.27}$$

and the ohmic resistance will be

$$R_{ohmic} = \frac{1}{\pi a\sigma\delta_S}\left(\frac{l-\delta}{4} - \frac{\sin(k_0 l - k_0\delta)}{4k_0}\right). \tag{3.28}$$

For reference, Figures 3.10 and 3.11 show the ohmic resistance for the dipole with different gap sizes for silver and stainless steel, respectively. The resistance is insensitive to the gap size until the gap reaches the larger values, *viz.*, a tenth of a wavelength, and this effect

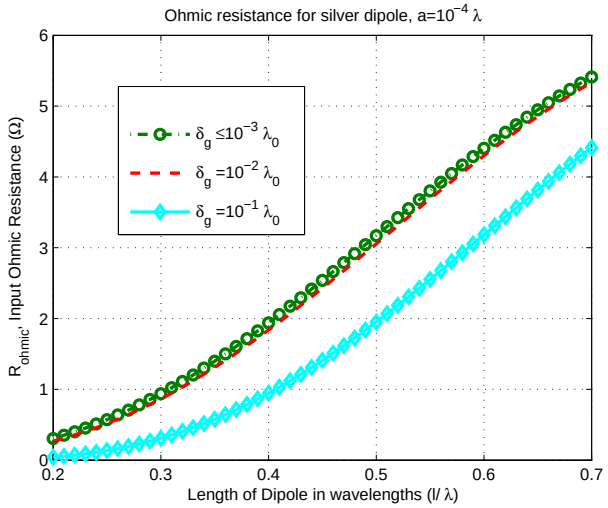

Figure 3.10: The ohmic resistance of the silver dipole with radius $10^{-4}\lambda$ and different gap sizes, operating at 1GHz.

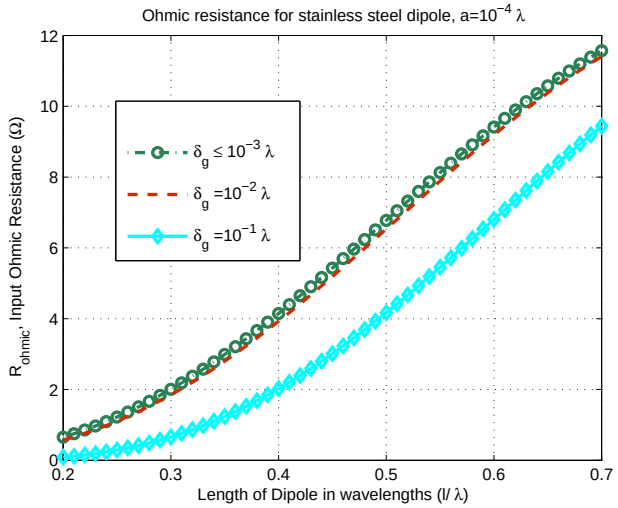

Figure 3.11: The ohmic resistance of the stainless steel dipole with radius $10^{-4}\lambda$ and different gap sizes, operating at 1GHz.

was also observed from the induced EMF method (Figure 2.6(a)). The ohmic loss formulas cannot be applied before checking the skin depth compared to the antenna thickness. If the skin depth of the antenna material is comparable with the antenna thickness, then the exact formula for the radial current distribution in the wire [97] should be applied.

3.6 Discussion

The dipole antenna has been a research topic for almost a century, and its impedance behavior and bandwidth remain topical in antenna theory. This is because the feed region modeling is a traditional challenge, and is still being researched. Accurate feed modeling has ramifications for electromagnetic solvers, which incorporate the models. There is no single solution technique for the wire dipole that gives accurate solutions over the full range of interest for the antenna theorist and practitioner.

A review of the approaches for finding the dipole impedance offers a glimpse of the variety of approaches, definitions, interpretations, and assumptions, from worldwide efforts in antenna theory and the associated electromagnetic feed modeling. The induced EMF method is the most rigorous method available, but is restricted to very thin wire structures. A finite feed gap can be modeled through a modification to the integral limits. The feed gap can be quite large (almost a tenth of a wavelength) before the resistance of the half wavelength dipole starts to change significantly. This change could be from the reduced extent of the current distribution, or from the formulation becoming suspect owing to the assumed current distribution between the separated conducting bodies. From this modified induced EMF method, new results are presented for the impedance and associated theoretical bandwidth of a lossless, thin dipole with a finite feed gap size. These results offer a benchmark for numerical techniques, and a comparison is included.

From the induced EMF results, a larger gap size leads to a larger theoretical bandwidth of the dipole. In fact the theoretical bandwidth of the finite gap thin dipole is extremely large - over 50%, and for a large gap of a tenth wavelength, about 70%. Realizing an antenna with an idealized gap, and with sufficiently thin conductors, is still a practical challenge. Nevertheless, the high bandwidth result is a promising pointer for further research into realizing the wide bandwidth with a suitable feed.

The finite conductivity of a metal can compromise the useful bandwidth of the thin dipole, particularly at high frequencies where even the best conductors become lossy, and

the known loss formulas are included.

As well as drawing on some existing numerical results, new ones are included here. The solvers used include the MOM (WIPL-D), FIT (CST), and FDTD (HFSS and Franek). Franek's FDTD results give the best agreement with those of the induced EMF method. The mathematical accuracy of the induced EMF results has been checked. But such a check is not possible with commercial solvers because the feed model details tend to be unavailable to the users. Physical measurement is in some ways the ultimate test of a theory, or a model. However, for the physical dipole, the feed region includes a physical system which is different to the gap (or no gap) feed suitable for an antenna theoretic approach. With the feed region detail dominating the input reactance, the current state of reconciling theory, simulation and measurement of dipoles has been presented.

Chapter 4

Array Factors and Uncorrelated Array Patterns

4.1 Introduction and Motivation

A phased array antenna is a combination of similar antenna elements in a specific structure to form a single antenna in order to reinforce the radiation pattern in the directions of interest, or to suppress it in undesired directions such as those featuring interference. For analysis, the simplest array comprises two isotropic antenna elements with same amplitude and same phase. A phase shifter in one branch provides a single degree of freedom for basic pattern adjustment. A phase and amplitude (or equivalently, in-phase and quadrature) weighting provides two degrees of freedom. In this chapter, simple manipulation of array patterns using a phase-only weighting is integrated for making simple MEAs for mobile communications.

Design and optimization of arrays provides the only basic guidelines for design and implementation of MEAs. In the process of designing MEAs, the coupling between elements is a key limiting factor. The mutual coupling between two ports (antennas) feeds some portion of the power of one port to the other port instead of radiating it. Reduction of the radiation power, i.e., decrease in SNR, deteriorates the radiation efficiency and eventually reduces the capacity of the wireless channel.

With simple (two- or three-element) arrays, for full spherical coverage, the correlation coefficient between the array patterns is regarded as an indication of the mutual coupling,

e.g., [14]. Therefore, uncorrelated patterns are sought to minimize the mutual coupling. Approximate orthogonality (small but nonzero correlation coefficient between patterns) is still useful in adaptive antennas in multipath scenarios. Isotropic elements in a uniform uncorrelated two-dimensional full/half plane space, i.e., the polar angles $\theta = \pi, 2\pi$, is one case which has a closed form solution.

Partial coverage is also considered. To treat the integrals of the partial coverage, accurate numerical integration methods are used with the aid of commercial software. The results for different mean angle and angular spread, show that for partial coverage, the broadside direction is more effective (lower pattern correlation) for isotropic elements than the same coverage in the endfire direction. Deploying the single degree of freedom (phase shift) in a three- (or more-) element array allows more complex patterns but brings no extra pattern orthogonality capability. The remainder of the chapter is as follows.

- The mathematical formulations of the configuration are provided in Section 4.2.
- The results for the arrays of isotropic antennas are developed and analyzed in Section 4.3.
- The directivity of the two-element linear array factor is presented in Section 4.4, demonstrating unintuitive (but explainable) results from even the simplest array.
- The chapter is summarized and the discussion is included in Section 4.5.

Mutual coupling is not treated here. For most of the configurations of interest, a relatively large element spacing is the main configuration of interest, and for this case the mutual coupling can be neglected. It is straightforward to include the impact of mutual coupling, if this is required.

4.2 Formulation of the Problem

For phased arrays (element pattern identical and oriented identically, so that there is separation of element and array patterns), the common element pattern, e.g., [91, 102], etc., is here denoted

$$\mathbf{f}(\theta, \phi) = f_\theta(\theta, \phi)\hat{\theta} + f_\phi(\theta, \phi)\hat{\phi}, \tag{4.1}$$

where $\hat{\theta}$ and $\hat{\phi}$ are the unit vectors in spherical coordinates in zenith and azimuth planes, respectively. The scalar functions $f_\theta(\theta, \phi)$ and $f_\phi(\theta, \phi)$ indicate the common (element)

pattern in directions of $\hat{\theta}$ and $\hat{\phi}$, respectively. The element pattern can be used in an array to help define coverage angles. Coverage is discussed further below. The array factor is a function of the element geometry (orientation and spacing) and the phase shifts, e.g., [98].

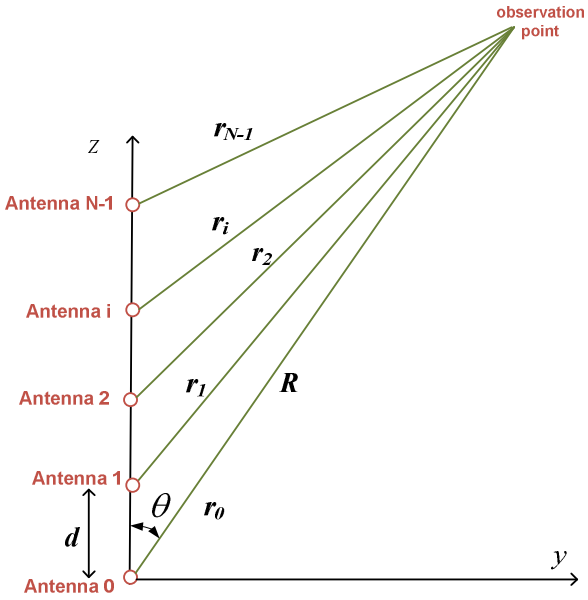

Figure 4.1: A linear array of similar, equispaced antennas along the z-axis of the Cartesian coordinates, with the same pattern, equally spaced, i.e., d.

4.2.1 Two-Element Array

Element **1** is located at the centre of the coordinate, and element **2** is at distance d along the z-axis. Figure 4.2 shows the configuration of interest for this array. Another array with a phase shift, i.e., γ, is also considered.

The phase shift can be a mechanical, purely electrical or processing operation, e.g., [38, 74]. A mechanical phase shift might be a transmission line with the electrical length equal to γ. The receiving case is considered here.

For the two arrays, four antennas, i.e., with isotropic patterns, might be used. In this case the two arrays effectively occupy twice space as one array. But the design can be economized and the same antennas can be used for both arrays. This design is perfectly implemented when there is not sufficient room to accommodate both arrays, e.g., on an electronic board. Figure 4.3 depicts the block diagram of such space-economized design

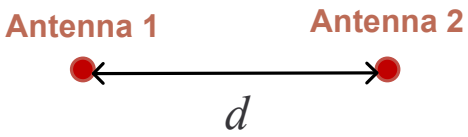

(a) Schematic 1: two-element array

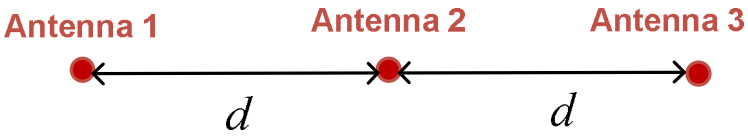

(b) Schematic 2: three-element linear array

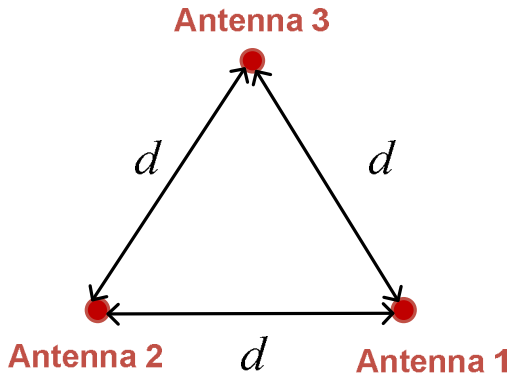

(c) Schematic 3: three-element circular array

Figure 4.2: Schematic of the configurations of the array elements: two-element, linear three-element and circular three-element arrays are considered.

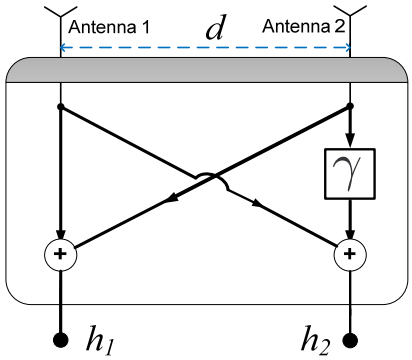

Figure 4.3: Block diagram of the beamformer.

when the two ports of the two arrays use the same elements.

The electric field pattern of the array (normalized pattern) is denoted $\mathbf{h}(\theta, \phi)$. The array patterns are denoted $\mathbf{h_1}(\theta, \phi)$ and $\mathbf{h_2}(\theta, \phi)$ for array **1** and array **2**, respectively. Here, the treatment is restricted to 2D patterns, *viz.*, the θ variable only, and the notation is limited to the scalar patterns, i.e., $h_1(\theta)$ and $h_2(\theta)$. The array factors (normalized patterns) are denoted as

$$h_1(\theta) = 1 + e^{jkd\cos\theta} \tag{4.2a}$$

$$h_2(\theta) = 1 + e^{jkd\cos\theta + j\gamma}. \tag{4.2b}$$

Orthogonality is sought between the patterns of the two arrays with respect to the spacing and the phase shift. If the coverage is uncorrelated and uniform between the angles α_1 and α_2, i.e. $\alpha_1 \leq \theta \leq \alpha_2$, and $C(d, \gamma)$ is the correlation (inner product) between the two patterns, then

$$C(d, \gamma) = \langle h_1(\theta), h_2(\theta) \rangle = h_1(\theta) \cdot h_2^*(\theta) = \int_{\alpha_1}^{\alpha_2} h_1(\theta) \cdot h_2^*(\theta) d\theta. \tag{4.3}$$

For isotropic (omnidirectional) antennas (full coverage), $\alpha_2 - \alpha_1 = 2\pi$. The correlation coefficient between the patterns, e.g., [14], is

$$\rho_{012}(d, \gamma) = \frac{\int_{\alpha_1}^{\alpha_2} h_1(\theta) \cdot h_2^*(\theta)\ d\theta}{\sqrt{\int_{\alpha_1}^{\alpha_2} h_1(\theta) \cdot h_1^*(\theta)\ d\theta \int_{\alpha_1}^{\alpha_2} h_2(\theta) \cdot h_2^*(\theta)\ d\theta}}. \tag{4.4}$$

4.2.2 Three-Element Array

The simplest three-element arrays are the equally-spaced linear and circular configurations.

Three-Element Linear Array

Under the assumption of the same amplitude and the same phase for all three antennas, all three antennas are put along the z-axis to form a three-element array. In the Cartesian coordinates, the coordinates of element **1**, element **2** and element **3** are denoted $(0, 0, -d)$, $(0, 0, 0)$ and $(0, 0, d)$, respectively, see Figure 4.2. The implementation might be with six elements, or similar to the space-economized design of Figure 4.3 for two antennas (one more antenna, i.e., one branch, is added to the configuration). A three-element linear array pattern, with no phase shifters, is

$$h(\theta) = e^{-jkd\cos\theta} + 1 + e^{jkd\cos\theta}, \tag{4.5}$$

and this is used for pattern **1**, *viz.*,

$$h_1(\theta) = e^{-jkd\cos\theta} + 1 + e^{jkd\cos\theta}, \tag{4.6}$$

and a single phase shifter can be deployed for the second array either on antenna **2** as

$$h_2(\theta) = e^{-jkd\cos\theta} + e^{j\gamma} + e^{jkd\cos\theta}, \tag{4.7}$$

or on antenna **3** as

$$h_2(\theta) = e^{-jkd\cos\theta} + 1 + e^{jkd\cos\theta+j\gamma}, \tag{4.8}$$

i.e., the phase shift may be applied to the middle or either of side elements.

Three-Element Circular Array

The element spacings (and mutual couplings) are the same for this configuration. The common element spacing is d (an equilateral triangle), i.e., Figure 4.2, so the patterns h_1 and h_2 can be written as

$$h_1(\theta) = e^{-jk\frac{d}{2}\cos\theta} + e^{jk\frac{\sqrt{3}}{2}d\sin\theta} + e^{jk\frac{d}{2}\cos\theta}, \tag{4.9a}$$

$$h_2(\theta) = e^{-jk\frac{d}{2}\cos\theta} + e^{jk\frac{\sqrt{3}}{2}d\sin\theta+j\gamma} + e^{jk\frac{d}{2}\cos\theta}. \tag{4.9b}$$

4.3 Pattern Orthogonality Results

4.3.1 Isotropic Dipole as Array Elements

Two-Element Arrays

Using h_1 and h_2 from equations (4.2a) and (4.2b), the correlation integral of equation (4.3), is

$$C(d,\gamma) = \int_{2\pi} h_1(\theta) \cdot h_2^*(\theta)\ d\theta = 2\pi(1 + J_o(kd))(1 + e^{-j\gamma}). \tag{4.10}$$

Equation (4.10) indicates that truly orthogonal patterns require a phase shift of $\gamma = \pi$ and that the orthogonality cannot be otherwise provided by changing the distance between the two antenna elements. Using equation (4.4) results in the correlation coefficient between the two patterns, $\rho_{012}(d,\gamma)$,

$$\rho_{012}(d,\gamma) = \frac{\sqrt{1 + J_o(kd)}(1 + \cos\gamma + j\sin\gamma)}{2\sqrt{1 + \cos\gamma J_o(kd)}}. \tag{4.11}$$

Here, for diversity considerations, the correlation coefficient is taken to be less than an arbitrary value of 0.5 (so the power correlation coefficient is less than about $0.5^2 = 0.25$) to mean *essentially orthogonal*.

Figure 4.4 shows the magnitude of the correlation coefficient, $|\rho|$, versus the phase shift γ, for different spacings between antenna elements. However, it is emphasized that this correlation is for the array factors and for small spacings, the mutual coupling will have an impact on physically realized antenna patterns. The curve corresponding to $\frac{d}{\lambda} = 0.5$ is below the curves corresponding to $\frac{d}{\lambda} = 10,\ 2$, and 0.1. Mathematically, this behaviour is from the oscillating Bessel functions. The correlation coefficient is depending only on the phase shift, so in order to form less correlated (but still essentially orthogonal) patterns, the phase shift must stay close to π. For hemispheric coverage, $(\alpha_2 - \alpha_1 = \pi)$, the result is the same.

A 3D plot of $|\rho|$ for a two-element array is depicted in Figure 4.5. This figure shows that increasing the spacing between the elements follows the oscillating nature of the Bessel function. When $d > \lambda$, the oscillation becomes less significant and the correlation coefficient converges. Controlling the phase shift is the only way to guarantee the orthogonality.

If the phase shifter is considered as a fixed delay line, then the (de-) correlation bandwidth (defined for the patterns being essentially orthogonal) can be taken directly from

Figure 4.4. The dashed line (for two-element array) in Figure 4.6 shows this bandwidth expressed as a relative bandwidth in percent. The figures provides the relative bandwidth that can be achieved for any desired correlation coefficient. For example, when the correlation coefficient is desired to be below some small number (close to its minimum), the phase shift window that guarantees this minimized correlation should be taken around π (a window starting before π and stopping after π), which is a narrow window of minimal decorrelation.

Partial Coverage

For partial coverage, to develop the orthogonality condition, the same approach, i.e., formulation and integration, is pursued but the limits of the integration change, e.g., α_1 and α_2. Generally there is no closed form solution to the integration of (4.4). The integration must be undertaken and solved numerically, e.g., [79].

Figure 4.7 shows cuts of the correlation coefficient function for two-element arrays. The abscissa is the element spacing and the phase shift is $\gamma = \frac{\pi}{2}$. The coverage examples are $0 < \theta < \frac{\pi}{6}$, $\frac{\pi}{6} < \theta < \frac{\pi}{3}$ and $\frac{\pi}{3} < \theta < \frac{\pi}{2}$, for all these three non-overlapping cases the beamwidth is $\frac{\pi}{6}$. For $0 < \theta < \frac{\pi}{6}$ (coverage is close to endfire) the transitions are very sharp, and very high and very low (less than 0.1) values of correlation coefficients can be found in close proximity. But for the $\frac{\pi}{3} < \theta < \frac{\pi}{2}$, close to broadside (away from endfire), the correlation coefficient behaves more smoothly as the coverage encompasses an increasing number of grating lobes. The behaviour of the correlation coefficient for the case of $\frac{\pi}{6} < \theta < \frac{\pi}{3}$ shows smoother transitions compared to the endfire case and sharper transitions compared to the broadside case. The curves converge asymptotically and the asymptotic value can be observed from Figure 4.4, see the $|\rho|$ corresponding to $\gamma = \frac{\pi}{2}$.

Three-Element Arrays in Full Coverage

For the three-element array with phase shift on one element, the correlation coefficient between h_1 and h_2 is found from (4.4). When the phase shift is on the middle element, the correlation coefficient is

$$\rho_{012}(d,\gamma) = \frac{1}{\sqrt{(J_o(2kd) + 2\cos\gamma J_o(kd) + \frac{3}{2})}} \times \frac{(J_o(2kd) + J_o(kd) + 1) + e^{-j\gamma}(J_o(kd) + \frac{1}{2})}{\sqrt{(J_o(2kd) + 2J_o(kd) + \frac{3}{2})}}. \tag{4.12}$$

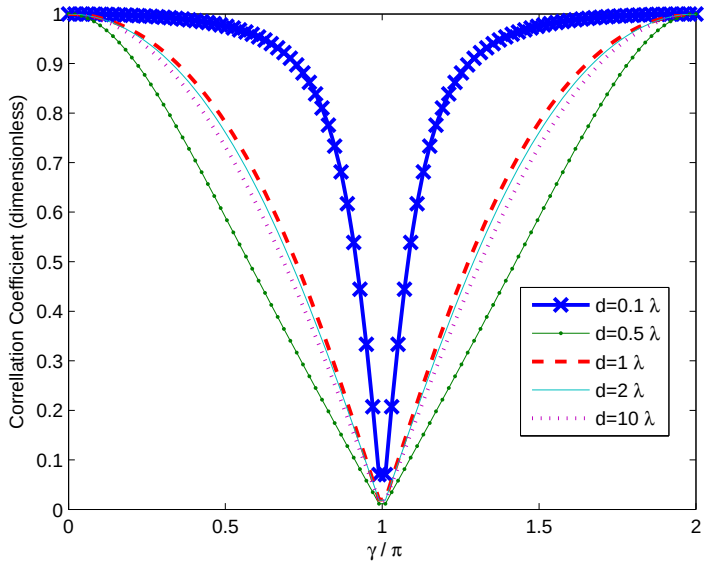

Figure 4.4: The magnitude of the correlation coefficient, $|\rho|$ of a two-element array. The correlation converges when the spacing between elements increases, e.g., $d > \lambda$.

The general form of (4.12) is related to that of the two-element array, i.e., (4.11), although for $\gamma = \pi$, the patterns are not orthogonal for the three-element array.

Figures 4.8(a) and 4.8(b) show $|\rho|$ versus spacing for the two-element and three-element arrays, respectively. The nature of the results are similar, and the peaks and oscillations follow the same trend. When the phase shift, γ, is less than $\frac{\pi}{2}$, the correlation coefficient for both two- and three-element arrays have similar patterns, but when the phase shift is more than $\frac{\pi}{2}$, $|\rho|$ of three-element array undergoes more ripples (the frequency of the ripples is almost twice more than that of the two-element case) for $d < 2\lambda$.

The dotted line in Figure 4.6 shows the decorrelation bandwidth for the three-element array. Note that for the element spacings of more than almost two wavelengths, the linear and circular three-element arrays have the same correlation bandwidth. The decorrelation bandwidth for three-element array is slightly less than the bandwidth for two-element array. For $|\rho| < 0.35$, the bandwidth is zero, while for two-element array, the double-sided bandwidth is almost 50%.

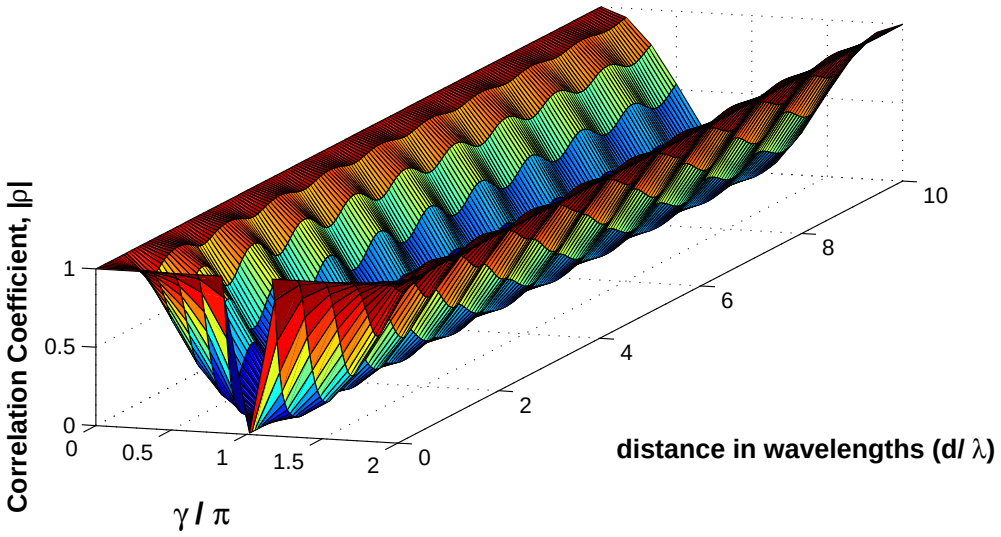

Figure 4.5: The 3D plot of the (magnitude) correlation coefficient, $|\rho|$ of a two-element array. The oscillation of the correlation coefficient is coming from the Bessel function.

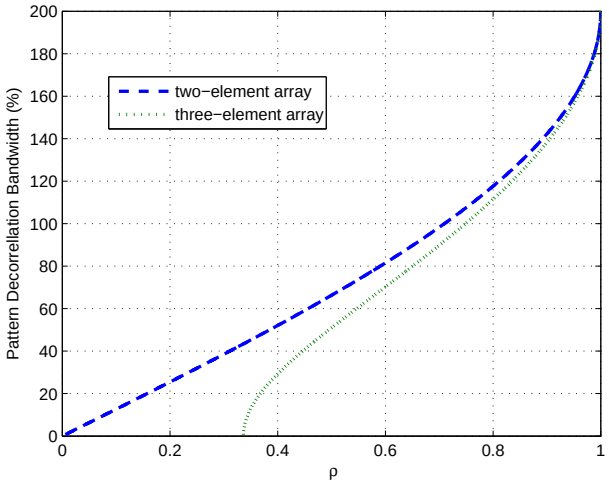

Figure 4.6: The two-sided pattern decorrelation bandwidth of the array, $d > 2\lambda$. If the phase shifter is considered as a delay line, the decorrelation bandwidth can be taken from this graph.

4.3.2 Short Electric Dipoles as Array Elements

The results presented in previous sections are all derived for isotropic elements. This is the simplest solution and determines the guideline (or the bound) for planning when directional elements are not deployed.

Here, to illustrate this with an example of directional antenna, short dipoles are considered for the antenna elements. This is a realistic assumption (dipoles are widely used in designing of arrays and MEAs, for example, see chapter 7). If a short dipole is aligned along the z-axiz, then the far-field electric pattern is $\sin\theta\hat{\theta}$. But if the dipole is perpendicular to the z-axis (on the $y-z$-plane) and along x-axis, its pattern is

$$\mathbf{h}(\theta,\phi) = \cos\theta\cos\phi\hat{\theta} - \sin\phi\hat{\phi}. \tag{4.13}$$

If two-dimensional space is considered, the dipole along the x-axis has an isotropic pattern in $y-z$-plane.

If short dipoles with element patterns are along the z-axis, the array factors (normalized patterns) for the two-element arrays are

$$h_1(\theta,\phi) = (1 + e^{jkd\cos\theta})\ \sin\theta, \tag{4.14a}$$

$$h_2(\theta,\phi) = (1 + e^{jkd\cos\theta+j\gamma})\ \sin\theta. \tag{4.14b}$$

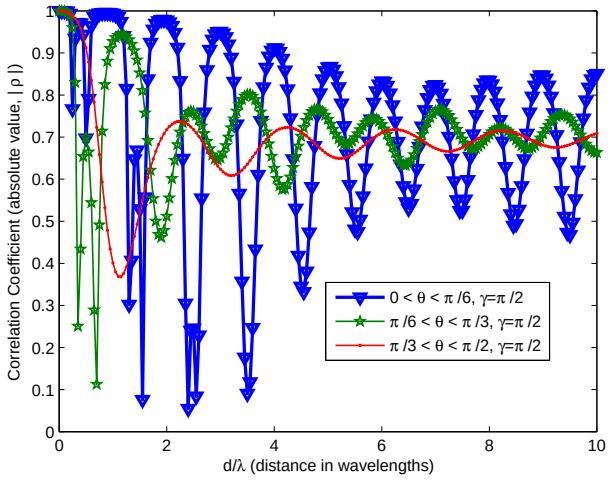

Figure 4.7: The correlation coefficient, $|\rho|$, for partial coverage and $\gamma = \frac{\pi}{2}$.

Their inner product, i.e., correlation coefficient numerator, is

$$C(d,\gamma) = \pi(1 + e^{-j\gamma})(1 + J_0(kd) - J_2(kd)), \tag{4.15}$$

where J_2 is the Bessel function of the first kind and second order. Note the extra term, i.e., second order Bessel function, compared with equation (4.10).

Figure 4.9(a) shows $|\rho|$ versus spacing for various phase shifts. If this result is compared to Figures 4.8(a) and 4.8(a), it can be inferred that using the short dipole results in smoother curves (less orthogonal or less uncorrelated). This shows that using directional antennas in the arrays, makes it more challenging to provide uncorrelated patterns.

Figure 4.9(b) depicts $|\rho|$ versus spacing for the dipole along x-axis. As mentioned earlier, the results are similar to those of Figure 4.8(a), and that is due to the isotropic pattern of the dipoles in the 2D plane, i.e, $y-z$-plane.

4.4 Directivity of Linear Array Factor

The uniform, linear array factor directivity is given by, e.g., Hansen (Chapter 5 in Collin and Zucker, 1969) [43] as

$$D_{LA}(\theta) = \frac{|F_{LA}(\theta,\phi)|^2}{(\frac{1}{4\pi})\int_0^{2\pi}\int_0^{\pi}|F_{LA}(\theta,\phi)|^2 \sin\theta \; d\theta \; d\phi}, \tag{4.16}$$

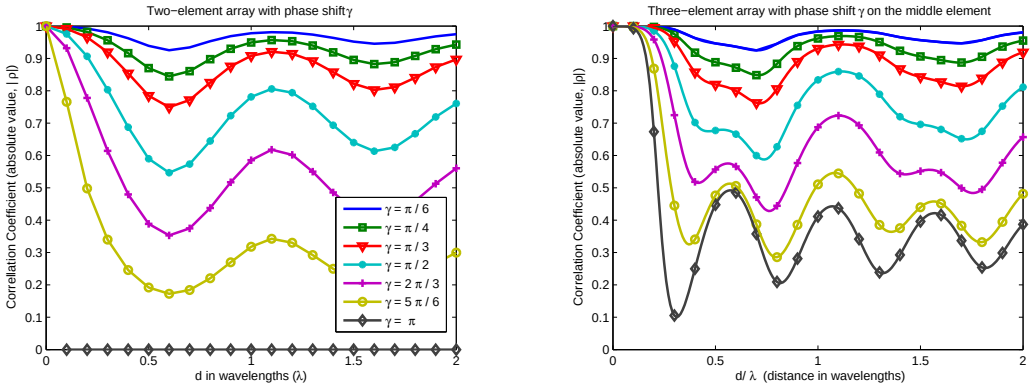

(a) two-element array of isotropic elements

(b) three-element array of isotropic elements

Figure 4.8: Pattern correlation coefficient, versus the element spacing, $\frac{d}{\lambda}$, for different values of γ, for two-element and linear three-element arrays.

$$D_{LA}(\theta) = \frac{|F_{LA}(\theta,\phi)|^2}{\frac{1}{N} + \frac{2}{N^2}\sum_{n=1}^{N-1}\frac{N-n}{nkd}\sin(nkd)\cos n\gamma}, \tag{4.17}$$

where the 2D pattern is the N-element array factor, denoted by F_{LA}, e.g., [37]

$$|F_{LA}(\theta,\phi)| = |F_{LA}(\theta)| = |\frac{\sin(N\gamma/2)}{N\sin(\gamma/2)}|, \quad \gamma = \delta + kd\cos\theta. \tag{4.18}$$

For a general element pattern, there is no simple relation between the directivity of the array factor and the directivity of the array. The array directivity is sometimes called the geometric directivity (GD). The formula shows that if the spacing is any multiple of a half-wavelength, the denominator is $1/N$ (independent of γ). Also, there is a direction (maybe more than one) for which the numerator is at its maximum value of one, and so in this direction the array directivity is equal to the number of elements [14]. (Here it is assumed that the efficiency of the antennas, i.e., η_{ant}, are unity so the gain, G, and directivity, D, are equal, in general $G = \eta_{ant}D$.) Taking two elements only, the gain resulting from the array factor can be written as:

$$D_{LA}(\theta = \pi/2) = \frac{1}{\frac{1}{2} + \frac{1}{2}\frac{\sin(kd)}{kd}} \quad \text{(broadside)}, \tag{4.19a}$$

$$D_{LA}(\theta = 0) = \frac{1}{\frac{1}{2} + \frac{1}{4}\frac{\sin(2kd)}{kd}} \quad \text{(endfire)}, \tag{4.19b}$$

and these are given in Figure 4.10. The directivity value of two is evident for the half-wavelength spacing for both cases. The maxima of the directivity reduce, along with the

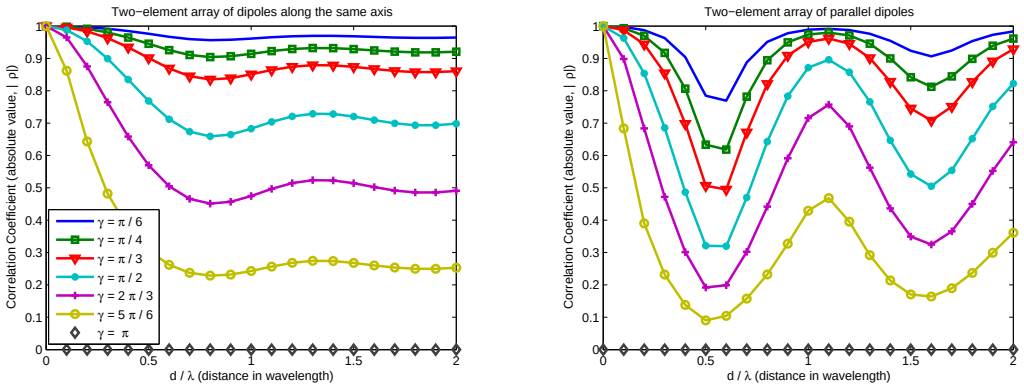

(a) two-element array of dipoles along the same axis (b) two-element array of parallel dipoles

Figure 4.9: Pattern correlation coefficient, versus the element spacing, $\frac{d}{\lambda}$, for different values of γ, for two-element arrays of short wire dipoles.

magnitude of the oscillating values in general, as the spacing increases so that the directivity approaches $N = 2$ as the spacing becomes large.

The reduction in directivity as the elements become closer, is different for the endfire and broadside cases, and other directions fall in between these cases. Because of the direction dependence, there is no definitive behaviour that can be concluded from this formulation for the general case of distributed directivity, e.g., partial coverage.

4.5 Summary and Discussion

Two- and three-element arrays with a single phase shifter have been analyzed for array pattern orthogonality. For full and hemispheric coverage, orthogonal patterns from a two-element array require a phase shift of $\gamma = \pi$. For partial coverage, the orthogonality relation is not closed form and numerical integration methods are needed. The form of the correlation coefficient is not simple (*cf.*, Figure 4.7). Endfire beams lead to smaller values of the pattern correlation coefficient compared to those at broadside. This is a design criteria for the plan and implementation of arrays. The broadside coverage provides less correlated patterns, leading to less coupling in the system.

Using directional antennas, e.g., dipoles, in the arrays, does not change the trend of the correlation. This can be interpreted as embedding (adding) weighting factors in the formulation, e.g., see for example (4.2a) and (4.14a). The example of dipole antennas,

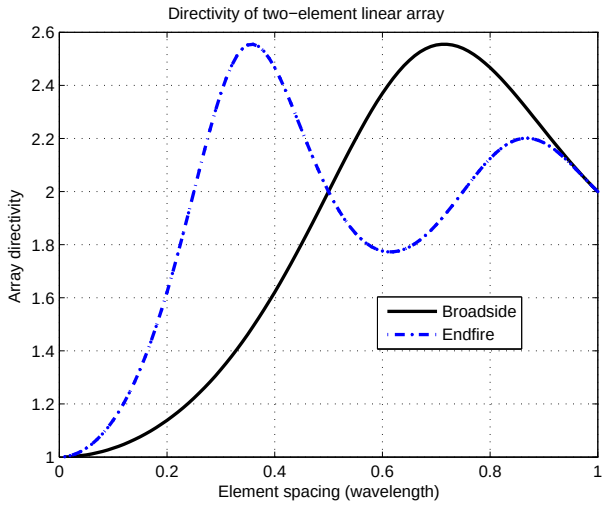

Figure 4.10: The directivity of the two-element array factor (*cf.*, an antenna with omnidirectional elements and no mutual coupling). As the spacing approaches zero, the directivity approaches that of a single element.

indicates that in a 2D plane, the parallel dipoles (perpendicular) to the plane, perform as isotropic. But when the dipoles are aligned along the same axis, the minimum of the correlation coefficient increases, i.e., higher correlation coefficient (less orthogonality).

The design configuration can be implemented for modeled or real scenarios if combined with the physics-based simulated channel for any arbitrary directional antenna pattern, see chapters 6 and 7. This approach seems to be a reliable pattern synthesis method for the real environment in case that the ray-traced (physics-based) data is accessible.

Adding another element to the array while keeping the number of phase shifters to one, which is akin to having dissimilar element patterns (an MEA, instead of an array), does not help to decorrelate the patterns, as expected from considering the phase shifter as the sole degree of freedom.

Part II

Multi-Element Antennas with Physics-Based Propagation for Mobile Communications

Chapter 5

Analysis of Physics-Based Simulation

5.1 Introduction to Physics-Based Simulated Channel

Physics-based simulation of radio channels offers a powerful technique for propagation analysis and here in **Part II**, it is used for evaluation of antennas. The situation is different to that of the measured channel. The simulated channel contains more information, including information that cannot be extracted from the measured channel. However, different processing of this synthetic data gives different results, and some of the issues are presented here.

Different ray-tracers have been developed based on different propagation mechanisms and processing and optimization criteria which results in different channels from different ray-tracers. Extraction of the channel from simulation, developing the well-suited modified code for each ray-tracer and interpreting the results are the main challenges in dealing with the physics-based simulated channels. For the research developed in this thesis, two different channels have been simulated. The simulated channels are located in Downtown Ottawa, Canada, provided by the Communications Research Centre Canada (CRC), and City centre of Braunschweig, Germany, provided by the Braunschweig Institute for Communications Technology at Technische Universität Braunschweig (BTU).

This chapter introduces physics-based simulation. Also the channel mathematical representation for this method of physical modeling is developed with and without antenna

patterns. The outline of this chapter is as follows.

- Background on channel modeling and the comparison between the most popular methods for channel signal generation are in 5.2.
- The channel representation and its formulation (suited for physical-modeling), and extraction of some geometrical information (see 5.4.1) are presented in 5.3.1.
- The channels considered and developed in this thesis, i.e., "CRC simulation" and "BTU simulation", are explained in 5.4.

The focus of **Part II** is not on interpreting the results of the ray-tracing processing. There are no measurements possible that allow a verification of ray-tracing. As environment models get more accurate, and more rays are traced (better computers are required), then it is likely that the data can be processed to be more accurate. The focus is therefore on the methods for the processing of ray data. The supplied data files are used to illustrate the results.

5.2 Background

Multipath channels have been modeled from different approaches for several decades, e.g., [103–109] (and several others, too numerous to list fully), and several simulation programs using scattering mechanisms have been developed. Software-based channel modeling is flexible and can be reliable for providing channel signals that include the effect of the antenna patterns. The goal is to provide a realistic channel. Ray-tracing is one way of channel modeling which uses geographical and built-environment data bases, along with the transmitter and receiver positions to calculate a channel impulse response, e.g., [18,19,110]. Physics-based channel modeling, i.e., ray-tracing, is fundamentally different to physical channel measurement because it is inherently averaged and filtered and this band-limiting makes it impossible to extract detail of the optical-like profile. One approach to seeking the detail is deconvolution processing (inverse filtering), but this is prone to produce erroneous profiles [111–114].

5.2.1 Methods of Channel Signal Generation

As noted in chapter 1, the channel signals can be generated using different approaches. The first is physical measurement. Here, a physical link is measured over time (or rather distance for mobile systems), and the channel signal is recorded and stored. The stored channel can be played back at different rates (velocity of a mobile terminal) in a computer, including experiments with the MEA signal combining and even digital communications configuration and parameters, e.g., [14, 115]. The stored channel is of course tied to the original measurement system and this can be limiting. For example, the antennas cannot be changed once the physical measurement has been undertaken, a new measurement would be required for a different antenna. The advantage of the stored channel is the ground-truth nature of the signal.

A second method is statistical generation of the channels. This method has the advantage of being very simple and convenient. It makes repeatable signals with precise and statistically controlled parameters, e.g., [21]. The disadvantage is the suspicion as to how realistic they are. Often, statistically generated signals are considered as overly-idealized. These channels can be stored and used in the same way as the stored channels. Statistically generated channels are widely used for comparing the performance of different communications systems, including different algorithms, etc. There is still difficulty in changing the types of antennas in the sense that the relationship between the statistically generated signals and the antenna configurations is complicated, so the approach is not very suitable for adaptive antenna design unless the full spatial propagation channel and antennas are part of the model.

The inclusion of the spatial channel defined applies physical modeling of the signal generation process, e.g., [18, 19]. Here, the physical environment is modeled along with the transmit and receive antennas. Currently, there is not the modeling technology or computation power required to do this with sufficient accuracy to "correctly" get the fine structure of the channel signals, except for canonical situations. However, the coarse structure of the signals from real-world environments can be estimated. Additionally, a fine-scale statistical component can be added to the coarse signal from the physical modeling. Of particular interest for the physical modeling is the use of existing environmental data bases such as geographic information systems (GIS) for outdoors, or computer-aided design (CAD) architectural files for some indoor situations. Radiosity can be used, but it is easier to resort to

ray theory [116], where the launching and gathering of a small number of rays approximates the propagation, and modeled or imported data for the antenna patterns are used.

5.2.2 Physical Modeling

The goal of physical modeling is the evaluation of the channel as close to the real channel as possible for predefined antenna positions by using environmental configurations. Different ray-tracers use different techniques, for example the number of calculated reflections and diffractions for each ray, and the number of rays, time and angular resolution, power threshold, time offset, rough surface scattering, and so on. This means that different simulators will give different channel data for the same geometry or "environment file". There is no standardized format of the output files, so extracting the data from different computer codes requires customized code. The data is a set of profiles of polarized complex impulse responses for each spatial channel sample. In most of the models, only two-dimensional propagation is considered for evaluating channel features. However, recently the interest has been renewed for both the elevation and azimuth domains with three-dimensional beamforming and MIMO techniques, e.g., [117]. (The three-dimensional modeling of the channel is considered increasingly in order to improve the performance of the channels via beamforming and MEA transmission or/and reception (MIMO techniques) , e.g., [117, 118].)

Ray-tracing is a powerful technique for physical modeling of the spatial or temporal behavior of the channel, i.e., the time delay is proportional to the length of the path traveled by the signal. These techniques have been optimized to minimize the calculation time and make the results similar to those of physical experiments, e.g., [18, 19]. For each receive location, a file of incident rays is created by the ray-tracer. The file typically contains the amplitude of the rays, their phase, time delay and departure and arrival angles for horizontal-horizontal (ϕ-ϕ), horizontal-vertical (ϕ-θ), vertical-horizontal (θ-ϕ) and vertical-vertical (θ-θ) polarizations. In most of the models, only two dimensional propagation is considered for evaluating channel features [119]. This is why "vertical" and "horizontal" terms have been used for the channels, and the polarization contributions are sometimes represented as 'VV', 'VH', 'HV' and 'HH'.

The simulated channels are in Downtown Ottawa including dense structure and high-rise urban buildings, and the city centre of Braunchweig, Germany, including low-rise buildings. Different ray-tracing techniques are used by the two simulators.

5.3 Basics of Mobile Channel

5.3.1 Deriving Signals from Physics-based Simulations

At a point in space, the incident waves at the mobile have the three Cartesian components of the electric field,

$$\mathbf{E_R}(\omega, \mathbf{r}) = E_x(\omega, \mathbf{r})\hat{\mathbf{x}} + E_y(\omega, \mathbf{r})\hat{\mathbf{y}} + E_z(\omega, \mathbf{r})\hat{\mathbf{z}}, \tag{5.1}$$

and similarly for the magnetic field,

$$\mathbf{H_R}(\omega, \mathbf{r}) = H_x(\omega, \mathbf{r})\hat{\mathbf{x}} + H_y(\omega, \mathbf{r})\hat{\mathbf{y}} + H_z(\omega, \mathbf{r})\hat{\mathbf{z}}, \tag{5.2}$$

where $\hat{\mathbf{x}}$, $\hat{\mathbf{y}}$ and $\hat{\mathbf{z}}$ are the unit vectors of the Cartesian coordinates; so there are six components in general. E_x, E_y and E_z denote the electric field components and H_x, H_y and H_z are the magnetic field components in Cartesian coordinates. Each component, such as E_x, is a complex scalar, and is also a function of (angular) frequency, ω, and position of the point at which the fields are determined, i.e., $\mathbf{r}$. The attention is on just the electric field of plane wave incidence because this allows the derivation of the received voltage signal of an antenna.

Two major assumptions are made for a tractable model, [14]. Firstly, the wave sources are assumed to be in the far field of the mobile antenna. This is so that plane wave analysis can be applied, which accounts for the next assumptions, including point scatters for the sources, and constant angles of arrival over a local linear trajectory. The scattering sources are assumed independent of the receiving antenna position. The electrical size of this local trajectory depends on the electrical dimensions of the physical scenario.

Both of the major assumptions seem reasonable for frequencies which are sufficiently high so there are many wavelengths between the receiving antenna and the scattering sources, and for when the receiving antennas are electrically small.

The receiving pattern includes the effects of the supporting platform. For an automobile, the platform is physically large but scatters for an outdoor scenario are also at large physical distance from the terminal. In an urban environment, the automobile itself is typically a part of the multipath environment, and this may compromise the assumption that the incident wave structure does not change over a local trajectory. Some experimental investigation on the vehicular effect is given in [120].

For handsets, the user's body may similarly compromise the assumption. At high frequencies such as 60GHz (wavelength is about 5mm), the assumption of many wavelengths separating the scatterers from the mobile antenna seems reasonable, but again, the mobile platform becomes electrically large and the far field assumption may be satisfied.

In summary, major assumptions are made regarding the nature of the radiowaves over a local trajectory of the antenna. For a given scenario, the impact of the assumptions can only be checked through full-wave electromagnetic simulation, although physical measurements can reveal some information.

The mobile antenna moves along the positive direction of a straight line, say ζ, which is in standard Cartesian space (x, y, z) and the standard polar angles (θ, ϕ) refer to this coordinate system. To deal with various physical simulator data formats, coordinate transformations are normally needed, including for polarizations.

The channel is expressed using Dirac delta functions, and such carries many assumptions and mathematical liberties. The (ray-traced) channel impulse response, say for one polarization, e.g., vertical-vertical (θ-θ), at the mobile, is the sum of the components which form the impulse response, and is expressed as (for a given carrier frequency)

$$g_{r_i}^{\theta\theta}(\Omega_D, \Omega_A, \tau) = \sum_{j=1}^{J_i} a_{ij}^{\theta\theta} e^{j\alpha_{ij}^{\theta\theta}} \ \delta(\tau - \tau_{ij}) \ \delta(\Omega_D - \Omega_{Dij}) \ \delta(\Omega_A - \Omega_{Aij}), \tag{5.3}$$

where

$$\begin{aligned} \delta(\Omega_D - \Omega_{Dij}) &= \delta(\theta_D - \theta_{Dij}) \ \delta(\phi_D - \phi_{Dij}), \\ \delta(\Omega_A - \Omega_{Aij}) &= \delta(\theta_A - \theta_{Aij}) \ \delta(\phi_A - \phi_{Aij}), \end{aligned} \tag{5.4}$$

where r_i is the position along the trajectory, *viz.*, at the ith point along r, i.e., $r = r_i$; a_{ij} is the amplitude of the jth discrete component at the ith receiver (receive location) and α_{ij} is its phase. The phase of each multipath is the result of path length times wavenumber, plus phases of the scattering, i.e., complex reflection and diffraction coefficients. For example, grazing angle reflections have a near-180° phase shift with respect to the corresponding non-reflected wave, such that they almost cancel each other out at large distances from the transmit antenna. There are J_i components at the ith mobile location, Ω is the solid angle; Ω_D and Ω_A indicate the departure and arrival solid angles, respectively, corresponding to the local coordinates of the transmit and receive antennas, respectively; i.e., $\Omega_{Dij} = (\theta_{Dij}, \phi_{Dij})$ and $\Omega_{Aij} = (\theta_{Aij}, \phi_{Aij})$, indicating, respectively, the departure and arrival solid (zenith and azimuth) angles of each ray component, and τ_{ij} is the delay of each component.

A ray-tracer typically generates only the components of one polarization (not the complete set), e.g., '$\theta\theta$' or '$\phi\phi$'. This is applicable to the acoustics case and the (unpolarized) optical case. However, a proper radiowave ray-tracing involves all four polarization-based channel combinations.

The received impulse response is represented as $g_{r_i}^{\theta\theta}(\Omega_D, \Omega_A, \tau)$, $g_{r_i}^{\phi\theta}(\Omega_D, \Omega_A, \tau)$, $g_{r_i}^{\theta\phi}(\Omega_D, \Omega_A, \tau)$ and $g_{r_i}^{\phi\phi}(\Omega_D, \Omega_A, \tau)$ for vertical-vertical (θ-θ), horizontal-vertical (ϕ-θ), vertical-horizontal (θ-ϕ) and horizontal-horizontal (ϕ-ϕ) polarizations, respectively. In general, the channel impulse response can be written as the summed-ray polarization matrix,

$$\mathbf{g}_{r_i}(\Omega_D, \Omega_A, \tau) = \begin{bmatrix} g_{r_i}^{\theta\theta}(\Omega_D, \Omega_A, \tau) & g_{r_i}^{\phi\theta}(\Omega_D, \Omega_A, \tau) \\ g_{r_i}^{\theta\phi}(\Omega_D, \Omega_A, \tau) & g_{r_i}^{\phi\phi}(\Omega_D, \Omega_A, \tau) \end{bmatrix}, \tag{5.5}$$

where the associated amplitudes and phases are denoted as $(a_{ij}^{\phi\theta}, \alpha_{ij}^{\phi\theta})$, $(a_{ij}^{\theta\phi}, \alpha_{ij}^{\theta\phi})$ and $(a_{ij}^{\phi\phi}, \alpha_{ij}^{\phi\phi})$, respectively.

The summation of the discrete scatters (summed field of equation (5.3)) is the general format that matches with the way which ray-traced channel is typically produced. This form has increasingly been adapted for formulating (modeling and fitting) the mobile channel from channel modeling and channel measurements, e.g., [121].

In a physical experiment, the delta functions (impulses) are not available. instead, the filtered versions of the impulses are stored in some data format of a stored channel. The stored channel contains undesired contributions, i.e., noise and interference from other users of the channel [122]. For the simulated channel, the noise and interference can be absent or their levels be adjusted precisely.

This channel representation is more recently referred as *double-directional* where the Tx and Rx antennas are excluded from the formulation, e.g., [20, 118, 121]. The double-directionality evaluation is the most complete method for separating (distinguishing) multipath components. Due to its excellent spatial resolution (compared to the non-directional or single-directional channel evaluation, e.g., [123–126]), the double-directional concept provides conceptually accurate estimates of the channel's multipath-richness [20].

The channel simulator (e.g., CRC simulator, BTU simulator) creates a file of incident signals at a location containing several parameters, see the parameters of equations (5.3) and (5.5). For a transmitted impulse, the response at the mobile is the incident fields,

expressed in (5.3) as the spatial spectrum of (single-polarization) electric fields,

$$\begin{aligned} &E^{\theta\theta}_{inc}(r_i;\Omega_D,\Omega_A,\tau) = \\ &\sum_{j=1}^{J_i} a^{\theta\theta}_{ij}\exp(j\alpha^{\theta\theta}_{ij})\delta(\tau-\tau_{ij})\delta(\Omega_D-\Omega_{Dij})\delta(\Omega_A-\Omega_{Aij}), \end{aligned} \tag{5.6}$$

where $E^{\theta\theta}_{inc}(r_i;\Omega_D,\Omega_A,\tau)$ indicates the incident (normalized) electric field at the antenna, corresponding to the polarization component (θ-θ). If for instance, a carrier, $e^{j\omega_C t}$, is transmitted, then the incident field is the $\omega \leftrightarrow \tau$ Fourier transform,

$$\begin{aligned} &E^{\theta\theta}_{inc}(r_i;\Omega_D,\Omega_A,\omega) = \\ &\sum_{j=1}^{J_i} a^{\theta\theta}_{ij}e^{j\alpha^{\theta\theta}_{ij}}\delta(\Omega_D-\Omega_{Dij})\delta(\Omega_A-\Omega_{Aij}) \times \left(\frac{1}{2\pi}e^{j\omega_C\tau_{ij}}\right). \end{aligned} \tag{5.7}$$

The Fourier transform is applied between the channel impulse response, i.e., summed field of equation (5.3), and scattering distribution, i.e., multipath. It is a convenient approach for finding the conditions for diversity [127, 128]. For brevity, in this equation, only the phase of each component is affected by the choice of carrier frequency. But the model is general in the sense that for each polarization, the set of $(a_{ij}, \alpha_{ij}, \underbrace{\phi_{Dij}, \theta_{Dij}}_{\Omega_{Dij}}, \underbrace{\phi_{Aij}, \theta_{Aij}}_{\Omega_{Aij}}, \tau_{ij})$ is different for different carrier frequencies.

Although the simulator generates these terms at any frequency, but a single frequency propagation channel calculation is useful for narrowband communications. So here, the major assumption is made that the frequencies of interest are within a sufficiently narrowband that the same impulse response (except for the phase of the components) holds for all the carrier frequencies of interest. This allows us to adhere to a single frequency calculation from the simulator to assess antennas and communications systems.

Now the goal is to find the signal received at an antenna. The co-polar complex amplitude gain receiving pattern, denoted $\mathbf{h}(\Omega) = h_\theta(\Omega)\hat{\theta} + h_\phi(\Omega)\hat{\phi}$, has units of m^{-1}, and for convenience, at the carrier frequency, is normalized as

$$\begin{aligned} \frac{1}{4\pi}\oint |\mathbf{h}(\Omega)|^2 \; d\Omega &= \frac{1}{4\pi}\oint \left(|h_\theta(\Omega)|^2 + |h_\phi(\Omega)|^2\right) \; d\Omega \\ &= P_\theta + P_\phi = 1, \end{aligned} \tag{5.8}$$

where P_θ and P_ϕ are the normalized power in the polarizations $\hat{\theta}$ and $\hat{\phi}$, respectively. Here, the frequency dependency of the antenna is omitted. The open circuit voltage at the antenna,

corresponding to the polarization component (θ-θ), at position r_i is

$$V_{\mathrm{O}}^{\theta\theta}(r_i,\tau) = \oint E_{inc}^{\theta\theta}(r_i;\Omega_D,\Omega_A,\tau)\cdot h_\theta^*(\Omega_A)d\Omega_A. \tag{5.9}$$

The general version would include the antenna dependence [14], as

$$V_{\mathrm{O}}^{\theta\theta}(r_i,\omega) = \oint E_{inc}^{\theta\theta}(r_i;\Omega_D,\Omega_A,\omega)\cdot h_\theta^*(\Omega_A,\omega)d\Omega_A. \tag{5.10}$$

A narrowband filter, representing the antenna, its matching circuit, and the reception electronic signal processing, has a complex amplitude baseband frequency response denoted $F_{filter}(\omega_{BB})$. The baseband frequency is $\omega_{BB} = \omega_C - \omega_r$, where ω_r is the radio frequency. The time domain response of the filter is the $\omega \leftrightarrow \tau$ Fourier transform, denoted $f_{filter}(\tau)$. For example, modeling with an ideal rectangular filter centered at ω_C and with single sided bandwidth, ω_{BW}, i.e., $\Pi_{\omega_{BW}}(\omega_C;\omega)$[1],

$$\Pi_{\omega_{BW}}(\omega_C;\omega) = \begin{cases} 1, & \omega_C - \omega_{BB} < \omega < \omega_C + \omega_{BB} \\ \frac{1}{2}, & \omega = \omega_C \pm \omega_{BB} \\ 0, & \text{otherwise} \end{cases} \tag{5.12}$$

$$F(\omega) = \Pi_{\omega_{BW}}(\omega_C;\omega) =\leftrightarrow \frac{\sin(\omega_{BW}\tau)}{\pi\tau}\cos(\omega_C\tau) = f(\tau). \tag{5.13}$$

The voltage at baseband is now

$$V_{BB}^{\theta\theta}(r_i,\omega_{BB}) = V_{\mathrm{O}}^{\theta\theta}(r_i,\omega_C-\omega_r)F(\omega_{BB}), \tag{5.14}$$

and if the filter is sufficiently narrowband and it is not possible to discriminate the different paths, this voltage can be written

$$V_{BB}^{\theta\theta}(r_i) = \int_0^\infty V_{BB}^{\theta\theta}(r_i,\tau)d\tau. \tag{5.15}$$

Similarly,

$$V_{\mathrm{O}}^{\theta\theta}(r_i) = \oint V_{\mathrm{O}}^{\theta\theta}(r_i,\tau)d\tau, \tag{5.16}$$

and this can also be seen from the Fourier transform case, where a carrier is transmitted.

[1] A rectangular function, centered at zero, with its area equal to one, is defined as

$$\Pi_{\frac{1}{2}}(t) = \begin{cases} 1, & t < |t| < \frac{1}{2} \\ \frac{1}{2}, & |t| = \frac{1}{2} \\ 0, & \text{otherwise} \end{cases} \tag{5.11}$$

	A	B	C	D	E	F	G	H
1	Delay (mus)	Azimuth-of-Departure	Elevation-of-Departure	Azimuth-of-Arrival	Elevation-of-Arrival	Doppler Shift	Amplitude (dB)	Phase (deg)
2	0.945	-20	-14.6	-114.4	14.6	0	-118.2	107.9
3	0.881	18.1	-3	134.8	49	0	-130.7	-47.2
4	0.956	-20	-14.4	-139.6	14.4	0	-121.3	155.5
5	0.987	-20	-14	-91.7	14	0	-127.8	-28.9
6	1.157	38.9	-11.9	154.6	11.9	0	-128.2	124
7	1.057	-17.1	-13	-129.2	13	0	-138.3	100.9
8	1.176	38.9	-11.7	126.1	11.7	0	-132	48
9	0.898	19	-3	177.6	43.8	0	-135.1	130.2
10	1.615	49.6	-8.5	152.4	8.5	0	-132.9	153
11	1.616	49.6	-8.5	153.5	8.5	0	-133.1	99.6
12	1.017	-20	-13.6	-159.6	13.6	0	-134.9	102.1

Figure 5.1: Sample of a ray-traced file, for one polarization component.

5.4 Scenario Description

The ray-tracing is available for sample urban environments, i.e., Downtown Ottawa, Canada, and city center of Braunschweig, Germany. Transmitting and receiving antennas are isotropic (omni-directional). The Ottawa trajectory is shaded by high-rise buildings while Braunschweig trajectory is surrounded by low-rises and trees. In Ottawa, 11351 successive points (about 340m) and in Braunschweig, 20001 (100m) successive points are sampled. The ray-tracers sweep the trajectories with the sample spacing between successive points equal to $\frac{\lambda}{10}$ for both simulators. Figure 5.1 shows a sample data file generated by CRC simulator. This file corresponds to one polarization component, i.e., for a complete processing, four polarization component should be available. The carrier frequencies are 1GHz and 5.9GHz for the Ottawa and Braunschweig simulations, respectively. The height of the antennas along the trajectory for both ray-tracers is set to be 1.5m, and the heights of transmitters (base station) are 72m and 25m for Ottawa and Braunschweig ray-tracers, respectively.

Table 5.1 summarizes the set-up for both scenarios. The maximum number of paths indicates the maximum number of ray components that is calculated at each receiver, i.e., $max(J_i)$ in (5.3). For the Ottawa ray-tracer, the power cut-off of the receiver is 150dB below the transmitted power, while for Braunschweig ray-tracer, there is no power threshold and the number of rays is limited by the total number of reflections. All azimuthal angles are presented as clockwise from North and the for example, for Ottawa, the trajectory "heading direction" is 148 degrees along the trajectory. The heading direction defines the orientation of the array[2] with respect to north and the direction of arrival indicates the

[2]A synthesis array is formed by the sampled signal along the trajectory.

direction of incidence with respect to north, so the difference between these two angles is just the incidence angle with respect to the array orientation.

Figure 5.2 shows the map for both scenarios. The maps show the density of the buildings around, i.e., the Ottawa channel is dense and the Braunschweig channel is suburban with fewer buildings around. The figures show that for both scenarios, line-of-sight rays exist[3]. The satellite view of the area is shown in Fig. 5.3 which shows the geographic map of area [17]. The red line shows the path along which the receiver is traveling, and the red dot is the transmitter located on top of one of the tall buildings. The structure of the buildings and their dimensions indicate how dense the multipath wireless channel is.

scenario description	Ottawa Downtown	Braunschweig city-center
population	888,391	243,829
carrier frequency, f_C	1GHz	5.9GHz
number of receivers	11351	20001
length of trajectory	340.53m	101.70m
Tx height, h_T	72m	25m
Rx height, h_R	1.5m	1.5m
maximum number of paths	179	752
power threshold	150dB	NA
propagation mechanism	5 reflection, 1 diffraction	reflection, scattering

Table 5.1: The configurations of the two different ray-traced scenarios in downtown Ottawa and city-center Braunschweig.

5.4.1 Extracting Geometrical Information

Some propagation parameters can be calculated from the geometrical information of the environment through the GIS for outdoor and CAD tools for indoor, as well as online maps, such as 'Google Maps' or 'Microsoft Bing'[4] [17, 129].

[3]An optical line-of-sight is suitable for optical propagation, i.e., where rays become a realistic model. A more realistic definition for a line-of-sight is when the first Fresnel zone is clear.

[4]Examples of web service applications which also provide mapping services

(a) Ottawa

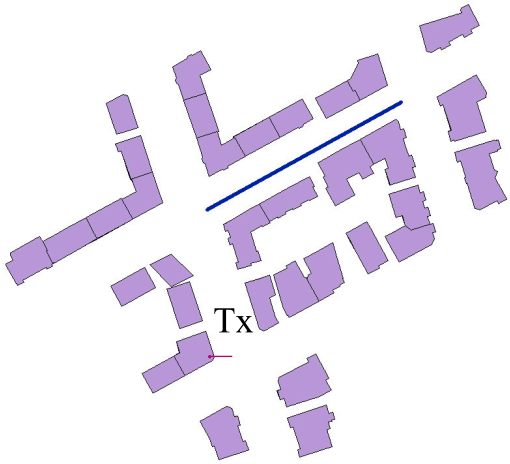

(b) Braunschweig

Figure 5.2: Scanned trajectory for Ottawa and Braunschweig ray-tracers

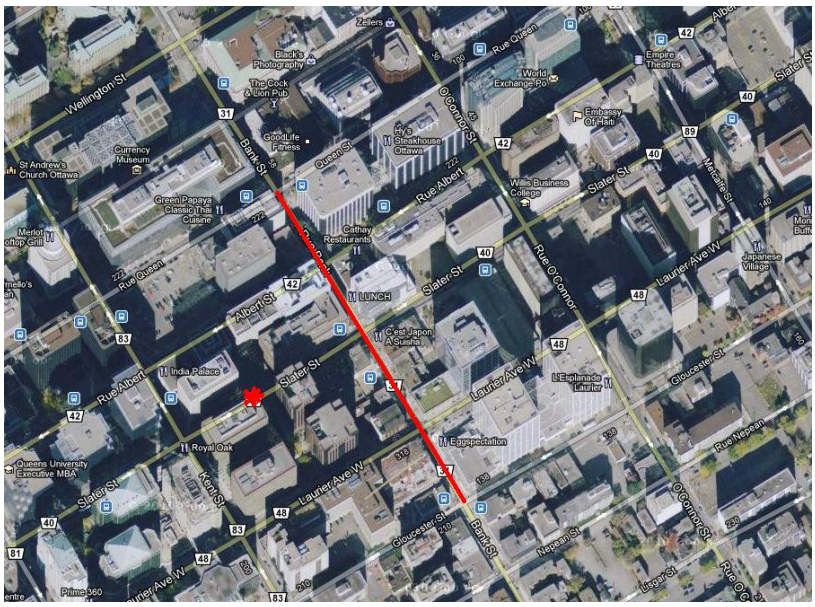

Figure 5.3: The satellite view of the trajectory and transmitter location, downtown Ottawa, ON [17].

For example, the line-of-sight (LOS) delay (time) is calculated from the geometry. The LOS time can be useful for Rice factor estimation. The LOS transmitting and receiving angles, also, enhance estimates of the transmitting and receiving angular spread.

The coordinates of all the points along the trajectory, as well as the base station are available, e.g., from the geographical data bases. The height of the transmitting antennas and the ith receiving antenna are also at hand, i.e., h_t and h_{r_i}, respectively, from a ray-tracer data file (or at least they are used to generate the file). The distance between the transmitting antenna and the ith receiving antenna is

$$d_{r_i} = \sqrt{\underbrace{(x_t - x_{r_i})}_{x_{d_i}}^2 + \underbrace{(y_t - y_{r_i})}_{y_{d_i}}^2 + \underbrace{(h_t - h_{r_i})}_{z_{d_i}}^2}, \tag{5.17}$$

where (x_t, y_t) and (x_{r_i}, y_{r_i}) are the Cartesian coordinates of the transmitting antenna (i.e., base station) and the ith receiving point, respectively.

For a specific pair of supplied files, Figures 5.4(b) and 5.4(a) show the coordinates of both receivers (green line) and the distance between transmitter and receivers (red line) for Ottawa and Braunschweig trajectories, respectively. If c is the speed of light, then the time

delay of the line-of-sight ray traveling from the transmitter to the ith receiver, is denoted

$$\tau_{i_{LOS}} = \frac{d_{r_i}}{c}. \tag{5.18}$$

Figures 5.4(a) and 5.4(b) show the coordinates and the distance between transmitter and receivers for Ottawa and Braunschweig, respectively. As mentioned earlier (section 5.3.1), for each receiver location, the set of delay components, i.e., τ_{ij}, $j = 1..J_i$, is given in the ray-traced data file. The transmitting and receiving azimuth (ϕ_T, ϕ_R), and zenith (θ_T, θ_R) angles are readily calculated for the direct line between transmitter and receiver (line-of-sight direction),

$$\phi_{T_i} = \tan^{-1}(\frac{y_{d_i}}{x_{d_i}}), \tag{5.19a}$$

$$\theta_{T_i} = \tan^{-1}(\frac{\sqrt{x_{d_i}^2 + y_{d_i}^2}}{z_{d_i}}) + \pi \mathrm{H}_{Heaviside}(-\tan^{-1}(\frac{\sqrt{x_{d_i}^2 + y_{d_i}^2}}{z_{d_i}})), \tag{5.19b}$$

and correspondingly

$$\phi_{R_i} = \pi + \phi_{T_i}, \tag{5.20a}$$

$$\theta_{R_i} = \pi - \theta_{T_i}, \tag{5.20b}$$

where the function $\mathrm{H}_{Heaviside}$ represents the Heaviside unit step function[5] and is used to correct the phase (to insure that $\theta_i \in [0, \pi]$ and $\phi_i \in [0, 2\pi]$).

The LOS delay, $\tau_{i_{LOS}}$, from (5.18), is compared with the minimum τ_{ij}, $j = 1..J_i$. For the receiving points along the trajectory that $\tau_{i_{LOS}} = min(\tau_{ij})$, a line-of-sight exists. Then the following equalities are satisfied:

$$\begin{aligned} (\theta_{Ti}, \phi_{Ti}) &= (\theta_{Dij}, \phi_{Dij}) \\ (\theta_{Ri}, \phi_{Ri}) &= (\theta_{Aij}, \phi_{Aij}). \end{aligned} \tag{5.21}$$

[5] $\mathrm{H}_{Heaviside}(x) = \int_{-\infty}^{x} \delta(s)ds$

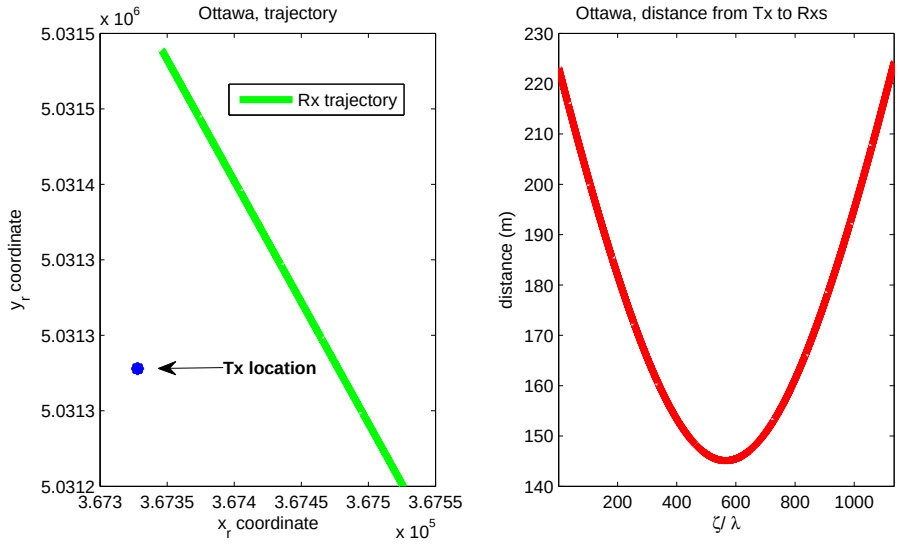

(a) Ottawa

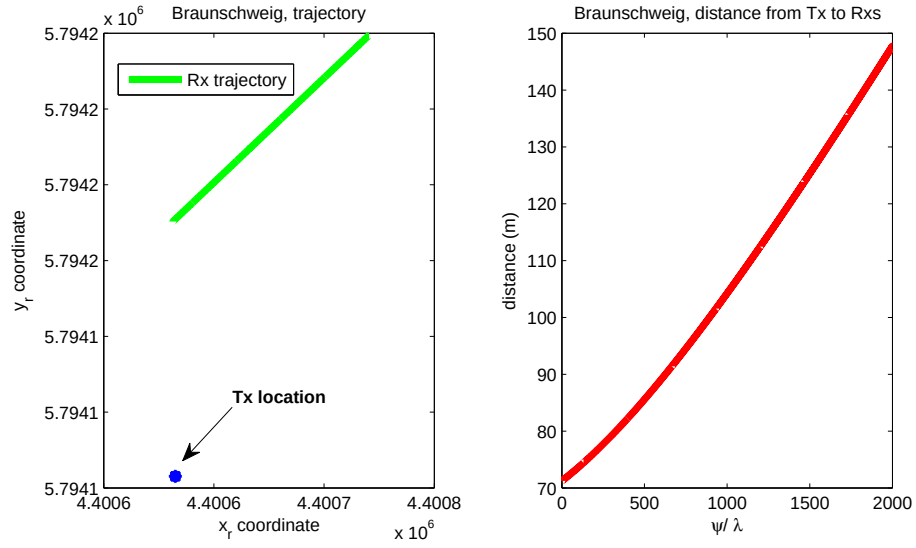

(b) Braunschweig

Figure 5.4: Cartesian coordinates and distance between transmitter and receiving points for both trajectories, i.e., Ottawa and Braunschweig.

Chapter 6

Analysis and Evaluation of the Channel Parameters

6.1 Introduction and Overview

This chapter looks into some of the important channel parameters for evaluating the channel performance. It emphasizes the interpretation of the ray-traced data file and extracting the channel parameters that cannot be evaluated from any other method. These are:

- Local mean: Local (spatial) mean of amplitude or power of the signal that is received by a (moving) receiver is perhaps the most important channel parameter. For statistical analysis of the wireless radio channel as well as power control, the local average is needed. It is also used for estimating higher moments, such as correlation coefficients.

- Power delay profile (PDP): The geometry of the physical environment and the antenna patterns govern the propagation in a wireless radio channel. The PDP shows the average effect of these obstacles [130]. In many communications systems, e.g. OFDM, noise variance and sub-channel PDPs are needed for assisting with channel estimation and frequency offset estimations [131]. The PDP has been estimated for different channel situations, including for various indoor and outdoor, car-to-car, etc., e.g., [105, 132–135].

- Delay spread (DS): Delay spread is used to predict the error probability caused by time dispersion, [122, 136]. There is no universal definition for the delay spread. Strictly,

it is the second centralized moment of the PDP, but the definition of the mean time, and the averaging detail, become important for finite data records of what is usually a non-stationary process. Because the delay spread is a moment and calculated from averaging (integrated over the PDP), it is robust to the detail of the PDP. Many attempts have been made to physically measure and model the delay spread both for indoor [137] and outdoor [138–140] scenarios.

- Correlation Coefficient: For statistical calculations of the radio coverage, it is important to characterize the accuracy of the channel power (gain) estimates. Estimating the next moment of the channel signal, i.e., the correlation coefficient, is essential for antenna (or frequency) diversity design [141].

6.2 Signal Envelope and Local Mean

6.2.1 Received Rays and Summed Field

At each receiving point (location), the ray-tracer provides a set of complex ray components, i.e., amplitude and phase of the channel taps, and the time delay, i.e., the time for each ray to reach the receiver from the transmitter, as well as the corresponding departing and arriving angles. For each polarization component, for example (θ-θ), at successive receiver locations, the amplitude of the rays (channel coefficients) versus time delay is shown in Figure 6.1. The vertical axis indicates the relative received signal amplitude intensity. The horizontal axis x indicates the time delay for each ray to arrive at that receiving point and the horizontal axis y is the distance (in wavelength) of the receiving location to the first point. (Note that all the receiving points of the trajectory have not been included in the figure in order to provide better graphical resolution.)

In the urban environment considered here, the mobile receiver (which sweeps the trajectory) is always lower than the surrounding structures, i.e., high-rise and low-rise buildings, and the signal transmitted from the transmitter, e.g., BS, is usually blocked by the surrounding structures and many copies of the signal, i.e., reflected, diffracted, refracted and scattered waves, are generated. Summing all these multipath components, i.e, waves, at the receiver results in a fast variation in the received signal [142,143]. The summed field at each

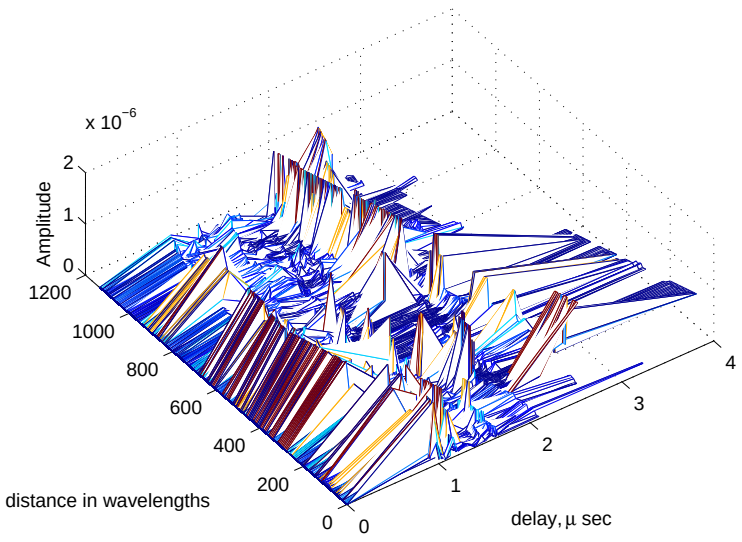

Figure 6.1: The amplitude of the rays, i.e., channel coefficients (taps), versus time delay for successive receiving points, for Ottawa trajectory (for good graphical resolution, one receiver out of every 5 successive receivers is included and a linear interpolation has been added).

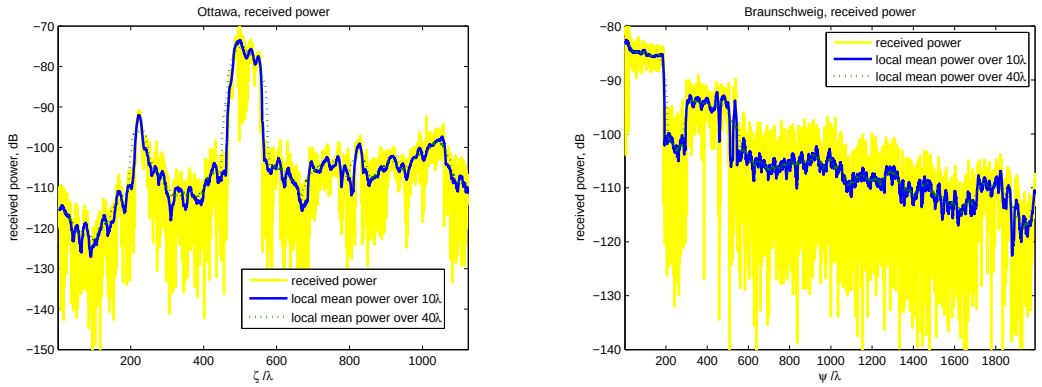

(a) Ottawa (b) Braunschweig

Figure 6.2: Summed field power and local mean for integration window lengths of 10λ and 40λ.

receiver can be denoted

$$s_{r_i}^{\theta\theta} = \sum_{j=1}^{J_i} a_{ij}^{\theta\theta} \exp(j\alpha_{ij}^{\theta\theta}) = \underbrace{\left|s_{r_i}^{\theta\theta}\right|}_{b_{r_i}^{\theta\theta}} \exp(j \underbrace{\angle s_{r_i}^{\theta\theta}}_{\beta_{r_i}^{\theta\theta}}), \tag{6.1}$$

where b_{r_i} and β_{r_i} denote the amplitude and phase of the (narrowband) summed field, respectively.

The yellow curve in Figure 6.2 is the summed field power, i.e., $\left|s_{r_i}^{\theta\theta}\right|^2$, for the Ottawa trajectory, i.e., 6.2(a), and for the Braunschweig trajectory, i.e., 6.2(b). The sharp and rapid fluctuations indicate the fading in these urban scenarios. The difference between maximum and minimum power for Ottawa is over 80dB and for Braunschweig is over 60dB. It is evident that a simple Rayleigh fading model (as used in most statistical simulations) is not accurate for this trajectory.

6.2.2 Local Mean Evaluation

Local mean (average) defined as the total received signal power (or amplitude) averaged in space, is probably the most important channel parameter. To determine some of the link features such as channel access, power control level and handoff, the local mean should be available, e.g., [144, 145]. It is a primary indication of the quality of the wireless link.

Local mean power, also called 'area-mean', or the large-scale effect, determines the power level averaged over an area of a few, or a few tens of, wavelengths. This *averaging* area is also

called "integration" area or integration distance. This ensures that the rapid fluctuations of the instantaneous received power due to multipath effects are largely removed. Typically for an urban measured channel, the integration distance ranges from 10λ to 40λ for an accuracy of about 1dB in the mean estimate [145].

The averaging is performed to remove the small-scale short-term fading from the large-scale long-term fading, i.e., channel variation [14]. (By this averaging the short-term and long-term variations of the fading channel are split.)

The variation of the small-scale short-term fading, also called multipath fading [145], occurs over very short distances, i.e., the order of the signal wavelength, and is of interest with its envelope being Rayleigh-distributed to a good approximation, i.e., levels up to 10dB above and 40dB below the mean for urban scenarios [146].

Large-scale long-term fades (path loss variation in received power) are due to power loss (due to path loss) and shadowing, and occur over relatively large distances. The large-scale fluctuation is due to changes in direct-line propagation between the transmitter (BS) and the receiver over different terrain configurations while the mobile unit is traveling. Since the propagation path is always redirected as the mobile unit is moving, the path loss also varies. It is affected by the location of the moving receiver, varies slowly and can be simplistically modeled with a log-normal distribution.

Owing to the importance of the local mean, many estimation methods have been developed for both indoor and outdoor environments, e.g., [144, 145, 147].

To calculate the local mean, the common (conventional) method is to add the ray powers or amplitudes, in a certain area, i.e., integration area, at a random receiver location, e.g., [148].

A more precise method has recently been presented to estimate the received local mean power [149]. According to numerical results, adding the ray powers, some of which may be out of phase with each other, will lead to errors. The method presented in [149], is for 2-D ray-tracing to predict the local mean by correctly summing the field contributions from a set of rays. The approach decreases the resulting errors that are caused by phase misalignment. This method focuses on the spatial average of the power received at the receiving antenna and considers the correlation between signals at different locations. The same study concludes that basically summing up the powers (common method) is acceptable if at least one of the observation domains is large (in terms of wavelength) and all the rays arriving at a point are within a sufficiently small angular range.

In this thesis, the dimensions of the ray-traced area are much larger than a wavelength, e.g., refer to table 5.1, and conventional averaging is pursued. Two major challenges in calculating the local mean are as follows, [145, 150]:

- Choosing an intermediate *averaging* window length, i.e., integration distance, is critical and depends on the surrounding structures of the channel (discussed below). If it is too short, the short-term fading will still be present, and if it is chosen too long, the long-term shadow fading effect will be overridden by the averaging process.
- The number of successive points taken for averaging is important. It should be guaranteed that the samples are dense enough (i.e., the distance between successive points is short enough) to make sure there are enough samples for averaging.

For each polarization component, e.g., (θ-θ), the narrowband summed field, i.e., received signal assuming the receiving antenna is isotropic, at the ith receiving antenna is represented in (6.1). The real part of this signal, i.e., b_{r_i} (real number), can be written as the multiplicand of two parts as follows

$$b_{r_i}^{\theta\theta} = b_{0_i}^{\theta\theta} \times m_i^{\theta\theta}, \tag{6.2}$$

where $b_{0_i}^{\theta\theta}$ is the demeaned (*quasi* Rayleigh) signal at the ith receiver, and $m_i^{\theta\theta}$ is the local mean. For the integration distance L, the estimate of local mean at the ith receiver is

$$\hat{m}_i^{\theta\theta} = \frac{1}{L} \sum_{i-\frac{L}{2}}^{i+\frac{L}{2}} b_{r_i}^{\theta\theta} \tag{6.3a}$$

$$= \frac{1}{L} \sum_{i-\frac{L}{2}}^{i+\frac{L}{2}} m_i^{\theta\theta} b_{0_i}^{\theta\theta}. \tag{6.3b}$$

If the length of L is chosen properly, the following equality is satisfied [144, 145],

$$\frac{1}{L} \sum_{i-\frac{L}{2}}^{i+\frac{L}{2}} b_{0_i}^{\theta\theta} = 1, \tag{6.4}$$

therefore, the the local mean and the local mean estimation will be the same, i.e.,

$$\hat{m}_i = m_i. \tag{6.5}$$

As mentioned, the distance between successive points has to be chosen properly to make sure the large scale variation is maintained. Here, the samples are spaced in every tenth

of wavelength, and the correlation results (discussed later in section 6.4) confirm that the samples are sufficiently dense.

Figure 6.3 shows the local mean power for integration distances 10λ and 40λ. The solid yellow graph is the received signal power. Figures 6.3(a) and 6.3(b) refer to the Ottawa and Braunschweig trajectories, respectively. The blue curve (above all the curves) is the demeaned signal, i.e., quasi-Rayleigh signal. It seems that for Ottawa, the integration distance 10λ is small and the rapid fluctuations are still present, while for Braunschweig, the integration distance 40λ loses the long-term variation of the signal. The demeaned signal, i.e., the blue curve, fluctuates with maximum 10dB above and minimum -40dB below its mean around zero dB.

According to Figure 6.2, the Ottawa channel can be regarded as case one, two and three. The Braunschweig channel can be categorized as case three and four, and for the first part of the trajectory, e.g., 180λ, the scale for path loss would be proportionally close to d^{-4} [145, 151].

6.2.3 Impact of the Integration Distance

The effect of the integration distance has been evaluated in [141] for the 2D uniform (multipath) scattering scenario. Uniform multipath scenario, also called, Clarke model, provides a simple two-path model which assumes the field incident on the receiving antenna (i.e., here, MS) is comprised of a number of azimuthal plane waves, distributed uniformly (with equal probability $\frac{1}{2\pi}$), with equal amplitude, arbitrary phase and arbitrary azimuthal angles of arrival, e.g., [104, 143, 152]. The variation of the normalized variance of the mean power or mean envelope versus integration distance is calculated and taken as the criterion to set a suitable integration distance. It has also been claimed and shown that the normalized variance of the mean power is similar to the normalized variance of the mean envelope [141], i.e.,

$$\frac{\sigma^2_{\bar{b}}}{\sigma^2_b} \approx \frac{\sigma^2_{\bar{b^2}}}{\sigma^2_{b^2}}, \tag{6.6}$$

where $\sigma^2_{\bar{b}}$, σ^2_b, $\sigma^2_{\bar{b^2}}$ and $\sigma^2_{b^2}$ are the variance of the mean (integrated) amplitude signal (summed rays for ray-traced data), the variance of the amplitude signal, variance of the mean power and the variance of the power, respectively.

For the omnidirectional, i.e., uniform, Doppler spectrum [104], the normalized variance

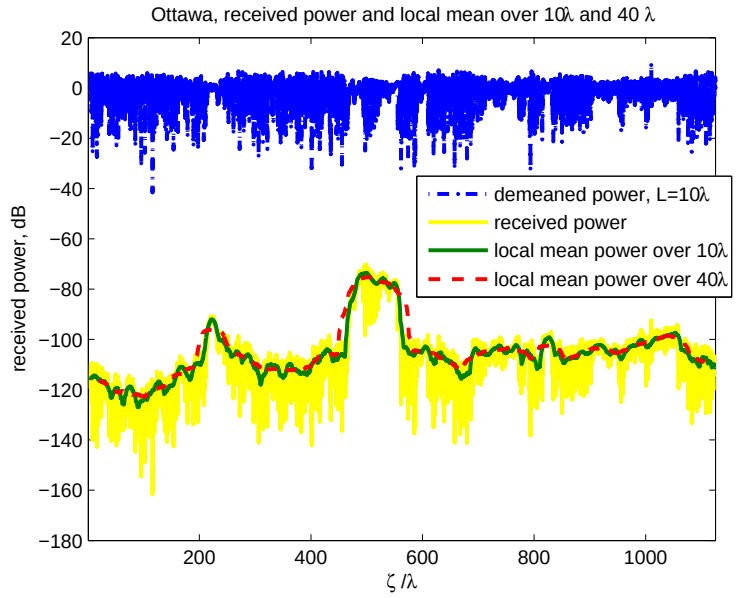

(a) Ottawa

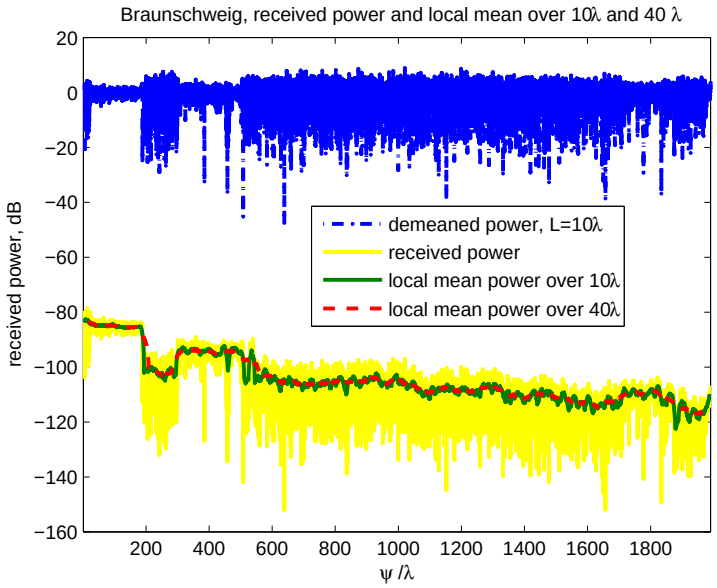

(b) Braunschweig

Figure 6.3: Received power, i.e., power of the summed field, local mean over integration distances 10λ and 40λ, and the demeaned signal (Rayleigh type) for Ottawa and Braunschweig trajectories.

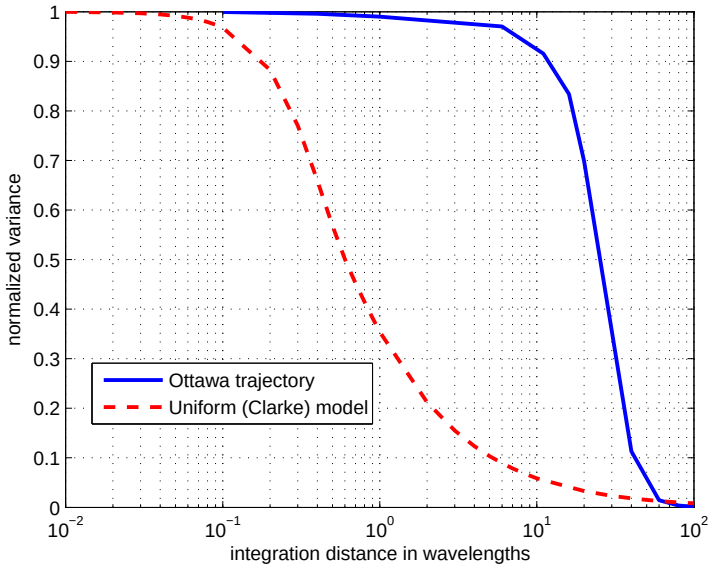

Figure 6.4: The normalized variance of the power (amplitude) of the signal which is averaged over distance in uniform (Clarke) scenario, e.g., [104], and ray-traced Ottawa trajectory. For normalized variance below 0.5, for the Ottawa trajectory, the integration distance must more than 20λ. It is seen that the simplistic Rayleigh model is very different from the physics-based modeling.

of the mean power is presented in [141] as

$$\frac{\sigma^2_{\bar{b}^2}}{\sigma^2_{b^2}} = \frac{2\lambda}{L}\int_{L/\lambda}^{0} J_0^2(k_C z)dz - J_0^2(k_C L) - J_1^2(k_C L), \tag{6.7}$$

where and J_0 and J_1 are the Bessel functions of the first kind, zeroth order and first order, respectively, and k_C is the wave number.

The normalized variance of the mean power is calculated for the Ottawa trajectory from (6.6) and the result is shown in Figure 6.4. The dashed line shown the normalized variance for the uniform (Clarke) model, calculated from (6.7). In the Clarke model, when the integration distance is 5λ, the normalized variance is below 10%. For Ottawa trajectory, it seems that the choice of $L = 40\lambda$ results in normalized variance below 10% and makes it a proper choice for integration distance.

6.3 Power Delay Profile and Delay Spread

6.3.1 Power Delay Profile for the Modeled Channel

The geometry of the surrounding area, i.e., the size, density and structure of the buildings, streets, trees, cars, etc., governs the propagation in a wireless radio channel. The power delay profile (PDP) shows the average effect of these obstructions [130]. PDP reflects the propagation environment and characterizes the channel properties. In many communications systems, e.g., OFDM, noise variance and sub-channel PDPs are required to estimate the channel and its frequency offset [131]. Many measurement techniques have been developed for it, e.g., [105,132–135], including for various indoor and outdoor, car-to-car, etc., channels.

Channel simulation inherently provides the detail, and the challenge is to find the suitable filtered version. The filtering includes the bandpass action of the transmit and receive filters, the antennas, the dispersion of the scattering environment, and finally the averaging for estimating the statistical expectation. Setting (adjusting) a sampling rate for the interpolation between the impulses is the complication of this method [27].

The PDP indicates the received signal intensity (power) in terms of time delay, i.e., by denoting the (relative) amount of received power at the receiver antenna in the time interval of $(\tau, \tau + d\tau)$ [122]. For small scale (multipath) channel modeling, the power delay profile is found by taking the spatial average of the baseband impulse response, that is $|h(t,\tau)|^2$, over a local area.

Physical measurements have indicated that a one-sided exponential function can be a suitable approximation for the PDP for some channels [122]. More generally, the PDP is claimed to be well-modeled by the sum of several delayed exponential functions, e.g., [122,135]. From recent physical measurements, typical values of the delay spread for typical urban and suburban environments range from 100ns to 3μs [122, 132, 153].

6.3.2 Delay Spread for the Modeled Channel

Delay spread is another special channel parameter. By definition, it is the variance (second centralized moment) of the PDP, but the mean time and the averaging detail should be carefully determined for finite data records of non-stationary processes. There is no universal standard definition for the delay spread.

Delay spread is a moment and calculated from integrating over the PDP. Therefore, it is

more robust to the calculation technique compared to the PDP while it can still be sensitive to the sampling/filtering. It is used to predict some features of the channel, e.g., the error probability caused by time dispersion, [122, 136].

Below, a few methods are developed to evaluate (estimate) the power delay profile and delay spread of the ray-traced, channel. These methods have not been explicitly been studied before, *cf.* [27].

Figure 6.5 shows some delays of interest for Ottawa channel. The blue solid line is the time-of-flight (TOF), i.e., τ_{TOF}, and this is the delay for the direct line between transmitter and receiver. The green dashed line is the minimum delay extracted from ray-tracer data file. It can be seen that for a small part of the trajectory, the time-of-flight and minimum delay are equal, and this is the part of the trajectory for which line-of-sight propagation exists, i.e., approximately between 450λ and 550λ. The red dashed-dotted line indicates the maximum delay at each receiver point and depends on the number of reflections and diffractions taken into account by the ray-tracer and also its power threshold. The cyan dotted line corresponds to the local mean of the unweighted delay which undergoes very sharp fluctuations. An finally, the light green solid line represents the variance of the unweighted (local) delay, second centralized moment of the set of (unprocessed) delays at each receiver. The delay spread for the whole trajectory (for the unprocessed delay) is $= 0.274\mu$sec (shown below, in section 6.3.3).

6.3.3 Local PDP and Delay Spread

The local delay spread is estimated at each receiver from the impulse response, i.e, delta functions, e.g., [14]. The local delay spread, e.g., at the ith receiver, σ_{DSi}, and its mean, $\bar{\tau}_{DSi}$, are calculated as

$$\sigma_{DSi}^2 = \frac{\sum_{j=1}^{J_i} a_{ij}^2 \tau_{ij}^2}{\sum_{j=1}^{J_i} a_{ij}^2} - \bar{\tau}_{DSi}^2, \tag{6.8a}$$

$$\bar{\tau}_{DSi} = \frac{\sum_{j=1}^{J_i} a_{ij}^2 \tau_{ij}}{\sum_{j=1}^{J_i} a_{ij}^2}. \tag{6.8b}$$

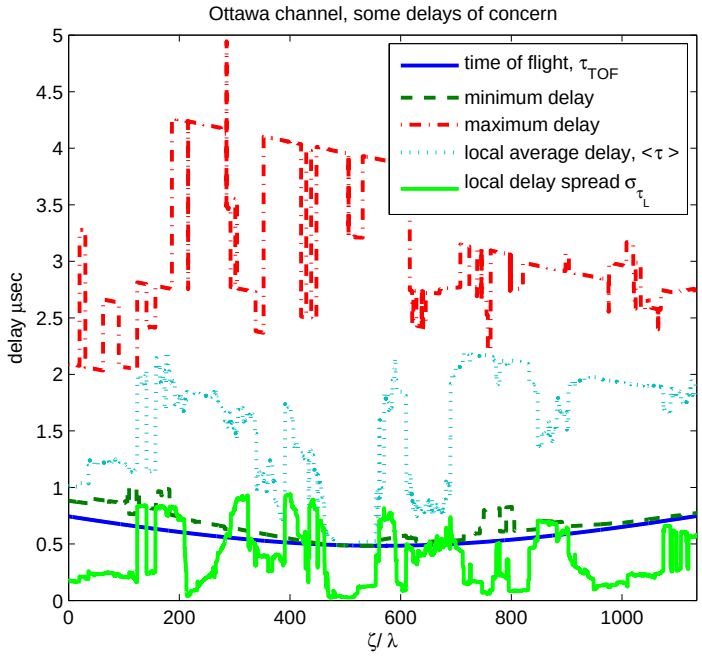

Figure 6.5: Some delays of concern.

Figure 6.6(a) and Figure 6.6(b) present the local delay spread as well as the line-of-sight (time-of-flight) delay (equation (5.18)), for the Ottawa and Braunschweig trajectories, respectively. In the Ottawa trajectory, as the receiver moves, the time-of-flight is decreasing, and when it reaches to the closest point to the transmitter, the time-of-flight reaches to its minimum value. In the Braunschweig, the receiver moves away from the transmitter and the time-of-flight increases. From Figures 6.6(a) and 6.6(b), it is inferred that local delay spread undergoes rapid and sharp fluctuations in urban dense environments while in suburban environments, e.g., Braunschweig, the local delay spread experiences smooth variation, which basically follows the time-of-flight delay trends.

To estimate the local mean delay spread, a moving window, i.e., integration distance, sweeps along the trajectory and the local mean is calculated for each window. If the integration distance is taken to include k successive receiving points, then the local mean delay

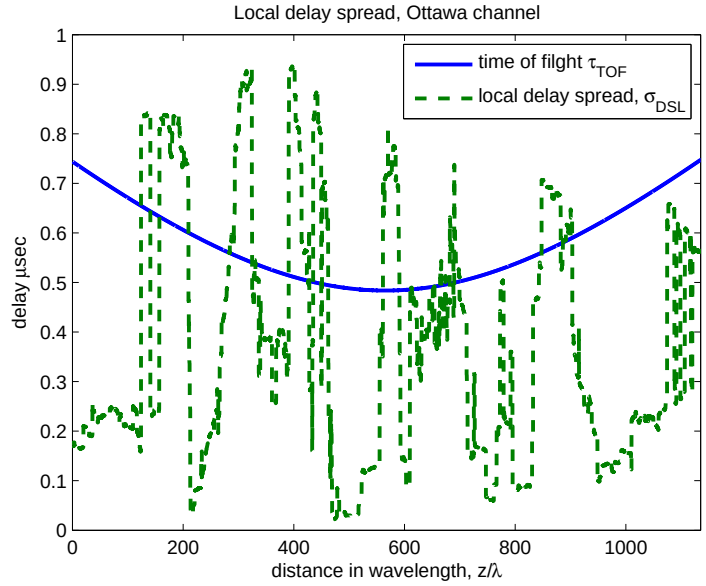

(a) Ottawa

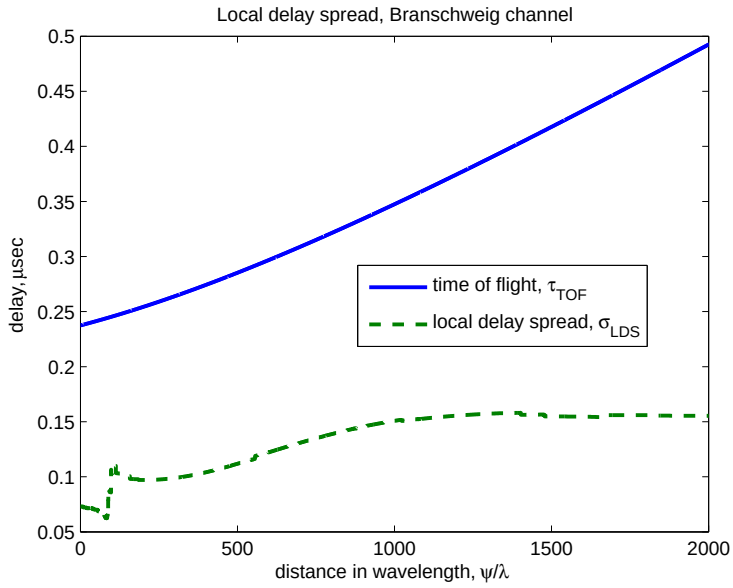

(b) Braunschweig

Figure 6.6: Local delay spread and time-of-flight for Ottawa and Braunschweig trajectories. The local delay spread undergoes rapid fluctuations for Ottawa trajectory, while for Braunschweig trajectory, the local delay spread smoothly follows the TOF and converges.

spread and its average, for the mth receiver is

$$\sigma^2_{DSL_m} = \frac{\sum\limits_{i=m-\frac{k}{2}}^{i=m+\frac{k}{2}} \sum\limits_{j=1}^{J_i} a_{ij}^2 \tau_{ij}^2}{\sum\limits_{i=m-\frac{k}{2}}^{i=m+\frac{k}{2}} \sum\limits_{j=1}^{J_i} a_{ij}^2} - \bar{\tau}^2_{DSL_m}, \tag{6.9a}$$

$$\bar{\tau}_{DSL_m} = \frac{\sum\limits_{i=m-\frac{k}{2}}^{i=m+\frac{k}{2}} \sum\limits_{j=1}^{J_i} a_{ij}^2 \tau_{ij}}{\sum\limits_{i=m-\frac{k}{2}}^{i=m+\frac{k}{2}} \sum\limits_{j=1}^{J_i} a_{ij}^2}. \tag{6.9b}$$

If the integration distance is taken as wide as the whole trajectory, the delay spread is averaged over the whole trajectory (traversed channel), i.e., $\sigma_{DSL} = \sigma_{DS}$. For the Ottawa channel, the delay spread is 0.274μsec.

A local moment, e.g., local delay spread, represents the channel that a stationary receiver would see. Designing a receiver (equalizer capability) for the delay spread is not practical. The variation of the local delay spread is large, and the receiver must work for a rapidly varying values.

6.3.4 Sampling in Time Domain (Time Binning)

An extensive channel measurement campaign was undertaken to characterize the power delay profile and the results are found in [135]. The time binning processing for measured data has been accomplished. Here, for the ray-traced channel, the time-binning method of [135] is modified and implemented to evaluate the PDP and DS. The maximum arrival time (delay) of all the rays and for all the receivers can be considered as the maximum time (timing alignment might be considered, see below). The bins might be the same size, or their sizes might adaptively be chosen, e.g., smaller bin sizes for more dense portions of the whole delay, and larger bin size for more sparse parts.

If the the maximum delay, $\tau_{max} = max(\tau_{ij})$, is partitioned in n non-overlapping sections and the bins are in equal size, $\Delta\tau$, then

$$\tau_{max} = \tau_n \tag{6.10a}$$

$$\Delta\tau = \tau_n - \tau_{n-1} = \tau_2 - \tau_1. \tag{6.10b}$$

For a higher spatial (geometrical) insight, refer to Figure 6.1. The maximum delay for the whole trajectory is readily determined. For the kth partition, the (normalized) power delay, P_k, is calculated as ($\mathrm{H}_{Heaviside}$ is the (Heaviside) unit step function, defined in section 5.4.1.)

$$P_k = \frac{\left| \sum_{i=1}^{M} \sum_{j=1}^{J_i} a_{ij} \exp(\alpha_{ij}) \mathrm{H}_{Heaviside} \left((\tau_k - \tau_{ij})(\tau_{ij} - \tau_{k-1}) \right) \right|^2}{\left| \sum_{k=1}^{n} \sum_{i=1}^{M} \sum_{j=1}^{J_i} a_{ij} \exp(\alpha_{ij}) \mathrm{H}_{Heaviside} \left((\tau_k - \tau_{ij})(\tau_{ij} - \tau_{k-1}) \right) \right|^2}. \tag{6.11}$$

If the time alignment is performed, some offset delay, τ_{offset}, is subtracted from the delay of each ray component, i.e., τ_{ij}, then the equation (6.10) is modified for the *new excess* delay as

$$\tau_{ij_{Excess}} = \tau_{ij} - \tau_{offset}. \tag{6.12}$$

The offset delay might be set (adjusted) accordingly. A few *offset* delays are suggested here.

- The time offset is set to be zero and the actual delay, i.e., τ_{ij}, is considered.
- The time offset is the time-of-flight at the ith receiver, the excess delay is the difference between the ray delay, i.e, τ_{ij}, and $\tau_{i_{TOF}}$, as

$$\tau_{ij_{excess}} = \tau_{ij} - \tau_{i_{TOF}}. \tag{6.13}$$

- The excess delay is defined as the delay for the first arriving ray, i.e., for the ith receiver, $\tau_{i_{min}} = min(\tau_{i1}, \tau_{i2}, ..., \tau_{iJ_i})$, and the excess delay is

$$\tau_{ij_{excess}} = \tau_{ij} - \tau_{i_{min}}. \tag{6.14}$$

  Therefore, for the part of trajectory which is in *line of sight (LOS)* region, the two above mentioned representations of the excess delay are the same.

Figure 6.7 shows the calculated PDP for different time (delay) offsets for the bin size 0.1μsec. The dotted line, the diamond line and solid line show the power delay profile for the cases of no-offset, offset equal to the time-of-flight and the offset equal to the minimum delay, respectively. As expected, the delay profile of no-offset takes more time to settle down. The TOF-offset starts at zero and the min-delay-offset follows it with slight time difference. The three curves are different in details and cannot be regarded *time-shifted* versions of each other, but their coarse variations may seem similar (for this example). (As the time bin

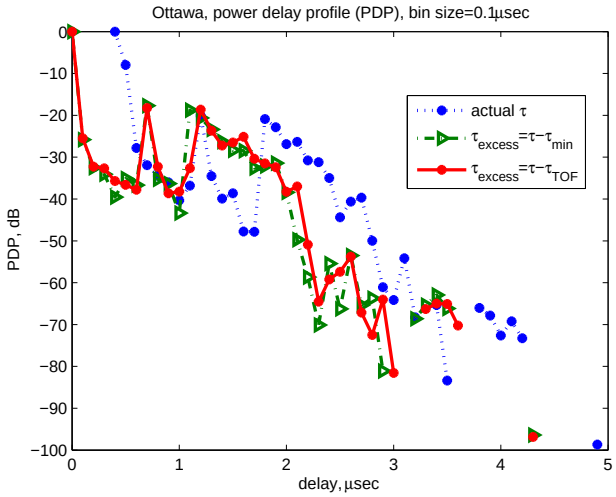

Figure 6.7: PDP for different time offset settings and bin size 0.1μsec. The PDP for three cases is considered, i.e., $\tau_{offset} = 0$, $\tau_{offset} = \tau_{min}$ and $\tau_{offset} = \tau_{TOF}$.

gets smaller, the details of different curves become more similar. On the other hand, when the time bin is chosen rather large, the PDP curves become more distinct.) In this way, the shape and variation of the PDP can be governed by bin size. If the bin size is chosen to be too small, large local variations occur with respect to the delay. For large number of samples, more software (memory) is needed, although this is seldom a biting constraint. A smaller bin size smoothes the PDP variations, but does not necessarily increase the accuracy. On the other hand, for larger bin sizes, the PDP is represented by few points and the nature of its variation would be lost.

Figure 6.8 shows the PDP for different bin sizes for the Ottawa simulation where the time offset is taken the line-of-sight delay. It is seen that decreasing the size of the bins from 0.02μsec to 0.01μsec does not change the result, but uses up twice the software resources. It is also observed that the large bin size, e.g., 1μsec, ruins the detail of the PDP, but still holds the exponentially decaying nature of the power delay profile.

Another factor that affects the delay profile is the starting point of each bin because the amount of power captured in each bin might vary by slightly moving (shifting) the bin interval.

The (local) delay spread has been calculated from the PDP of Figure 6.7 and 6.8. The resulting delay spreads are similar to Figures 6.6(a) and 6.6(b), i.e., the same peaks and

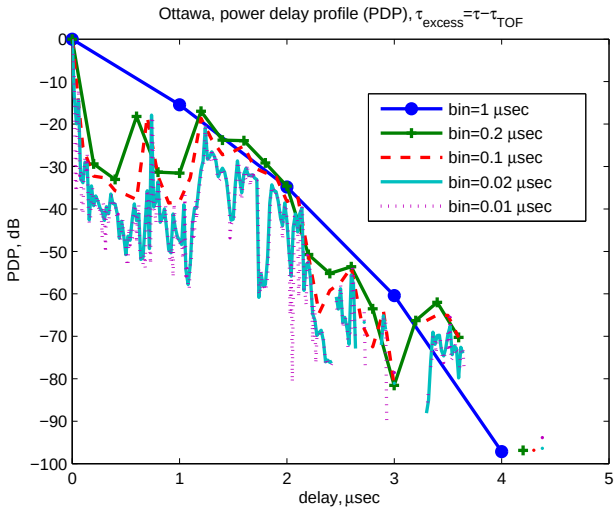

Figure 6.8: PDP evaluated via time binning for different bin sizes, bin= 0.01μsec to = 1μsec.

fluctuations. That is because delay spread is the second moment and its sensitivity is much lower than PDP.

For the Ottawa channel, the 'total' delay spread for different bin sizes (i.e., sampling rate) and for different time delay offsets is presented in Table 6.1. The results show that the delay spread for no-offset of delay alignment is less sensitive to the bin size variations, while for two other cases, the decreasing size of the bin from 1μsec to 0.01μsec can affect delay spread by up to 8%. In presenting results like this, it is evident that the bin size must be mentioned.

bin size μsec	DS, μsec actual τ	DS, μsec $\tau = \tau - \tau_{min}$	DS, μsec $\tau = \tau - \tau_{TOF}$
1	0.2080	0.1744	0.1677
0.2	0.2110	0.2212	0.2335
0.1	0.2124	0.2400	0.2365
0.02	0.1931	0.2414	0.2478
0.01	0.1978	0.2334	0.2470

Table 6.1: Delay spread for different bin sizes and different time (delay offset), for the PDP calculated from equation (6.11).

6.3.5 Filtering and Sampling

To synthesize a continuous PDP, interpolation of the local power profile is required. The interpolation is applied to transform the train of (discrete) delta functions to the continuous time dependent power profile. Passing the signal through a low-pass filter results in continuous (interpolated) signal in the time domain. Then the sampling is performed to represent a digital (quantized) version of the signal. The sampling process is similar to binning process, see section 6.3.4.

At the first stage, the local delay profile is filtered through a low-pass filter, denoted $x(t)$ in the time domain and $X(f)$ in the frequency (Fourier) domain, i.e.,

$$X(f) \overset{F^{-1}}{\rightarrow} x(t). \tag{6.15}$$

As an example of a low-pass filter, $x(t)$ is assumed to be the ideal 'rect' function, centered at $f = 0$, with the cut-off frequency $\frac{f_c}{2}$ at each side, and a total bandwidth of f_c. $X(f)$ is shown as

$$X(f) = \Pi(\frac{f}{f_c}). \tag{6.16}$$

Then the output of the filter at the ith receiver, y_{r_i}, is

$$y_{r_i}(\Omega_D, \Omega_A, \tau) = g_{r_i}(\Omega_D, \Omega_A, \tau) * x(\tau), \text{ time domain representation} \tag{6.17a}$$

$$Y_{r_i}(\Omega_D, \Omega_A, f) = G_{r_i}(\Omega_D, \Omega_A, f) \times X(f), \text{ frequency domain representation} \tag{6.17b}$$

where '$*$' is the convolution operator and $G_{r_i}(\Omega_D, \Omega_A, \omega)$ is the Fourier transform of the narrow-band time domain (local) impulse response of the channel at the ith receiver, $g_{r_i}(\Omega_D, \Omega_A, \tau)$, see (5.3). The continuous output of the low-pass filter is denoted as

$$y_{r_i}(\Omega_D, \Omega_A, t) = \ f_c \sum_{j=1}^{J_i} \ a_{ij} \ \exp(j\alpha_{ij}) \ \mathrm{sinc}\left(f_c\left(t - \tau_{ij}\right)\right). \tag{6.18}$$

The 'sinc' function and 'rect' function are Fourier pairs, i.e.,

$$\Pi(\frac{f}{f_c}) \overset{F^{-1}}{\rightarrow} f_c \mathrm{sinc}(f_c t), \tag{6.19a}$$

$$\mathrm{sinc}(t) = \frac{\sin(2\pi f_c t)}{\pi f_c t}. \tag{6.19b}$$

Any *practical* low-pass filter can be used as $X(f)$ in (6.17) for a measured or physically modeled channel. The 'rect' function is used here as an example of a mathematically standard and convenient form for developing and explaining the approach.

The next processing is the sampling. For the continuous interpolated filtered signal, $y_{r_i}(\Omega_D, \Omega_A, t)$, the PDP can now be evaluated at any desired sampling rate (corresponding to the bin size in time domain). If the filtered signal $y_{r_i}(\Omega_D, \Omega_A, t)$ is sampled at the sampling rate f_S, the sampled signal, denoted $y_{S_{r_i}}$, is

$$y_{S_{r_i}}(\Omega_D, \Omega_A, t) = y_{r_i}(\Omega_D, \Omega_A, t) \sum_{n=-\infty}^{\infty} \delta(t - \frac{n}{f_S}) \tag{6.20a}$$

$$= \sum_{n=-\infty}^{\infty} y_{r_i}(\Omega_D, \Omega_A, \frac{n}{f_S})\delta(t - \frac{n}{f_S}), \tag{6.20b}$$

$y_{S_{r_i}}$ is a sum of delta functions that have magnitudes equal to the value of $y_{r_i}(\Omega_D, \Omega_A, t)$ at the time instants the delta functions occur.

The effect of filter bandwidth and sampling rate on the behaviour, i.e., shape and variation, of the PDP and delay spread cannot be predicted intuitively. For the fixed filter bandwidth of $f_C = 20$MHz, the impact of the sampling rate on the PDP is shown in Figure 6.9. Figures 6.9(a) and 6.9(b) represent the PDP for the Ottawa and Braunschweig simulations, respectively. The low sampling rate, e.g., $f_s = 1$MHz, is an improper choice for both channels, because the sampling time, i.e., $\frac{1}{f_S}$, will be 1μsec, and this is comparable to the channel signal time, and therefore, the detail of the PDP would be lost in sampling. However, increasing the sampling rate after some threshold does not improve the precision of the estimation. From Figure 6.9, the sampling rate about (and more than) 10MHz is suitable for Ottawa simulation while for Braunschweig simulation, the sampling rate more than 5MHz keeps the detail of the profile. Figure 6.10 illustrates the impact of the sampling rate on the delay spread for both simulated channels. The sampling rate and filter bandwidth should be chosen accordingly, i.e., when the sampling rate approaches the bandwidth, the delay spread diverges. There are some challenges in applying this method. Compared to the other approaches, e.g., time binning, this technique (filtering and sampling) is more robust, and the resulting PDP and delay spread are not sensitive to the alignment of the intervals. For the Ottawa simulation, sampling rates below 10MHz, result in ripples when the bandwidth exceeds 1MHz, while for the Braunschweig simulation, the ripples are found in DS corresponding to the sampling rate 1MHz, and the bandwidth above 10MHz.

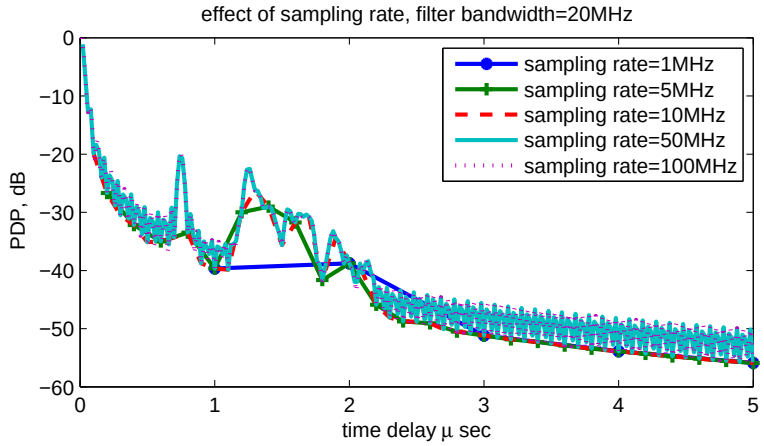

(a) Ottawa

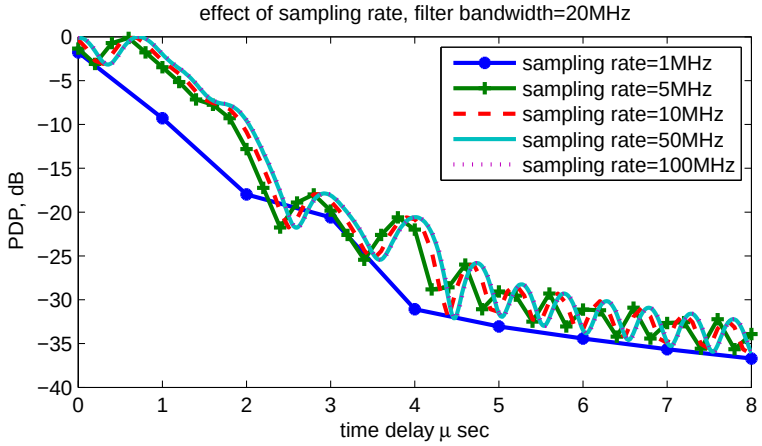

(b) Braunschweig

Figure 6.9: PDP for a fixed bandwidth and different sampling rates

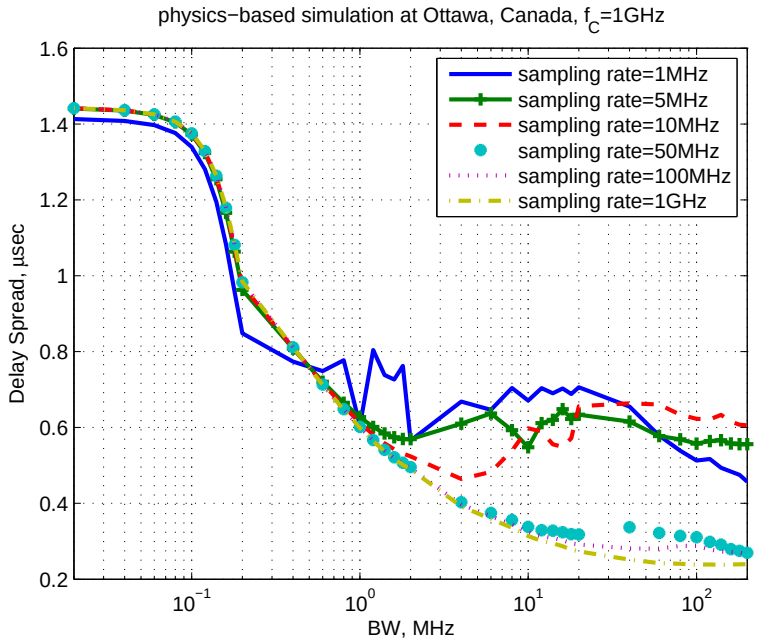

(a) Ottawa

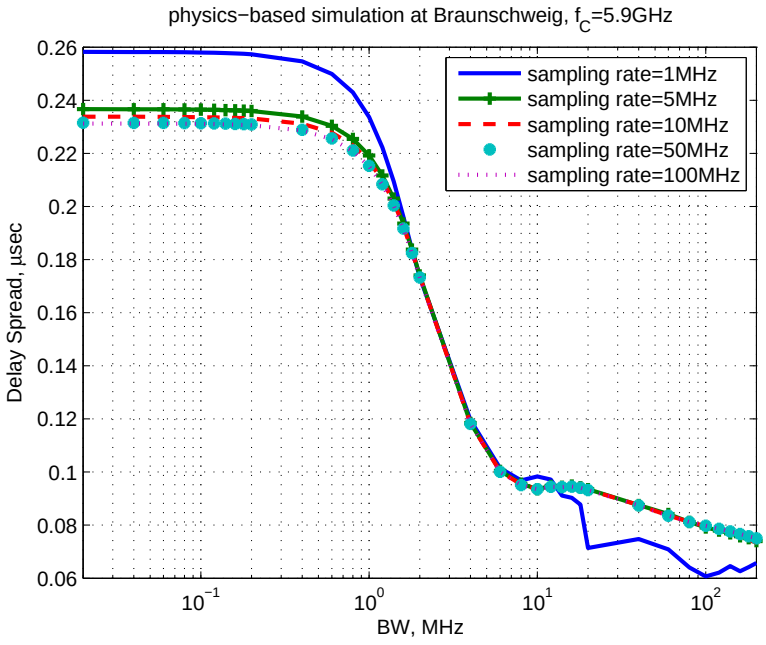

(b) Braunschweig

Figure 6.10: Delay spread for varying filter BW and different sampling rates

6.4 Cross-Correlation

6.4.1 Correlation Distance

The cross-correlation coefficient is another important channel parameter. This parameter must be estimated for channel and antenna evaluations especially when the diversity/MIMO is involved. In a wireless multipath channel the spatial cross-correlation function shows the effect of mutual coupling between the antennas (at both the transmitter and receiver) [146]. The cross-correlation coefficient function shows the correlation distance which is a criterion for determining the required spacing between antennas for MIMO and diversity [146].

For a single polarization, the cross-correlation coefficient, $\rho_{m,n}$, between the narrowband signals at the mth and the nth receivers is (the superscript denoting the polarization component is omitted for the sake of brevity),

$$\rho_{m,n} = \frac{\left\langle s_{r_m} \cdot s^*_{r_n} \right\rangle}{\sqrt{\left\langle |s_{r_m}|^2 \right\rangle \left\langle |s_{r_n}|^2 \right\rangle}}. \tag{6.21}$$

where '$\cdot$' denotes the dot product, i.e., scalar product, and the operand $\langle\ \rangle$ is taking the ensemble (over all measured or simulated points) average. The cross-correlation coefficient of the demeaned or local mean signals is also estimated for some channel applications. For the demeaned signal, the cross-correlation coefficient can be written as

$$\rho_{DM_{m,n}} = \frac{\left\langle b_{0_m} \cdot b^*_{0_n} \right\rangle}{\sqrt{\left\langle |b_{0_m}|^2 \right\rangle \left\langle |b_{0_n}|^2 \right\rangle}}, \tag{6.22}$$

where b_{0_m} and b_{0_n} are the demeaned signal (envelope) at mth and nth receivers, respectively. The cross-correlation coefficient is also defined and evaluated between the signals of different polarizations. The equations (6.21) and (6.22) are modified slightly as follows, for example, if the cross-correlation coefficient between two points of polarization components '$\theta\theta$' and '$\theta\phi$' is sought,

$$\rho_{\theta\theta,\theta\phi}(\underbrace{m,n}_{\Delta\zeta=m-n}) = \frac{\left\langle s^{\theta\theta}_{r_m} \cdot s^{\theta\phi *}_{r_n} \right\rangle}{\sqrt{\left\langle \left|s^{\theta\theta}_{r_m}\right|^2 \right\rangle \left\langle \left|s^{\theta\phi}_{r_n}\right|^2 \right\rangle}}. \tag{6.23}$$

The amplitude of the zero-lag, i.e., $\Delta\zeta = 0$, cross-correlation coefficients of the received

signal for Ottawa simulation are calculated as follows,

$$
\begin{aligned}
&|\rho_p(\Delta\zeta = 0)| \\
&= \begin{bmatrix} |\rho_{\theta\theta,\theta\theta}(0)| & |\rho_{\phi\theta,\theta\theta}(0)| & |\rho_{\theta\phi,\theta\theta}(0)| & |\rho_{\phi\phi,\theta\theta}(0)| \\ |\rho_{\theta\theta,\phi\theta}(0)| & |\rho_{\phi\theta,\phi\theta}(0)| & |\rho_{\theta\phi,\phi\theta}(0)| & |\rho_{\phi\phi,\phi\theta}(0)| \\ |\rho_{\theta\theta,\theta\phi}(0)| & |\rho_{\phi\theta,\theta\phi}(0)| & |\rho_{\theta\phi,\theta\phi}(0)| & |\rho_{\phi\phi,\theta\phi}(0)| \\ |\rho_{\theta\theta,\phi\phi}(0)| & |\rho_{\phi\theta,\phi\phi}(0)| & |\rho_{\phi\phi,\theta\phi}(0)| & |\rho_{\phi\phi,\phi\phi}(0)| \end{bmatrix} \qquad (6.24a) \\
&= \begin{bmatrix} 1.0000 & 0.3722 & 0.3900 & 0.6036 \\ 0.3722 & 1.0000 & 0.3175 & 0.0808 \\ 0.3900 & 0.3175 & 1.0000 & 0.2987 \\ 0.6036 & 0.0808 & 0.2987 & 1.0000 \end{bmatrix}. \qquad (6.24b)
\end{aligned}
$$

The cross-correlation coefficient is in general a complex number, but the magnitude is presented. The cross-correlation matrix of (6.24b) shows that the signals of different polarizations are correlated. For example, for '$\theta\theta$' and '$\phi\phi$' polarizations (which are often assumed to be orthogonal), the correlation coefficient is about 0.6. This is because the multipath fading signal is not *purely* Rayleigh and in a real situation, in contrast to the ideal situation, each polarization influences other polarizations.

Figures 6.11 and 6.12 show the cross-correlation coefficient between received signals of different polarizations versus spacing between the receiver antennas (no beamforming is performed). Figure 6.11 represents the cross-correlations when the spacing is increased up to six wavelengths. This result can be used to adjust the spacing between the receivers if micro diversity is utilized. From Figure 6.11, it is inferred that for different polarizations, the cross-correlation coefficient is decaying periodically. The maximum $|\rho|$ between different polarization components is always less than 0.6 which is assumed to be uncorrelated for most of the applications (since the power correlation coefficient will be below 0.36). Figure 6.12 illustrates the cross-correlation for larger spacings which can be assisted when macro diversity is used. For the spacing up to 10λ (about three meters for Ottawa ray-tracer), the received signals are " essentially uncorrelated", i.e., $|\rho| < 0.4$.

The cross-correlation is also evaluated for the demeaned, i.e., quasi-Rayleigh or Rayleigh-type, signal. For two different polarizations, e.g., '$\theta\theta$' and '$\theta\phi$', the cross-correlation between

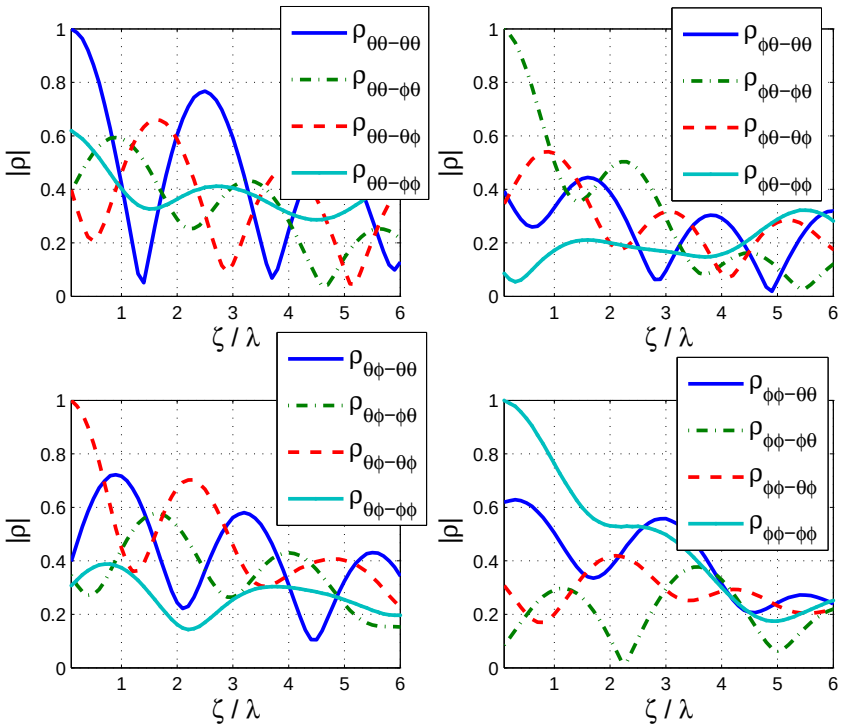

Figure 6.11: Magnitude of the cross-correlation coefficient, the spacing between the receivers is increased up to 6λ (application for micro diversity).

two receivers with spacing $\Delta\zeta$ is written as

$$\rho_{DM\theta\theta,\theta\phi}(\underbrace{m,n}_{\Delta\zeta=m-n}) = \frac{\left\langle b_{0_m}^{\theta\theta} \cdot b_{0_n}^{\theta\phi *} \right\rangle}{\sqrt{\left\langle \left| b_{0_m}^{\theta\theta} \right|^2 \right\rangle \left\langle \left| b_{0_n}^{\theta\phi} \right|^2 \right\rangle}}. \tag{6.25}$$

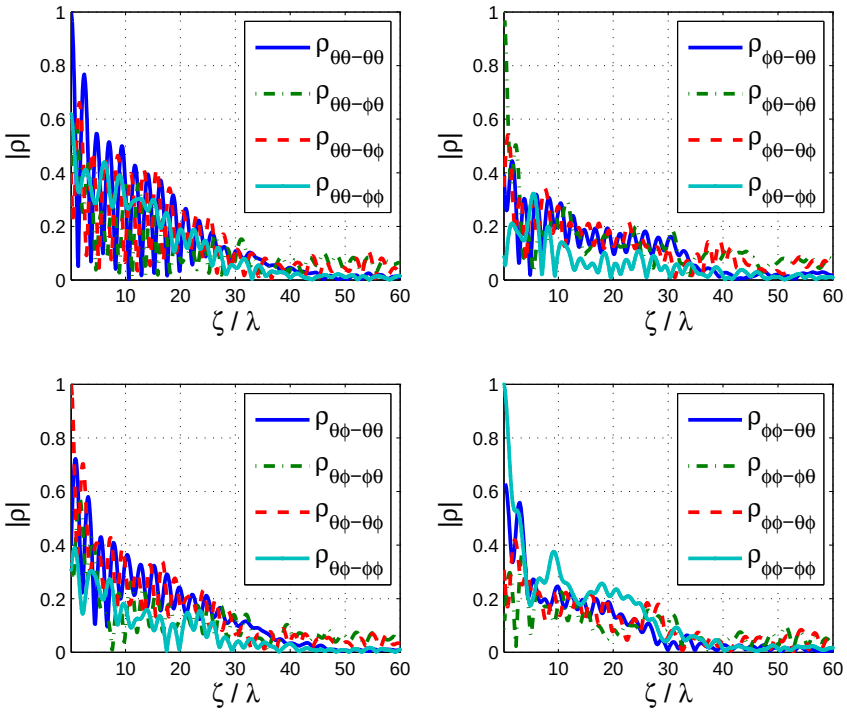

Figure 6.12: Magnitude of the cross-correlation coefficient, the spacing between the receivers is increased up to 60λ (application for macro diversity), $|\rho|$ is negligible ($|\rho| < 0.1$) when the spacing is more than 20λ.

If the integration distance (meaning window) is chosen to be for example 10λ, the cross-correlation matrix for the Ottawa simulation at zero-lag, i.e., $\Delta\zeta = 0$, is as follows,

$$
\begin{aligned}
&|\rho_{DMp}(\Delta\zeta = 0)| \\
&= \begin{bmatrix}
|\rho_{DM\theta\theta,\theta\theta}| & |\rho_{DM\phi\theta,\theta\theta}| & |\rho_{DM\theta\phi,\theta\theta}| & |\rho_{DM\phi\phi,\theta\theta}| \\
|\rho_{DM\theta\theta,\phi\theta}| & |\rho_{DM\phi\theta,\phi\theta}| & |\rho_{DM\theta\phi,\phi\theta}| & |\rho_{DM\phi\phi,\phi\theta}| \\
|\rho_{DM\theta\theta,\theta\phi}| & |\rho_{DM\phi\theta,\theta\phi}| & |\rho_{DM\theta\phi,\theta\phi}| & |\rho_{DM\phi\phi,\theta\phi}| \\
|\rho_{DM\theta\theta,\phi\phi}| & |\rho_{DM\phi\theta,\phi\phi}| & |\rho_{DM\phi\phi,\theta\phi}| & |\rho_{DM\phi\phi,\phi\phi}|
\end{bmatrix} \qquad (6.26a) \\
&= \begin{bmatrix}
1.0000 & 0.0391 & 0.0992 & 0.1800 \\
0.0391 & 1.0000 & 0.0956 & 0.0889 \\
0.0992 & 0.0956 & 1.0000 & 0.0590 \\
0.1800 & 0.0889 & 0.0590 & 1.0000
\end{bmatrix}. \qquad (6.26b)
\end{aligned}
$$

The content of the matrix (6.26b) shows that for the demeaned signal, different polarization channels are *uncorrelated* ($\rho < 0.18$) and these channels can be considered as essentially orthogonal. For the demeaned signal, while the spacing lag is increased the variation of the cross-correlation coefficient follows the Bessel function variation, and the spacing of about 0.2λ seems to guarantee the orthogonality (results are not shown here).

The cross-correlation coefficient matrix for demeaned channel signals is calculated for different integration distances and for both Ottawa and Braunschweig simulations, i.e., from λ to 80λ, and the cross-correlation matrix is reasonably stable to the choice of integration distance. The demeaning of the signal seems to guarantee the orthogonality of the correlations between different polarizations and that is what is expected from the Rayleigh signal.

6.5 Summary

With channel simulation, the ray-tracing computation detail is inherent, and the challenge is to find the appropriately filtered version (meaning that the claimed results should correspond to the measurement results). The filtering includes the bandpass action of the transmit and receive filters, the antennas, the dispersion of the scattering environment, and finally the averaging for estimating the statistical expectation. A complication is that a sampling rate must be nominated for the interpolation between the impulses and care must be taken with the associated processing. There is no widely standardized definition to calculate (evaluate) channel parameters such as local mean, power delay profile (PDP) and its moment, the delay spread, angular spread and channel correlation from physics-based channel data.

Chapter 7

MEA Performance Evaluation

7.1 Introduction and Motivation

The evaluation of MEA performance in urban environments is particularly important for the planning and design of reliable, spectrally efficient systems. To date, MIMO communication using large dimensions has not been implemented for commercial systems. But the potential capacity of MIMO is much more significant when the MIMO dimensions become large. The hold-up is not just the shortfall in understanding how to deploy large-dimension MIMO, but also how to design the antenna systems. There is no widely agreed method for evaluating MEAs used by MIMO communications. Even the performance evaluation of a well-established MIMO configuration, such as the small scale systems already used, remains limited. The evaluation often defers to OTA tests in artificial environmental conditions. The real-world performance remains unclear, so care must be taken in design optimization. The incorporation of some physical modeling of the propagation environment is discussed in order to evaluate the MEA performance for a typical urban wireless channel.

A ray-optic method is applicable to any 3D environment, and any number of antennas with arbitrary patterns. In this sense it offers a practical approach for large-dimension MIMO evaluation by being able to change the antennas and the environment, all in software. The evaluation method is illustrated by using an MEA slot cube (12 antennas) operating in a specific environment, namely downtown Ottawa.

7.2 Received Signal at Mobile Antenna

For a general analysis of the channel, usually the channel relates to the fields only and is represented independent of the antenna type. Alternatively stated, an idealized isotropic antenna pattern is considered. But the transmitting and receiving antennas should be considered separately to be able to fully characterize the channel [20].

The transmitting and receiving antennas, with complex normalized patterns $\mathbf{h}_T(\theta, \phi)$ and $\mathbf{h}_R(\theta, \phi)$, respectively, can be written in two polarizations as

$$\mathbf{h}_T(\underbrace{\theta, \phi}_{\Omega}) = h_{T\theta}(\Omega)\hat{\theta} + h_{T\phi}(\Omega)\hat{\phi}, \tag{7.1a}$$

$$\mathbf{h}_R(\underbrace{\theta, \phi}_{\Omega}) = h_{R\theta}(\Omega)\hat{\theta} + h_{R\phi}(\Omega)\hat{\phi}, \tag{7.1b}$$

where $h_\theta(\Omega)$ and $h_\phi(\Omega)$ denote the antenna patterns in spherical coordinates corresponding $\hat{\theta}$ and $\hat{\phi}$, i.e., the spherical unit vectors in θ and ϕ directions, respectively. The subscripts T and R refer to transmitting and receiving antennas, respectively.

$\mathbf{h}_T$ and $\mathbf{h}_R$ are also written in vector form in $\mathbb{C}^{1\times 2}$ as

$$\mathbf{h}_T(\Omega) = [h_{T\theta}(\Omega) \quad h_{T\phi}(\Omega)] \cdot [\hat{\theta} \quad \hat{\phi}]^{\mathrm{T}}, \tag{7.2a}$$

$$\mathbf{h}_R(\Omega) = [h_{R\theta}(\Omega) \quad h_{R\phi}(\Omega)] \cdot [\hat{\theta} \quad \hat{\phi}]^{\mathrm{T}}, \tag{7.2b}$$

where the superscript 'T' stands for the transpose of the vector and matrix. The sum of incident rays at the ith receiver point, E_i^{inc}, e.g., for a single polarization '$\theta\theta$' (*cf.,* vertically polarized transmit and receive antennas), is represented by

$$E_i^{inc\theta\theta}(\tau, \Omega) = \oint \; g_{r_i}^{\theta\theta}(\Omega, \tau)\; h_{T\theta}(\Omega_D)\; d\Omega_D. \tag{7.3}$$

At the receiver, the components from all directions are weighted by the complex receive antenna pattern to form the received signal (which is also in a summed-ray form),

$$y_{r_i}^{\theta\theta}(\tau) = \oint \; E_i^{inc\theta\theta}(\Omega, \tau)\; h_{R\theta}(\Omega_A)\; d\Omega_A. \tag{7.4}$$

Including the polarizations, the signal voltages are calculated as

$$\mathbf{y}_{r_i}(\tau) = \oint \oint \; \mathbf{h}_R(\Omega_A) \cdot \mathbf{g}_{r_i}(\Omega, \tau) \cdot \mathbf{h}_T^{\mathrm{T}}(\Omega_D)\; d\Omega_A\; d\Omega_D. \tag{7.5}$$

For each receiving point, e.g., the ith point, there are J_i rays calculated by the ray-tracer, i.e., only J_i departure and arrival solid angles (Ω_A and Ω_D) for the ith receiver are

sampled. The arrival and departure angles, ϕ_A, θ_A, ϕ_D and θ_D, are seldom in the same direction of the sampled angles of the antenna pattern. Therefore, interpolation is required before proceeding with signal calculation, i.e., (7.3), (7.4) and (7.9). The ramification is that care must be taken with the angular sample spacing and interpolation because these directly affect the signal.

7.3 Metrics for Multiport Directional Coverage

For an N port antenna, the normalized (polarized) patterns of the kth port, $k \in [0, ..., N]$, are denoted

$$\mathbf{h}_k(\Omega) = h_{k\theta}(\Omega)\hat{\theta} + h_{k\phi}(\Omega)\hat{\phi}. \tag{7.6}$$

The set of patterns is assembled as

$$\mathbf{H}(\Omega, \tau) = \begin{bmatrix} \mathbf{h}_1(\Omega, \tau) \\ \mathbf{h}_2(\Omega, \tau) \\ \vdots \\ \mathbf{h}_N(\Omega, \tau) \end{bmatrix} \in \mathbb{C}^{N \times 2}, \tag{7.7}$$

and the transmitting and receiving antennas are $\mathbf{H}_T(\Omega)$ and $\mathbf{H}_R(\Omega)$, with $N = N_{Tx}$ for $\mathbf{H}_T(\Omega)$ and $N = N_{Rx}$ for $\mathbf{H}_R(\Omega)$,

$$\mathbf{H}_T(\Omega, \tau) \in \mathbb{C}^{N_{Tx} \times 2} \tag{7.8a}$$

$$\mathbf{H}_R(\Omega, \tau) \in \mathbb{C}^{N_{Rx} \times 2}. \tag{7.8b}$$

The received signals at the ith receiver point are

$$\mathbf{Y}_{r_i N_{Rx} \times N_{Tx}}(\tau) = \oint \oint \mathbf{H}_R(\Omega_A) \cdot \mathbf{g}_{r_i}(\Omega, \tau) \cdot \mathbf{H}_T^{Tr}(\Omega_D) d\Omega_A d\Omega_D. \tag{7.9}$$

The following two cases are of interest:

- open circuit patterns, i.e., there is no mutual coupling (which can be used for selection combining and switched combining),
- loaded circuit patterns (embedded patterns or active patterns), i.e., the mutual coupling between antennas is included (for equal gain combining, maximum ratio combining, and optimum combining).

7.4 Diversity Analysis

The analysis of antenna diversity is usually related to the signal envelope. The power level of the channel fading which is caused by the varying multipath, brings about the link *outage* as a performance parameter, e.g., [14]. The outage probability is derived from the cumulative distribution function (CDF) of the power of the wireless link. The digital outage is defined as the relative time or relative number of terminals (at a given time) in a multiuser system for which the error performance or capacity efficiency drops below some acceptable level, whereas the analogue outage pertains to the SNR or SINR [91].

7.4.1 Diversity Combining

For some combining techniques, such as maximum ratio combining (MRC), a noise level is required in order to weight each branch by its SNR.

The baseband equivalent signal voltage and the baseband noise powers at the kth antenna branch (out of the total $M_{ant} = N_{Rx} \times N_{Tx}$ branches) are denoted by y_k and n_k, respectively. The noise power is often taken as constant and common for all the branches, i.e., $N_0 = N_k = \langle |\bar{n}_k|^2 \rangle$.

The amplitude SNR for the kth branch is denoted $q_k = \frac{|y_k|}{\sqrt{\langle |\bar{n}_k|^2 \rangle}}$. The energy ratio is $SNR_k = \gamma_k = q_k^2$ and its mean is $\Gamma_k = \langle \gamma_k \rangle$. The three classical combining techniques (if the noise energies are the same for all branches) are

- A. Selection Combining (SC): $q_C = \max\{q_1, q_2, \ldots, q_{M_{ant}}\}$,
- B. Equal Gain Combining (EGC): $q_C = \sum_k q_k / \sqrt{M_{ant}}$,
- C. Maximum Ratio Combining (MRC): $q_C = \sqrt{\sum_k q_k^2}$,

where q_C is the envelope of the combined signal.

In the example below, a hybrid combination is used. The combination consists of two stages. The branches are first ordered and selected based on the highest local mean signal strength (similar to selection combining (A)). These branch signals are then combined using two techniques: predetection equal gain combining (B) and maximum ratio combining (C). This combination is a practical technique for currently available electronics, allowing inexpensive coherent combining yet also allowing the benefit of selecting the best average

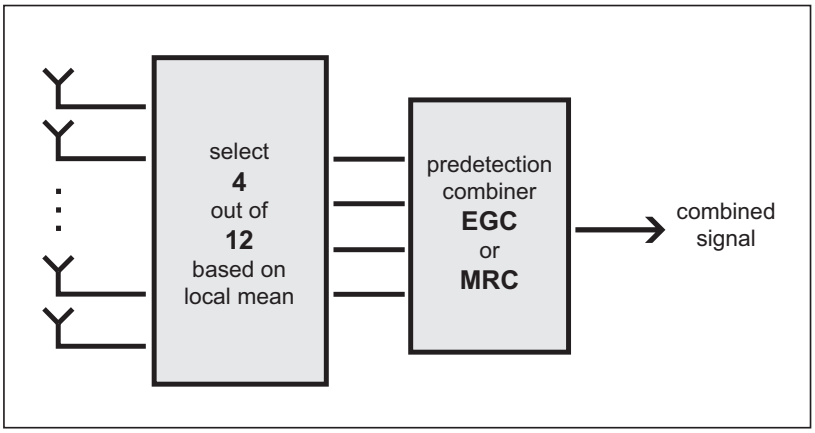

Figure 7.1: The block diagram of the hybrid combiner. The M_{ant} branches are the input of the combiner. In the first stage, the branches are sorted based on their local mean power, and then M_{comb} branches, i.e., here four branches, are chosen and fed to the next stage which can be an MRC or EGC. The output of the hybrid combiner is the amplitude SNR (i.e., $\sqrt{SNR}$) of the combined signal, i.e., q_C.

gains from the twelve branches. Figure 7.1 illustrates the block diagram of such a hybrid combiner. In this example, first, all diversity antenna branches are sorted based on their local mean power and the first best four branches are chosen. These four branches are then fed to the diversity combiner, i.e., MRC or EGC, and the output of the hybrid combiner is the amplitude SNR (i.e., $\sqrt{SNR}$) of the combined signal, i.e., q_C.

For the predetection combining, the complex weights are derived from samples of the signal-plus-noise, not from the wanted signal alone which may not be available in practice. Combining using the signal-plus-noise (as a weighting) is not suitable for low SNRs. But for branch SNRs above about 10dB, there is no significant difference between this form of combining and classical combining (weights derived from the wanted signal alone), e.g., [154]. Other idealized and practical combining techniques can be readily tested and analyzed, including more sophisticated MIMO combinations.

7.4.2 Diversity Gain

Diversity gain is an analogue metric that is considered to measure the performance of the diversity of a system. For a given outage probability, the diversity gain is defined as the increase in the SNR of the combined antenna signal relative to a reference SNR, e.g., [91, 155]. In an ideal situation, the diversity branches have equal average SNR and

zero mutual coupling. However, for compact antennas, the coupling is seldom zero and the average SNRs are seldom the same. The idealized situation allows useful performance benchmarks.

At a given probability, e.g., $p\%$, the diversity gain, DG, for the combined M_{ant}-branch signal, can be defined as (*cf.*, the discussion in [13])

$$\mathrm{DG}_{DIV}(dB) = \left(\frac{\gamma_C}{\Gamma_C}(dB) - \frac{\gamma_{ref}}{\Gamma_{ref}}(dB)\right)_{p\%} \tag{7.10}$$

where γ_C is the SNR of the combined signal and Γ_C is its mean. γ_{ref} and Γ_{ref} are, respectively, the instantaneous and mean SNR of a reference, for example that of a single element reference antenna. Often, the branch with maximum mean SNR or the mean SNR of all branches, or a separate reference element such as a dipole, is considered as the reference SNR. Choosing a poor reference branch for γ_{ref} will artificially increase the DG. Another definition takes a common mean SNR reference in each term of (7.10), i.e.,

$$\mathrm{DG}_{DIV}(dB) = \left(\gamma_C(dB) - \gamma_{ref}(dB)\right)_{p\%}, \tag{7.11}$$

where the normalization is with respect to the mean of the reference SNR, i.e., Γ_{ref}. Note the definition used here is in accordance with (7.11). The diversity gain are calculated (from above equations) by interpolation between dense samples, e.g., [14, 155]. Here, the linear interpolation is considered for calculating the diversity gain of the channel.

A trajectory of the mobile terminal is taken for evaluating the diversity performance. The averaging is performed over the trajectory.

7.5 Dipole Antennas for Diversity Evaluation

Along the trajectory, two dipole antennas are placed at distance $d = l_{mn}$ to each other. Figure 7.2 shows the configuration of the multi-element, i.e., two-element, antenna system. l_{mn} indicates the distance between two antennas located at mth and nth points of the trajectory. The received signal at both antennas are combined using different diversity techniques. Selection combining, equal gain combining and maximum ratio combining are considered here.

Figure 7.3 shows the combined received signal for $l_{mn} = \lambda$ (here, $\lambda = 30$cm, which is a realistic assumption for mobile stations like laptop boards, etc.). The comparison between selection combining (SC), equal gain combining (EGC) and maximum ratio combining

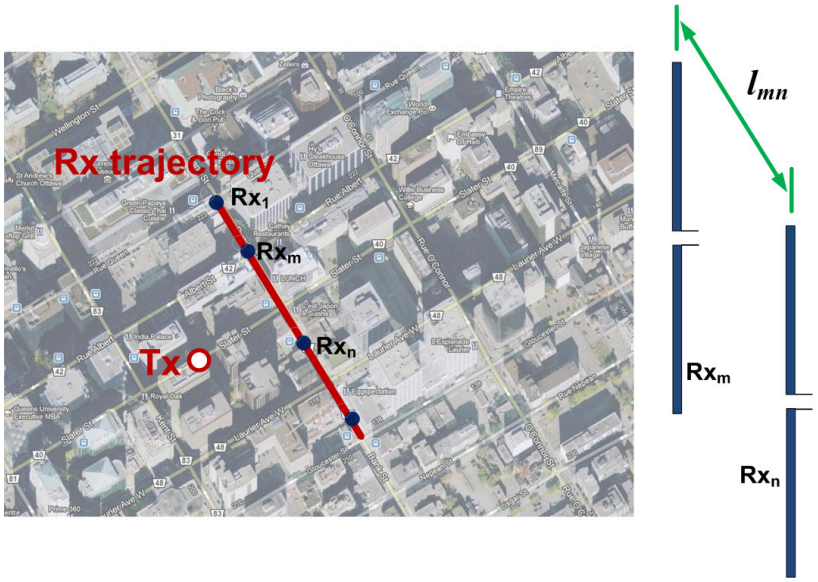

Figure 7.2: The configuration of the two-element (1×2) receive diversity system.

(MRC) shows more diversity improvement with MRC (as expected). Figure 7.4 shows the received signal for different antenna spacings, ranging from a fraction of wavelength to some hundreds of wavelengths. This figure is presented to provide some feel for the diversity gain which could be provided with only two dipoles.

7.5.1 Diversity Results for 1×2 Dipoles

Antenna selection/combining might be performed either based on the instantaneous signal level, demeaned signal level, i.e., fast fading, local mean signal, i.e., slow fading [156]. Table 7.3 shows the received diversity gain, for two different cases of instantaneous signal,(i.e., Figure 1.3) and demeaned (Rayleigh-type, fast fading). For the demeaned signal, the integration distance in set to be 10λ. The diversity gains have been calculated for different probabilities, i.e., 10%, 5% and 1% from (7.10).

Figure 7.5 shows the variation of the diversity gain for different probabilities, i.e., 10%, 5% and 1%, while the spacing between two antennas are increasing. As expected, the diversity gain improvement is tremendously high when the antennas are far apart, e.g., $l_{mn} = 100\lambda$. This can be implemented for macro diversity applications.

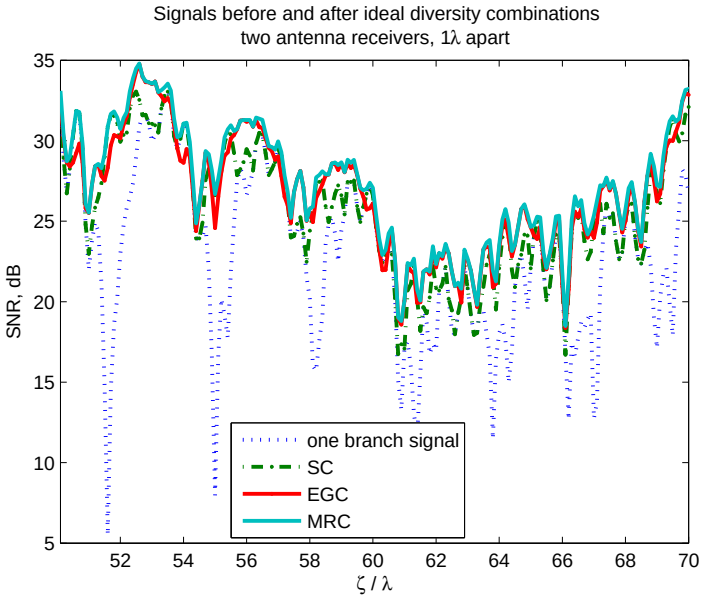

Figure 7.3: Combined signals and the single-branch signal for the receivers being λ apart along the trajectory (a few wavelengths are shown as a sample section of the trajectory).

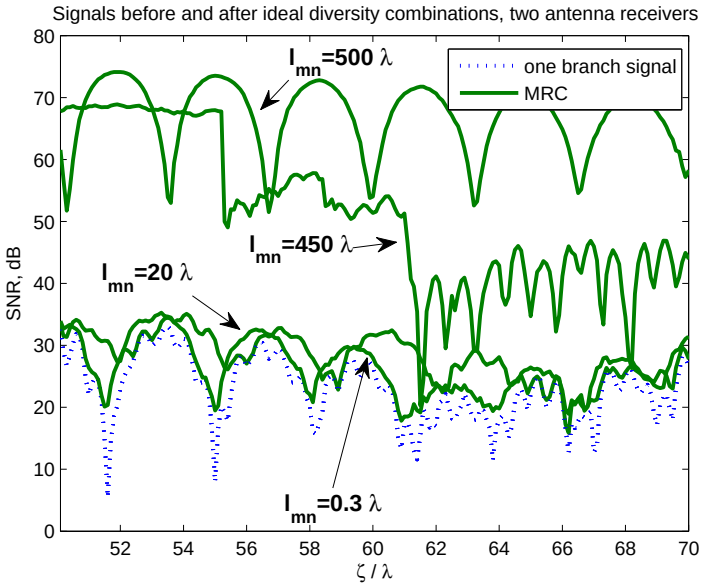

Figure 7.4: Combined signals and the single-branch signal received signal for different spacing between antennas along the trajectory (a few wavelengths are shown as a sample section of the trajectory).

signal type	10% DG	5% DG	1% DG
instantaneous	6.36dB	8.78dB	15.78dB
fast fading	6.61dB	8.26dB	13.40dB

Table 7.1: 10% and 1% diversity gain for instantaneous and fast fading signals for MRC. $l_{mn} = 10\lambda$, local mean over moving window with $L = 10\lambda$ integration distance.

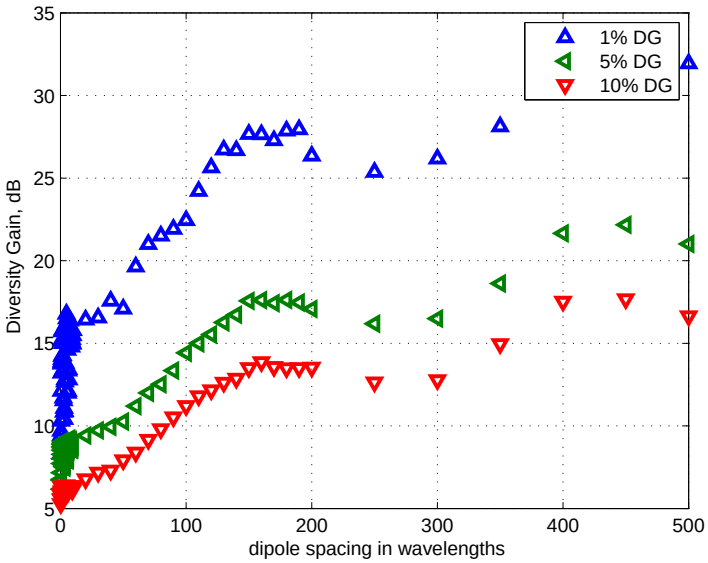

Figure 7.5: Diversity gain (big picture) for different outage probabilities, i.e., 10%, 5% and 1%, versus the spacing between two dipole in wavelength. The large spacings may be considered for macro diversity.

7.6 MEA Antenna Dievrsity

7.6.1 MEA Antenna Patterns

Polyhedron structured MEAs are suitable candidates for multiport antennas in uniform 3D scenarios, *cf.*, [157–161]. The antennas may be mounted on each surface of the polyhedron or be set along the edges.

The MIMO cube is a type of polyhedron that has been studied in the configurations of dipole cube and slot cube over the past decade, e.g., [157, 158].

An example is the slot MIMO cube, where slots are set on the edges of the hollow polyhedron (hollow cube), shown in Figure 7.6. This MEA has been designed, simulated,

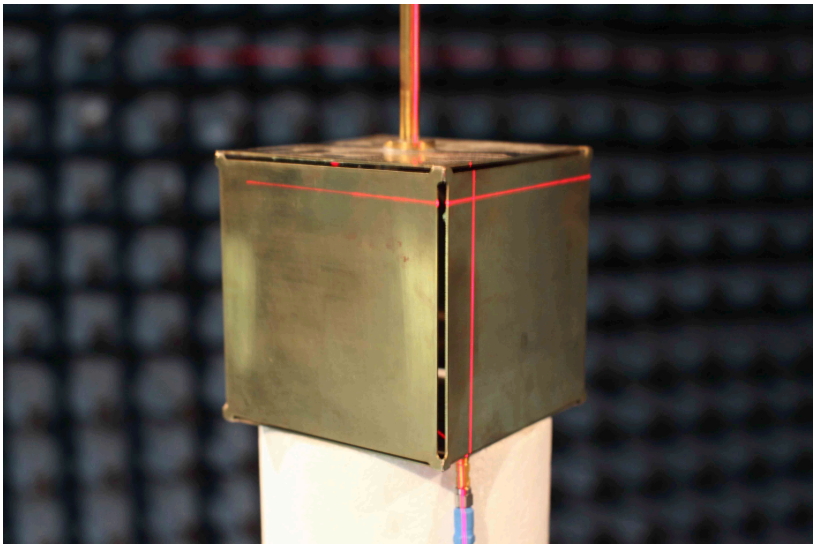

Figure 7.6: The MIMO slot cube with broad bandwidth [159] used for illustrating diversity evaluation in an urban channel.

built and measured [159]. This multiport antenna has a 30% bandwidth at $S_{11} \leq 10$dB when terminated with 50 Ohms.

The multiport antenna of Figure 7.6 has been illuminated with a plane wave of arbitrary polarization, and the voltages of both cases of open circuit and loaded circuit are available from simulation and measurement, and the simulation and measurement agree well [162]. The pattern evaluation has been undertaken and used in [8, 13, 162].

The branches are correlated and their average SNRs are unequal. So this compact antenna can be a typical MEA candidate for implementation (which is seldom treated in communications system studies). This antenna is analyzed for diversity performance below.

The set of directions to be sampled are uniform over the sphere. This is non-trivial, so a set of uniformly spaced samples in both angles, i.e., (θ, ϕ), or else over $(\sin\theta, \phi)$, can be used. Here, the antenna patterns have been uniformly sampled over the sphere, and the resolution is taken to be one degree for both azimuth and zenith angles.

7.6.2 Instantaneous Signal SNR

The multiport antenna of section 7.6.1 has been used for transmit diversity, i.e., '12×1' (the cube antenna is at the fixed base station position), and receive diversity, i.e., '1×12', (the cube is moving along the trajectory).

Figure 7.7 shows the improvement in SNR for a small sample part of the trajectory (a few wavelengths) for the receive diversity case. It should be noted here that the combinings, i.e., SC, EGC and MRC, are performed based on the whole trajectory. The 5% probability improvement is also based on the whole trajectory. The isotropic pattern (solid purple line) is from the ray-tracing data and corresponds to an idealized, isotropic, dual-polarized, antenna at both the transmitter and receiver. Here it is denoted as "summed-field" to emphasize that this SNR corresponds to the pattern of an isotropic antenna, addition of unweighted complex rays. The signal from one of the strongest branches of the MEA is also shown for the reference (solid cyan line). The three diversity combining techniques have been applied to all twelve branches of the MEA. The dB difference between the 5% outage levels of the two signals is the diversity gain. In this example the diversity gain is about 18.5dB. The maximum ratio combining technique outperforms the other techniques as expected.

Figure 7.8 shows the cumulative distribution versus normalized SNR. The solid blue line indicates the case where the MEA is at the receiver, i.e., mobile antenna, and the dashed green line refers to the case where the MEA is used at the base station. The maximum ratio combining of only two branches (best SNRs) at outage probability 1% provides more than 10dB diversity gain improvement in receive diversity, and more than 5dB diversitygain improvement in transmit diversity. This result confirms that a simple two-branch antenna can provide large gain improvement if they are used efficiently, e.g., [163]. The 12-branch combined signals for selection and maximum ratio combining are included in the figure. The receive diversity outperforms the transmit diversity, and that is because the angular spread at the receiver is larger that the angular spread in the transmitter.

The diversity gain, from (7.10), is in Figure 7.9 for transmit (diamond line) and receive (squared line) diversities, for different outage probabilities. The reference Rayleigh curve is for ideal branches (same mean SNR, and uncorrelated Rayleigh channel signals).

The diminishing return in diversity gain from more branches is worse for the MEA antenna than for the reference case (red lines with circle markers in Figure 7.9). This is because at the base station, several of the elements do not illuminate the directions of interest, i.e., their distributed directivity is low and their contribution to the diversity combined signal is not noticeable. Increasing the number of elements to more that 8 (and especially 10) does not significantly affect the diversity gain, as expected.

The receive diversity gain is slightly larger than transmit diversity gain for the same

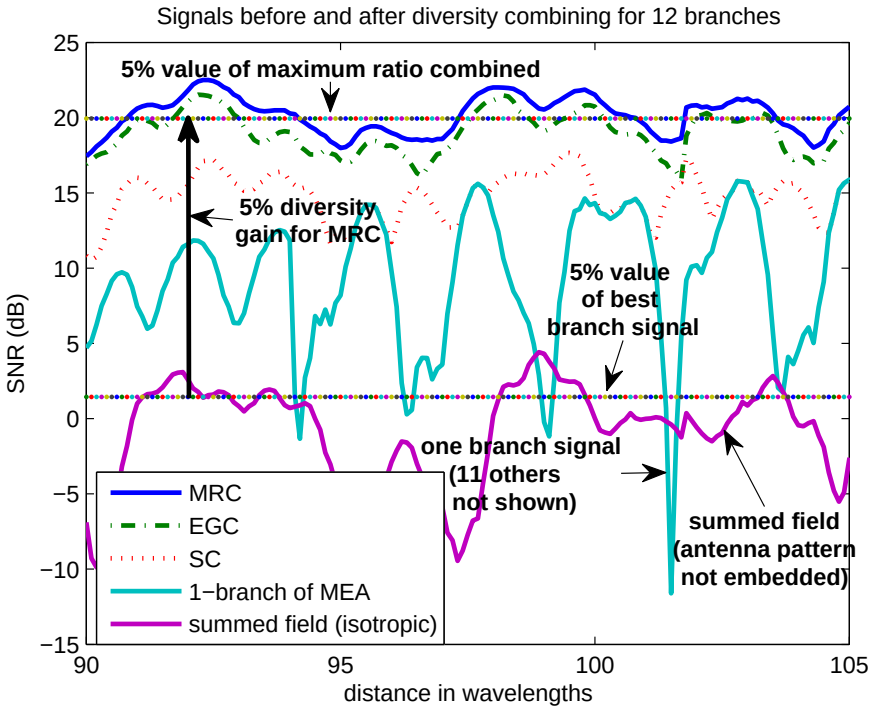

Figure 7.7: The received SNR for receive diversity from different diversity techniques along a few wavelengths of the trajectory. The signal of one branch of the MEA is included for comparison. The dB difference between the 5% outage levels of two signals is the diversity gain.

number of branches. Again, this is because of the angular spread at the transmitter and receiver. The use of the cube antenna is less efficient at the base station in the sense that several branches are not well utilized due to the angular directivity. This is not an optimized choice of antenna for the base station, but this antenna is used here for illustration.

7.6.3 Slow-Faded and Rayleigh-Faded Signal SNRs

The receiver takes the local mean of the signal power and then the process of selection/combining is applied. This is called slow selection/combining.

The CDF for the local mean and demeaned signals have been calculated and compared with the result from instantaneous, i.e., section 7.6.2. The integration distance is 10λ. Tables 7.2 and 7.3 summarize the received diversity gain, for three different cases of instantaneous, fast (demeaned) and slow (local mean) fading signals. Table 7.2 contains the results for just

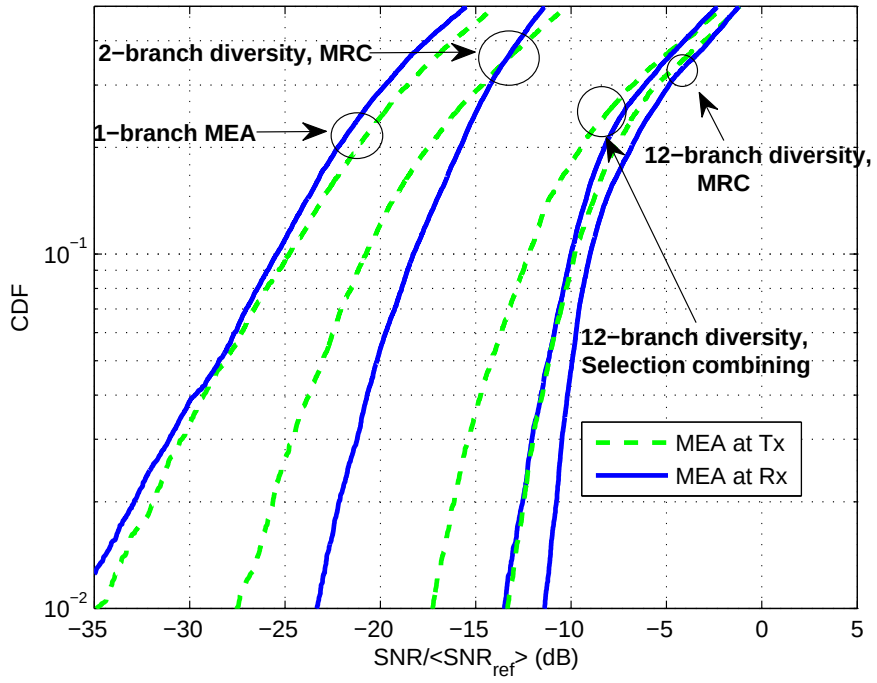

Figure 7.8: The probability that the SNR is less than abscissa, i.e., CDF, versus normalized SNR. The solid line indicates the case where the MEA is the receiver, i.e., mobile antenna, and the solid line refers to the case where the MEA is used at the base station. 1-branch MEA curve corresponds to the case when only one branch of the MEA is used, i.e., the 1-branch MEA is selection based on the beast local mean of all 12 antennas which is the first stage of the hybrid combining. 2-branch MEA is combined based an the hybrid combining techniques.

two receiver antennas of the MEA (the best two mean SNRs), whereas table 7.3 contains the results when all the twelve antennas of the MEA are used. In both tables, the diversity gains for uncorrelated, equal energy, Rayleigh fading signal (i.e., Figure 7.9), are also included for comparison. The diversity gains from fast fading and reference Rayleigh fading signals are quite similar, which is expected. Since the fast fading signal is the demeaned quasi-Rayleigh signal.

The integration distance in set to be 10λ. Increasing the integration distance to 40λ does not affect the results significantly.

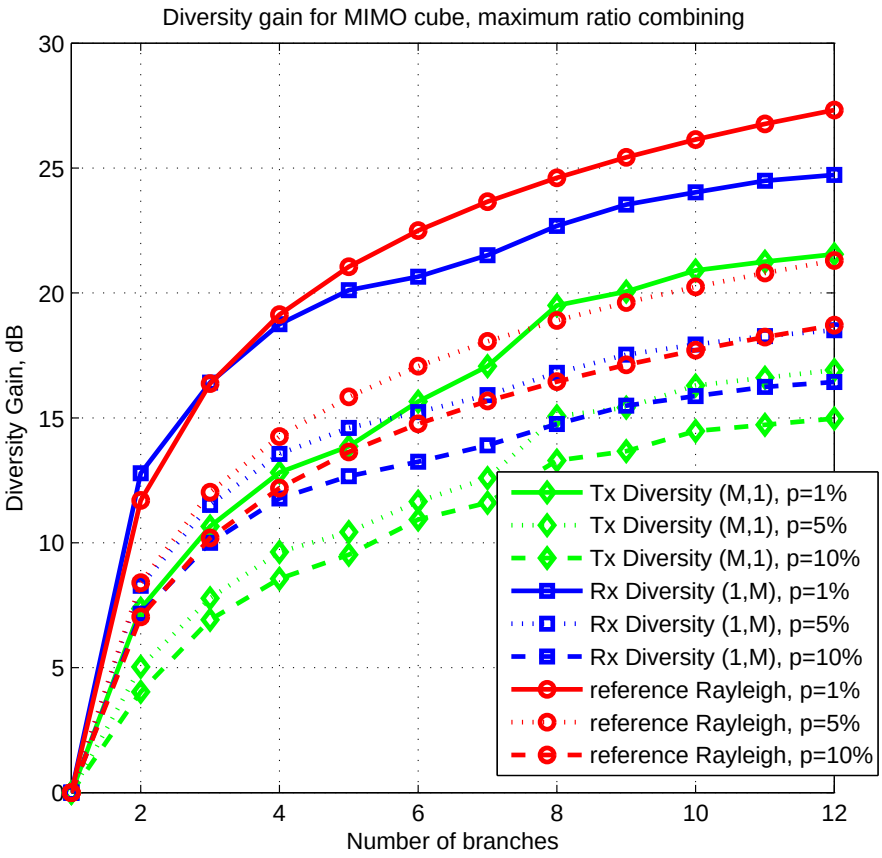

Figure 7.9: Diversity gain for two different cases of 'transmit diversity' and 'receive diversity', versus increasing number of branches of the MEA. The branch with the highest mean SNR is taken as the reference.

If just two receive antennas are used, for 10% percent of the samples, there is no difference between the receive diversity gain acheived for three difference cases cases. Instantaneous, fast and slow fading based antenna diversity show 5.22dB and 6.63dB and 5.3dB average power gains, respectively. By increasing the number of the antennas, the diversity gains from instantaneous and fast fading signals remain the same and that of fast fading signals surpasses them.

If this procedure is implemented in real experimental scenario, the 'meaning' (averaging) process produces an (intrinsic) averaging delay which might result in negative gain in dB

signal type	10% DG	5% DG	1% DG
instantaneous	5.22dB	6.72dB	12.79dB
slow fading	5.30dB	5.24dB	5.75dB
fast fading	6.63dB	8.04dB	13.09dB
Rayleigh reference	7.03dB	8.41dB	11.70dB

Table 7.2: 10%, 5% and 1% diversity gains of two-branch antenna (only two branches of the MIMO cube with the highest mean SNR are considered) for instantaneous, slow and fast fading for MRC. $L = 10\lambda$, the integration distance to calculate the local mean and demeaned signals is 10λ.

signal type	10% DG	5% DG	1% DG
instantaneous	14.01dB	16.11dB	24.73dB
slow fading	12.63dB	13.24dB	14.07dB
fast fading	17.23dB	19.73dB	27.35dB
Rayleigh reference	18.71dB	21.30dB	27.33dB

Table 7.3: 10%, 5% and 1% diversity gains of tweleve-branch MIMO cube, for instantaneous, slow and fast fading for MRC. $L = 10\lambda$, the integration distance to calculate the local mean and demeaned signals is 10λ.

[156]. The advantages of this slow selection/combining are the improvement in throughput, decrease of the interference and increase of the mobile battery life [156].

7.7 Summary

The spectral efficiency of wireless systems is partially governed by the radiowave propagation, specifically the multipath. Typically, equalization is used to repair the channel distortions, but the ideal solution is to use multi-element antennas (MEA), which involves the MIMO technology and diversity combining techniques. The evaluation of the performance of multi-element antennas is of great importance for the planning and design of reliable and spectrally efficient systems. Nevertheless, large-scale MEAs have not extensively been applied (implemented) due to the complexity of their design and performance evaluation.

There are few ways to scientifically compare different multiport antenna designs. It is contended that a suitable way forward for the antenna electrical evaluation (in order to help guide the design), is to use physical modeling of the environment together with parametric antenna data. This comprises ray-tracing with embedded multiport antenna patterns,

akin to the double-directional channel. It offers excellent trade-offs for the modeling of the channel, but there remain several pitfalls in the estimation of the signals from the ray data. Furthermore, there is no standard for ray-tracing in the sense of a widely accepted criterion for choosing the number of rays, reflections, diffractions, and rough surface scattering components, etc.

Antenna patterns can be entered from physical measurements, numerical calculation, or mathematical modeling functions. For indoor situations, architectural CAD files can be used for modeling the environment. For outdoor, The use of GIS data for the environment model allows the neighborhoods and streets of many cities to be modeled, so different antenna systems can be compared for modeled specific environments.

To date, MIMO communications using large dimensions have not been implemented for commercial systems. But the potential capacity of MIMO is much more significant when the MIMO dimensions become large. The hold-up is not just the shortfall in understanding how to deploy large-dimension MIMO, but also how to design the antenna systems.

This method maintains the flexibility of being computer-driven with full control of the modeling parameters, while still allowing the choice of incorporating physically measured channel information. In principle, this method is applicable to any 3D environment, and any number of antennas with arbitrary patterns. In this sense it offers a practical approach for large-dimension MIMO evaluation by being able to change the antennas and the environment, all in software.

The current limitation is that the computation (mainly the ray-tracing aspect - setting up a 3D model and deriving the relevant rays) requires automation and standardization, and of course great computing power. However, these seem to be achievable goals.

Specific digital communication aspects (not addressed here) are possible by applying the resulting channels to standard simulation approaches. However, it is clear that the antenna adaptation - with the associated changing patterns - and the (adaptive) digital communications are closely interrelated, and their integration is not trivial.

Chapter 8

Summary, Conclusion and Future Works

8.1 Summary and Conclusion

Increasing the bandwidth of elements and the use of MEAs are two of the solutions for the problem of exploiting the available bandwidth more efficiently.

To evaluate the theoretical bandwidth of the antenna, its impedance should be available. The impedance of the electric dipole, the simplest antenna element, is not well established despite its long history of research. One of the problems in treating the impedance is the modeling of its excitation feed. Different electromagnetic numerical methods pursue different models of the feed gap. In chapter 2 the dipole impedance was investigated. The dipole is studied as a stand-alone element, i.e., the feed modeling as an explicit problem is not considered. The most significant research on dipole impedance, with and without excitation gap is summarized. Then some of the most popular numerical methods have been introduced and the results for impedance have been illustrated. The theoretical methods, i.e., induced EMF and wave structure methods, are applied for the dipole impedance without gap and the induced EMF method is developed for the impedance of a dipole with gap. This is a novel theoretical approach in treating the impedance of a dipole with gap.

The quality factor and bandwidth of the dipole is considered as a separate topic. The Q results from different theoretical and numerical methods as well as some published measurement results are provided in chapter 3. Some of the conventional Q bounds as well as

the recent Q bound are presented as a Chu graph. The results indicate that the induced EMF method and FDTD method give the lowest quality factor, i.e., highest theoretical bandwidth, among all the available methods.

Chapter 3 also discusses the ohmic loss of a half-wavelength dipole and its radiation efficiency for some of the best conductors. Ohmic loss is a restricting factor at emerging frequencies. These new results demonstrate that at high frequencies, i.e., more that 60GHz, the ohmic loss becomes significant (compared to the radiation resistance) and the thickness of the dipole becomes a design limitation. These are new and useful results.

Studying antenna arrays and diversity correlation theory are the only guidelines for MEA design. The correlation coefficient between the patterns of an array can be regarded as an indication of coupling between the elements of and MEA. Chapter 4 looks at the antenna arrays and depicts some of the limitations in their implementation. The basic array structures are analyzed and new and non-intuitive results for using a simple beamformer are presented. Adding more antenna elements does not help unless the more degrees of freedom are considered in design methodology.

Physics-based simulation channels provide data that cannot be physically measured. The main features of this method of channel evaluation are introduced in chapter 5. The simulation has been undertaken by two different research centres and the ray-tracing data files are provided. The Communications Research Centre, Canada has simulated an urban channel in Downtown Ottawa, and the Braunschweig Technische Universität has simulated a suburban channel in City centre of Braunschweig. Each simulator uses its own criterion, i.e., number of reflections and diffractions, power threshold, etc. Chapter 6 interprets these data files and develops the proper calculation procedure for the first time for selected channel parameters. So far, there is not any standard approach to determine the channel parameters for a physically-modeled channel. Here the channel parameters have been formulated to suit for a physically-modeled channel.

Deploying MEAs, i.e., MIMO and other diversity techniques, is the key to high spectral efficiency. To date, MIMO communication using large dimensions has not been implemented for commercial systems. There is no widely agreed method for evaluating MEAs used for MIMO communications. Even the performance evaluation of a well-established MIMO configuration, such as the small scale systems already used, remains very limited. The evaluation often defers to OTA (over-the-air) tests of some form of coarse throughput in artificial environmental conditions, and the real-world performance of the system, and the

antennas, remains unclear. Chapter 7 develops the incorporation of some physical modeling, *viz.*, ray-tracing, of the propagation environment to evaluate the MEA performance for urban wireless channels. The limitation is computation capability.

8.2 Recommendation for Future Works

8.2.1 Measurement of the Thin Dipole Impedance

The theoretical results from induced EMF method and the numerical results from FDTD method offer a very high 3dB impedance bandwidth for an impractically thin dipole, i.e., $a < 10^3\lambda$, with large gap size, i.e., $\delta_g = 10^{-1}\lambda$. It is a challenging research task to get measurements results for this dimension of dipole. It is emphasized that in an antenna theoretic approach, the impedance of an antenna should be considered as one problem, and its feed and matching network should be considered separately.

8.2.2 Validity of the Physics-Based Simulation

The physics-based channel data are from two different research centres, CRC Canada, and BTU Germany. The results for channel parameter and MEA evaluations would be more complete if the CRC simulator could simulate the Braunschweig trajectory, and the BTU simulator could simulate the Ottawa channel. In that case, two data sets are provided for each channel, and then two sets of results will be available. Also, attempting the measurement of the channels is very important, and the measured data needs to be added to the simulation sets. In that case, the fair comparison of the outcomes from ray-tracing techniques is possible.

8.2.3 Applications of the Physics-Based Results

Many other applications can be suggested for the physics-based results derived in this thesis. For example, these results can be used to study the performance metrics in digital communications, e.g., bit error rate (BER). MATLAB has recently amended a package that includes channel models for the signal processing of digital communications. These models and channel parameters, are statistically generated and do not feature the unique aspects of a real channel. Adding the ray-traced channel results to the mathematical computation tools such as MATLAB or MAPLE, provides more realistic digital communication results.

Several Rice (K) factor estimators have been suggested, e.g., [164]. All of these estimators are designed based on ideal Rayleigh channel. The physics-based simulated channel is can be used for verifying these estimators.

Bibliography

[1] R. G. Vaughan, "Compact multiport antennas for high spectral efficiency," in *Antennas and Propagation (EuCAP), 2013 7th European Conference on*, 2013, pp. 16–20.

[2] G. F. Pedersen, "Limit values for downlink mobile telephony in Denmark," Aalborg university, Tech. Rep., November 2012.

[3] M. Dehghani Estarki and R. G. Vaughan, "Theoretical zero-gap dipole impedance," in *2012 IEEE International Symposium on Antennas and Propagation (APSURSI)*, Chicago, IL, USA, July 2012.

[4] M. Dehghani Estarki, X. Yun, X. Han, and R. G. Vaughan, "The effect of gap size on dipole impedance using the induced emf method," in *20th International Symposium in Electromagnetic Theory (EMTS), URSI.* Berlin, Germany: IEEE, August 2010, pp. 373–376.

[5] L. J. Chu, "Physical limitations of omnidirectional antennas," *Journal of Applied Physics*, vol. 19, no. 2, pp. 1163–1175, December 1948.

[6] M. Gustafsson, C. Sohl, and G. Kristensson, "Illustrations of new physical bounds on linearly polarized antennas," *IEEE Transactions on Antennas and Propagation*, vol. 57, no. 5, pp. 1319–1327, May 2009.

[7] M. Dehghani Estarki and R. G. Vaughan, "Bounds on Q for the short dipole," in *2012 IEEE International Symposium on Antennas and Propagation (APSURSI)*, Chicago, IL, USA, July 2012.

[8] J. X. Yun and R. G. Vaughan, "Space efficiency of multiple element antennas," *Antennas and Propagation, IEEE Transactions on*, vol. 60, no. 6, pp. 3066–3071, 2012.

[9] M. Dehghani Estarki and R. G. Vaughan, "A study of the radiation efficiency of a half wavelength dipole," in *14th Conference on Antenna Technology and Applied Electromagnetics and the American Electromagnetics Conference (ANTEM-AMEREM).* Ottawa, ON, Canada: IEEE, July 2010, pp. 1–4.

[10] H. A. Wheeler, "Fundamental limitations of small antennas," *Proceedings of the IRE*, vol. 35, no. 12, pp. 1479–1484, December 1947.

[11] R. C. Hansen and R. E. Collin, *Small Antenna Handbook*. Hoboken, NJ, USA: John Wiley & Sons, Inc., 2011.

[12] D. Kajfez, *Q Factor*. Oxford, MS, USA: Vector Fields, 1994.

[13] J. X. Yun and R. G. Vaughan, "Multiple element antenna efficiency and its impact on diversity and capacity," *Antennas and Propagation, IEEE Transactions on*, vol. 60, no. 2, pp. 529–539, 2012.

[14] R. G. Vaughan and J. B. Andersen, *Channels, Propagation and Antennas for Mobile Communications*, 1st ed. London, United Kingdom: Institution of Electrical Engineers, 2003.

[15] J. H. Winters, "On the capacity of radio communication systems with diversity in a rayleigh fading environment," *Selected Areas in Communications, IEEE Journal on*, vol. 5, no. 5, pp. 871–878, 1987.

[16] S. A. Mirtaheri and R. G. Vaughan, "Practicable MIMO capacity in ideal channels," in *Vehicular Technology Conference, 2006. VTC 2006-Spring. IEEE 63rd*, vol. 4. IEEE, 2006, pp. 1620–1624.

[17] Google Maps. [Online]. Available: https://maps.google.com/

[18] Y. L. C. de Jong, "Measurement and Modelling of Radiowave Propagation in Urban Microcells," Ph.D. dissertation, Technische Universiteit Eindhoven, 2001.

[19] F. Aguado Agelet, A. Formella, J. M. Hernando Rabanos, F. Isasi de Vicente, and F. Perez Fontan, "Efficient ray-tracing acceleration techniques for radio propagation modeling," *Vehicular Technology, IEEE Transactions on*, vol. 49, no. 6, pp. 2089–2104, 2000.

[20] M. Steinbauer, A. F. Molisch, and E. Bonek, "The double-directional radio channel," *Antennas and Propagation Magazine, IEEE*, vol. 43, no. 4, pp. 51–63, 2001.

[21] M. C. Jeruchim, P. Balaban, and K. S. Shanmugan, *Simulation of Communication Systems: Modeling, Methodology and Techniques*. Springer, 2000.

[22] P.-S. Kildal and K. Rosengren, "Correlation and capacity of mimo systems and mutual coupling, radiation efficiency, and diversity gain of their antennas: simulations and measurements in a reverberation chamber," *Communications Magazine, IEEE*, vol. 42, no. 12, pp. 104–112, 2004.

[23] D. A. Hill, "Plane wave integral representation for fields in reverberation chambers," *Electromagnetic Compatibility, IEEE Transactions on*, vol. 40, no. 3, pp. 209–217, 1998.

[24] R. G. Vaughan and M. Dehghani Estarki, "New bandwidth limits for dipoles," in *Progress In Electromagnetics Research Symposium (PIERS)*, Moscow, Russia, August 2012.

[25] M. Dehghani Estarki and R. G. Vaughan, "Theoretical methods for impedance and bandwidth of the thin dipole," *IEEE Antennas and Propagation Magazine*, April 2013.

[26] ——, "On the limits of simple array antennas for uncorrelated patterns," in *2011 IEEE International Symposium on Antennas and Propagation (APSURSI)*, Spokane, WA, USA, July 2011, pp. 2445–2448.

[27] ——, "On the power delay profile and delay spread for physics-based simulated mobile channel," in *Antennas and Propagation (EuCAP), 2013 7th European Conference on*, 2013, pp. 959–963.

[28] M. Dehghani Estarki, J. X. Yun, Y. L. C. de Jong, and R. G. Vaughan, "Multiport antenna performance analysis from ray-traced channels for small cells," in *Antennas and Propagation (EuCAP), 2014 8th European Conference on*, 2014.

[29] B. M. Kolundzija, J. S. Ognjanovic, and T. Sarkar, *WIPL-D: Electromagnetic Modeling of Composite Metallic and Dielectric Structures.* Norwood, MA, USA: Artech House, 2000.

[30] R. Lewallen. EZNEC Pro. [Online]. Available: www.eznec.com

[31] CST Microwave Studio. [Online]. Available: www.cst.com

[32] A. Taflove and K. R. Umashankar, "The finite-difference time-domain method for numerical modeling of electromagnetic wave interactions," *Electromagnetics*, vol. 10, no. 1, pp. 105–126, 1990.

[33] D. Sullivan, *Electromagnetic Simulation Using the FDTD Method.* New York, NY, USA: IEEE Press, 2000.

[34] O. Franek, *Private Communications with R. G. Vaughan.* Aalborg University, Denmark, 2009.

[35] J. B. Andersen, "Admittance of infinite and finite cylindrical metallic antenna," *Radio Science*, vol. 3, pp. 607–621, 1968.

[36] C. T. Tai, "Dipoles and monopoles," in *Antenna Engineering Handbook*, 2nd ed., R. C. Johnson and H. Jasik, Eds. New York, NY, USA: McGraw-Hill, 1993, ch. 4, pp. 4–1–4–34.

[37] C. A. Balanis, *Antenna Theory: Analysis and Design*, 3rd ed. Hoboken, NJ, USA: John Wiley & Sons, Inc., 2005.

[38] J. D. Kraus and R. J. Marhefka, *Antennas: For All Applications*, 3rd ed. New York, NY, USA: McGraw-Hill, 2002.

[39] E. K. Miller, "Admittance dependence of the infinite cylindrical antenna upon exciting gap thickness," *Radio Science*, vol. 2, no. 12, pp. 1431–1435, 1967.

[40] R. W. P. King, *The Theory of Linear Antennas*. Cambridge, MA, USA: Harvard University Press, 1956.

[41] S. A. Schelkunoff and H. T. Friis, *Antennas: Theory and Practice*. New York, NY, USA: John Wiley & Sons, Inc., 1952.

[42] T. Do-Nhat and R. H. MacPhie, "On the effect of gap width on the admittance of solid circular cylindrical dipoles," *IEEE Transactions on Antennas and Propagation*, vol. 37, no. 12, pp. 1545–1553, December 1989.

[43] R. Collin and F. Zucker, *Antenna Theory, Part 1*. New York, NY, USA: McGraw-Hill, 1969.

[44] W. Stutzman and G. Thiele, *Antenna Theory and Design*. New York, NY, USA: John Wiley & Sons, Inc., 1981.

[45] R. MacPhie, "Radiation and impedance characteristics of a thin-wire transmission line-dipole system," in *Antennas and Propagation Society International Symposium, 1989. AP-S. Digest*, vol. 3, June 1989, pp. 1376–1379.

[46] E. Kaldjob, B. Geck, and H. Eul, "Impedance measurement of properly excited small balanced antennas," *Antennas and Wireless Propagation Letters, IEEE*, vol. 8, pp. 193–195, 2009.

[47] M. Weiner, S. Cruze, C. Li, and W. Wilson, *Monopole Elements on Circular Ground Planes*. Norwood, MA, USA: Artech House, 1987.

[48] L. Lewin, "A contribution to the theory of cylindrical antennas–radiation between parallel plates," *IRE Transactions on Antennas and Propagation*, vol. 7, no. 2, pp. 162–168, april 1959.

[49] N. Inagaki and T. Sekiguchi, "Integral equation and its solution for a cylindrical antenna having a finite gap at the driving point," *Electron. Commun. Japan*, vol. 52-B, no. 5, pp. 88–94, 1969.

[50] T. Do-Nhat and R. H. MacPhie, "The static electric field distribution between two semi-infinite circular cylinders: A model for the feed gap field of a dipole antenna," *IEEE Transactions on Antennas and Propagation*, vol. 35, no. 11, pp. 1273–1280, November 1987.

[51] ——, "Effect of gap length on the input admittance of center fed coaxial waveguides and infinite dipoles," *IEEE Transactions on Antennas and Propagation*, vol. 35, no. 11, pp. 1293–1299, November 1987.

[52] D. S. Jones, *Methods in Electromagnetic Wave Propagation*, 1st ed. Walton Street, Oxford, England: Clarendon Press, 1979.

[53] D. H. Werner, J. A. Huffman, and P. L. Werner, "An exact formulation for the electromagnetic fields of a cylindrical antenna with a triangular current distribution," *Radio Science*, vol. 31, no. 4, pp. 701–714, 1996.

[54] H. G. James, "A review of the major developments in our understanding of electric antennas in space plasmas," *The Radio Science Bulletin*, no. 336, pp. 75–94, March 2011.

[55] C. T. Tai and S. A. Long, "Dipoles and monopoles," in *Antenna Engineering Handbook*, 4th ed., J. L. Volakis, Ed. New York, NY, USA: McGraw-Hill Professional, 2007, ch. 4.

[56] S. Silver, *Microwave Antenna Theory and Design*, 1st ed. New York, NY, USA: McGraw-Hill, 1949.

[57] P. S. Carter, "Circuit relations in radiating systems and applications to antenna problems," *Proceedings of the Institute of Radio Engineers*, vol. 20, no. 6, pp. 1004–1041, November 1932.

[58] R. W. P. King and D. Middleton, "The cylindrical antenna: current and impedance," *Quarterly of Applied Mathematics*, vol. 3, pp. 302–335, 1946.

[59] E. Hallén, "Exact treatment of antenna current wave reflection at the end of a tube-shaped cylindrical antenna," *Institute of Radio Engineers Transactions on Antennas and Propagation*, vol. 4, no. 3, pp. 479–491, July 1956.

[60] Y. M. Chen and J. B. Keller, "Current on and input impedance of a cylindrical antenna," *Journal of Research of the National Bureau of Standards–D. Radio Propagation*, pp. 15–21, 1962.

[61] R. L. Fante, "Quality factor of general ideal antennas," *IEEE Transactions on Antennas and Propagation*, vol. 17, no. 2, pp. 151–155, March 1969.

[62] R. W. P. King and T. T. Wu, "Currents, charges, and near fields of cylindrical receiving and scattering antennas," *IEEE Transactions on Antennas and Propagation*, vol. 13, no. 6, pp. 978–979, November 1965.

[63] L. Shen, T. T. Wu, and R. W. P. King, "A simple formula of current in dipole antennas," *IEEE Transactions on Antennas and Propagation*, vol. 16, no. 5, pp. 542–547, September 1968.

[64] R. Mack, *A study of circular arrays-II, Cruft Laboratory*, Harvard University, technical reports 382-383, 1963.

[65] E. C. Jordan and K. G. Balmain, *Electromagnetic Waves and Radiating Systems*. Englewood Cliffs, NJ, USA: Prentice-Hall, Inc., 1950.

[66] R. H. Duncan, "Theory of the infinite cylindrical antenna including the feed point singularity in antenna current," *Journal of Research of the National Bureau of Standards-D. Radio Propagation*, pp. 181–187, 1962.

[67] R. A. Hurd and J. Jacobsen, "Admittance of an infinite cylindrical antenna with realistic gap field," *Electronics Letters*, vol. 4, no. 19, pp. 420–421, 1968.

[68] E. K. Miller and J. A. Landt, "Direct time-domain techniques for transient radiation and scattering from wires," *Proceedings of the IEEE*, vol. 68, no. 11, pp. 1396–1423, November 1980.

[69] H. T. Shamansky, A. K. Dominek, and L. Peters Jr, "Electromagnetic scattering by a straight thin wire," *IEEE Transactions on Antennas and Propagation*, vol. 37, no. 8, pp. 1019–1025, August 1989.

[70] A. G. Tijhuis, P. Zhongqiu, and A. R. Bretones, "Transient excitation of a straight thin-wire segment: a new look at an old problem," *IEEE Transactions on Antennas and Propagation*, vol. 40, no. 10, pp. 1132–1146, 1992.

[71] J. C. Bogerd, A. G. Tijhuis, and J. J. A. Klaasen, "Electromagnetic excitation of a thin wire: A traveling-wave approach," *IEEE Transactions on Antennas and Propagation*, vol. 46, no. 8, pp. 1202–1211, 1998.

[72] M. Fahmy, I. Eshrah, and M. Khalaf, "Simple closed-form solution for normalized current distribution and scattered field pattern for straight wires," in *Radio Science Conference, 2001. NRSC 2001. Proceedings of the Eighteenth National*, vol. 1. IEEE, 2001, pp. 185–195.

[73] Y. Hei Lo, S. He, L. Jiang, and C. Chew, "Finite-width gap excitation and impedance models," in *2011 IEEE International Symposium on Antennas and Propagation (APSURSI)*, Spokane, WA, USA, July 2011.

[74] R. S. Elliott, *Antenna Theory and Design*. Englewood Cliffs, NJ, USA: Prentice-Hall, Inc., 1981.

[75] L. Brillouin, "Origin of radiation resistance," *Radioelectricite*, vol. 3, pp. 147–152, 1922.

[76] D. Otto, "A note on the induced EMF method for antenna impedance," *IEEE Transactions on Antennas and Propagation*, vol. 17, no. 1, pp. 101–102, January 1969.

[77] J. B. Andersen, *Metallic and Dielectric Antennas*. Denmark: Polyteknisk Forlag, 1971.

[78] E. K. Miller and F. J. Deadrick, "Some computational aspects of thin-wire modeling," *Numerical and asymptotic techniques in electromagnetics*, pp. 89–127, 1975.

[79] M. L. Abell and J. P. Braselton, *Maple by Example*, 3rd ed. Academic Press, 2005.

[80] S. R. Best, "The foster reactance theorem and quality factor for antennas," *IEEE Antennas and Wireless Propagation Letters*, vol. 3, pp. 306–309, 2004.

[81] C. G. Montgomery, R. H. Dicke, and E. M. Purcell, *Principles of Microwave Circuits*. New York, NY, USA: McGraw-Hill, 1948.

[82] A. D. Yaghjian and S. R. Best, "Impedance, bandwidth, and Q of antennas," *IEEE Transactions on Antennas and Propagation*, vol. 53, no. 4, pp. 1298–1324, 2005.

[83] J. S. McLean, "A re-examination of the fundamental limits on the radiation q of electrically small antennas," *IEEE Transactions on Antennas and Propagation*, vol. 44, no. 5, pp. 672–675, May 1996.

[84] R. M. Foster, "A reactance theorem," *Bell System Technical Journal*, vol. 3, no. 2, pp. 259–267, 1924.

[85] O. S. Kim, O. Breinbjerg, and A. D. Yaghjian, "Electrically small magnetic dipole antennas with quality factors approaching the Chu lower bound," *IEEE Transactions on Antennas and Propagation*, vol. 58, no. 6, pp. 1898–1906, June 2010.

[86] R. E. Collin and S. Rothschild, "Evaluation of antenna Q," *IEEE Transactions on Antennas and Propagation*, vol. 12, no. 1, pp. 23–27, January 1964.

[87] R. C. Hansen and R. E. Collin, "A new Chu formula for Q," *IEEE Antennas and Propagation Magazine*, vol. 51, no. 5, pp. 38–41, October 2009.

[88] P. K. Park and C. T. Tai, "Receiving antennas," in *Antenna Handbook: Theory, Applications, and Design*, Y. T. Lo and S. W. Lee, Eds. New York, NY, USA: Van Nostrand Reinhold, 1988, ch. 6.

[89] R. C. Hansen, "Fundamental limitations in antennas," *Proceedings of the IEEE*, vol. 69, no. 2, pp. 170–182, February 1981.

[90] P. Hansen and R. Adams, "The minimum Q for spheroidally shaped objects: Extension to cylindrically shaped objects and comparison to practical antennas," *Antennas and Propagation Magazine, IEEE*, vol. 53, no. 3, pp. 75–83, June 2011.

[91] R. G. Vaughan, "Antenna evaluation for communications with diversity/MIMO," in *Printed Antennas*, 1st ed., R. Waterhouse, Ed. West Sussex, England: John Wiley & Sons, Ltd., 2007, ch. 15, pp. 407–445.

[92] R. C. Hansen, *Electrically Small, Superdirective, and Superconducting antennas*. New York, NY, USA: Wiley-Interscience, 2006.

[93] J. B. Andersen and A. Frandsen, "Absorption efficiency of receiving antennas," *IEEE Transactions on Antennas and Propagation*, vol. 53, no. 9, pp. 2843–2849, September 2005.

[94] D. M. Grimes and C. A. Grimes, "Radiation Q of dipole-generated fields," *Radio Science*, vol. 34, no. 2, pp. 281–296, 1999.

[95] S. R. Best and D. L. Hanna, "A performance comparison of fundamental small-antenna designs," *IEEE Antennas and Propagation Magazine*, vol. 52, no. 1, pp. 47–70, February 2010.

[96] J. Ren, "Absolute phase in mobile channels," Ph.D. dissertation, Simon Fraser University, Burnaby, BC, Canada, 2010.

[97] S. Ramo, J. R. Whinnery, and T. V. Duzer, *Fields and Waves in Communication Electronics*. New York, NY, USA: John Wiley & Sons, Inc., 1965.

[98] F. T. Ulaby, *Fundamentals of Applied Electromagnetics*. Upper Saddle River, NJ, USA: Prentice-Hall, Inc., 2001.

[99] R. E. Collin, *Antennas and Radiowave Propagation*. New York, NY, USA: McGraw-Hill, 1985.

[100] J. A. Stratton, *Electromagnetic Theory*. New York, NY, USA: McGraw-Hill, 1941.

[101] *IEEE Standard Test Procedures for Antennas*. IEEE Std. 149-1979, 1979.

[102] R. Mailloux, *Phased Array Antenna Handbook*. Boston, MA, USA: Artech House, 1994.

[103] P. A. Bello and B. D. Nelin, "The effect of frequency selective fading on the binary error probabilities of incoherent and differentially coherent matched filter receivers," *Communications Systems, IEEE Transactions on*, vol. 11, no. 2, pp. 170 –186, June 1963.

[104] W. C. Jakes Jr., *Microwave Mobile Communications*. Wiley, New York, 1974.

[105] C. L. Holloway, M. G. Cotton, and P. McKenna, "A model for predicting the power delay profile characteristics inside a room," *Vehicular Technology, IEEE Transactions on*, vol. 48, no. 4, pp. 1110–1120, 1999.

[106] D. J. Y. Lee and W. C. Y. Lee, "Propagation prediction in and through buildings," *Vehicular Technology, IEEE Transactions on*, vol. 49, no. 5, pp. 1529–1533, 2000.

[107] M. Geissler, C. Oikonomopoulos-Zachos, T. Ould, and M. Arnold, "MIMO performance optimisation of car antennas," in *Antennas and Propagation (EUCAP), 2012 6th European Conference on*. IEEE, 2012, pp. 2750–2753.

[108] Y. Sun, J. Zhang, C. Pan, and P. Zhang, "Optimal and computational-efficient detection and estimation of multi-paths in channel sounding," in *Vehicular Technology Conference, 2013. VTC2013-Fall. IEEE 78th.* IEEE, 2013.

[109] D. J. Y. Lee and W. C. Y. Lee, "Enhanced Lee in-building model," in *Vehicular Technology Conference, 2013. VTC2013-Fall. IEEE 78th.* IEEE, 2013.

[110] M. F. Catedra, J. Perez, F. Saez de Adana, and O. Gutierrez, "Efficient ray-tracing techniques for three-dimensional analyses of propagation in mobile communications: application to picocell and microcell scenarios," *Antennas and Propagation Magazine, IEEE*, vol. 40, no. 2, pp. 15–28, 1998.

[111] R. A. Scholtz, R. J.-M. Cramer, and M. Z. Win, "Evaluation of the propagation characteristics of ultra-wideband communication channels," in *Antennas and Propagation Society International Symposium, 1998. IEEE*, vol. 2, 1998, pp. 626–630.

[112] M. Z. Win and R. A. Scholtz, "Characterization of ultra-wide bandwidth wireless indoor channels: a communication-theoretic view," *Selected Areas in Communications, IEEE Journal on*, vol. 20, no. 9, pp. 1613–1627, 2002.

[113] R. G. Vaughan and N. L. Scott, "Super-resolution of pulsed multipath channels for delay spread characterization," *Communications, IEEE Transactions on*, vol. 47, no. 3, pp. 343–347, 1999.

[114] T. C. K. Liu, D. I. Kim, and R. G. Vaughan, "A high-resolution, multi-template deconvolution algorithm for time-domain UWB channel characterization," *Electrical and Computer Engineering, Canadian Journal of*, vol. 32, no. 4, pp. 207–213, 2007.

[115] S. Salous, *Radio Propagation Measurement and Channel Modelling*, 1st ed. West Sussex, United Kingdom: John Wiley and Sons Ltd., 2013.

[116] I. Ashdown, *Radiosity: a Programmer's Perspective*, 1st ed. New York, USA: John Wiley and Sons Inc., 1994.

[117] Z. Zhimeng, Y. Xuefeng, X. Li, and L. Xue, "Extension of ITU IMT-advanced channel models for elevation domain and line-of-sight scenarios," in *Vehicular Technology Conference, 2013. VTC2013-Fall. IEEE 78th.* IEEE, 2013.

[118] J. Medbo, H. Asplund, J.-E. Berg, and N. Jalden, "Directional channel characteristics in elevation and azimuth at an urban macrocell base station," in *Antennas and Propagation (EUCAP), 2012 6th European Conference on.* IEEE, 2012, pp. 428–432.

[119] E. Perahia and R. Stacey, *Next generation wireless LANs*. Cambridge University Press Cambridge, 2008, vol. 417.

[120] R. Vaughan, N. Scott, and J. Southon, "Characterization of standing wave movement by in-line antennas," in *Antennas and Propagation Society International Symposium, 1991. AP-S. Digest*. IEEE, 1991, pp. 974–977.

[121] A. Richter, "Estimation of radio channel parameters: Models and algorithms," Ph.D. dissertation, Technische Universität Ilmenau, Ilmenau, ISLE, Germany, 2005.

[122] A. F. Molisch, *Wireless Communications*. West Sussex, England: Wiley, 2011.

[123] J. Fuhl, J.-P. Rossi, and E. Bonek, "High-resolution 3-d direction-of-arrival determination for urban mobile radio," *Antennas and Propagation, IEEE Transactions on*, vol. 45, no. 4, pp. 672–682, 1997.

[124] U. Martin, "Spatio-temporal radio channel characteristics in urban macrocells," in *Radar, Sonar and Navigation, IEE Proceedings-*, vol. 145, no. 1. IET, 1998, pp. 42–49.

[125] U. Martin, J. Fuhl, I. Gaspard, M. Haardt, A. Kuchar, C. Math, A. F. Molisch, and R. Thomä, "Model scenarios for direction-selective adaptive antennas in cellular mobile communication systems–scanning the literature," *Wireless Personal Communications*, vol. 11, no. 1, pp. 109–129, 1999.

[126] R. B. Ertel, P. Cardieri, K. W. Sowerby, T. S. Rappaport, and J. H. Reed, "Overview of spatial channel models for antenna array communication systems," *Personal Communications, IEEE*, vol. 5, no. 1, pp. 10–22, 1998.

[127] R. G. Vaughan, "Spaced directive antennas for mobile communications by the fourier transform method," *Antennas and Propagation, IEEE Transactions on*, vol. 48, no. 7, pp. 1025–1032, 2000.

[128] R. G. Vaughan and J. B. Andersen, "Antenna diversity in mobile communications," *Vehicular Technology, IEEE Transactions on*, vol. 36, no. 4, pp. 149–172, 1987.

[129] Bing Maps. [Online]. Available: http://www.bing.com/maps/

[130] M. Wittmann, J. Marti, and T. Kürner, "Impact of the power delay profile shape on the bit error rate in mobile radio systems," *Vehicular Technology, IEEE Transactions on*, vol. 46, no. 2, pp. 329–339, 1997.

[131] T. Cui and C. Tellambura, "Power delay profile and noise variance estimation for ofdm," *Communications Letters, IEEE*, vol. 10, no. 1, pp. 25–27, 2006.

[132] D. Cox, "910 MHz urban mobile radio propagation: Multipath characteristics in New York City," *Communications, IEEE Transactions on*, vol. 21, no. 11, pp. 1188–1194, 1973.

[133] D. M. J. Devasirvatham, "Time delay spread measurements of wideband radio signals within a building," *Electronics Letters*, vol. 20, no. 23, pp. 950–951, 1984.

[134] A. Paier, J. Karedal, N. Czink, H. Hofstetter, C. Dumard, T. Zemen, F. Tufvesson, A. F. Molisch, and C. F. Mecklenbrauker, "Car-to-car radio channel measurements at 5 ghz: Pathloss, power-delay profile, and delay-doppler spectrum," in *Wireless Communication Systems, 2007. ISWCS 2007. 4th International Symposium on*, Oct. 2007, pp. 224 –228.

[135] V. Erceg, D. G. Michelson, S. S. Ghassemzadeh, L. J. Greenstein, A. J. Rustako Jr, P. B. Guerlain, M. K. Dennison, R. S. Roman, D. J. Barnickel, S. C. Wang, and R. R. Miller, "A model for the multipath delay profile of fixed wireless channels," *Selected Areas in Communications, IEEE Journal on*, vol. 17, no. 3, pp. 399–410, 1999.

[136] J. Chuang, "The effects of time delay spread on portable radio communications channels with digital modulation," *Selected Areas in Communications, IEEE Journal on*, vol. 5, no. 5, pp. 879–889, 1987.

[137] D. Devasirvatham, "Time delay spread and signal level measurements of 850 mhz radio waves in building environments," *Antennas and Propagation, IEEE Transactions on*, vol. 34, no. 11, pp. 1300–1305, 1986.

[138] D. Cox and R. Leck, "Correlation bandwidth and delay spread multipath propagation statistics for 910-MHz urban mobile radio channels," *Communications, IEEE Transactions on*, vol. 23, no. 11, pp. 1271–1280, 1975.

[139] L. J. Greenstein, V. Erceg, Y. S. Yeh, and M. V. Clark, "A new path-gain/delay-spread propagation model for digital cellular channels," *Vehicular Technology, IEEE Transactions on*, vol. 46, no. 2, pp. 477 –485, May 1997.

[140] E. S. Sousa, V. M. Jovanovic, and C. Daigneault, "Delay spread measurements for the digital cellular channel in toronto," *Vehicular Technology, IEEE Transactions on*, vol. 43, no. 4, pp. 837–847, 1994.

[141] R. Vaughan, "Finite sample estimates for mobile channels," in *Vehicular Technology Conference, 2000. IEEE VTS-Fall VTC 2000. 52nd*, vol. 2. IEEE, 2000, pp. 797–804.

[142] W. C. Y. Lee, *Mobile Communications Engineering: Theory and Applications.* New York, NY, USA: McGraw-Hill, Inc., 1997.

[143] G. Stüber, *Principles of Mobile Communication*, 2nd ed. USA: Kluwer Academic Publishers, 2001.

[144] D. Wong and D. Cox, "An optimal local mean signal power level estimator for rayleigh fading environments," in *Information, Communications and Signal Processing, 1997. ICICS., Proceedings of 1997 International Conference on*, vol. 3. IEEE, 1997, pp. 1701–1704.

[145] W. C. Y. Lee, "Estimate of local average power of a mobile radio signal," *Vehicular Technology, IEEE Transactions on*, vol. 34, no. 1, pp. 22–27, 1985.

[146] R. G. Vaughan and N. L. Scott, "Closely spaced monopoles for mobile communications," *Radio science*, vol. 28, no. 6, pp. 1259–1266, 1993.

[147] R. A. Valenzuela, O. Landron, and D. Jacobs, "Estimating local mean signal strength of indoor multipath propagation," *Vehicular Technology, IEEE Transactions on*, vol. 46, no. 1, pp. 203–212, 1997.

[148] V. Erceg, A. Rustako Jr, and R. Roman, "Diffraction around corners and its effects on the microcell coverage area in urban and suburban environments at 900 mhz, 2 ghz, and 4 ghz," *Vehicular Technology, IEEE Transactions on*, vol. 43, no. 3, pp. 762–766, 1994.

[149] Y. L. C. de Jong and M. A. H. J. Herben, "Prediction of local mean power using 2-d ray-tracing-based propagation models," *Vehicular Technology, IEEE Transactions on*, vol. 50, no. 1, pp. 325–331, 2001.

[150] D. Wong and D. Cox, "Estimating local mean signal power level in a rayleigh fading environment," *Vehicular Technology, IEEE Transactions on*, vol. 48, no. 3, pp. 956–959, 1999.

[151] W. C. Lee, *Mobile communications engineering*. McGraw-Hill Professional, 1982.

[152] A. Goldsmith, *Wireless Communications*, 1st ed. Cambridge University Press, 2005.

[153] A. F. Molisch and F. Tufvesson, "Multipath propagation models for broadband wireless systems," in *Digital Signal Processing for Wireless Communications Handbook*, M. Ibnkahda, Ed. CRC Press, 2004, ch. 2, pp. 2.1–2.43.

[154] W. C. Jakes, Y. S. Yeh, M. J. Gans, and D. O. Reudink, "Fundamentals of diversity systems," in *Microwave Mobile Communications*, reissue of 1st ed., W. C. Jakes, Ed. New York: IEEE Press, 1994, ch. 5, pp. 309–387.

[155] O. Nørklit and R. G. Vaughan, "Method to determine effective number of diversity branches," in *Global Telecommunications Conference, 1998. GLOBECOM 1998. IEEE*, vol. 1, 1998, pp. 138–141.

[156] J. Salo, K. Haneda, V. M. Kolmonen, A. A. H. Azremi, and P. Vainikainen, "Measurement-based evaluation of link budget gain from 3GPP LTE uplink transmit antenna selection," in *Vehicular Technology Conference, 2013. VTC2013-Spring. IEEE 77th.* IEEE, 2013.

[157] B. N. Getu and J. B. Andersen, "The MIMO cube-a compact MIMO antenna," *Wireless Communications, IEEE Transactions on*, vol. 4, no. 3, pp. 1136–1141, 2005.

[158] M. Gustafsson and S. Nordebo, "Characterization of mimo antennas using spherical vector waves," *Antennas and Propagation, IEEE Transactions on*, vol. 54, no. 9, pp. 2679–2682, 2006.

[159] J. Yun and R. Vaughan, "Slot mimo cube," in *Antennas and Propagation Society International Symposium (APSURSI), 2010 IEEE*, 2010, pp. 1–4.

[160] X. Qing, Z. N. Chen, and T. S. P. See, "A multi-band MIMO antenna with full coverage," in *Antennas and Propagation (EUCAP), Proceedings of the 5th European Conference on*, 2011, pp. 2497–2500.

[161] C. Hofmann, A. Knopp, and B. Lankl, "Indoor los MIMO channel measurements with a focus on antenna array design," in *Global Telecommunications Conference (GLOBECOM 2010), 2010 IEEE*, 2010, pp. 1–5.

[162] J. X. Yun, "Design and evaluation of slot antennas," Ph.D. dissertation, Simon Fraser University, 2011.

[163] M. Dehghani Estarki and R. G. Vaughan, "Software-based design of multiple antenna systems for large wireless capacities," in *Wireless World Research Forum, Vancouver, Canada*, October, 2013.

[164] J. Ren and R. G. Vaughan, "Rice factor estimation from the channel phase," *IEEE Transactions on Wireless Communications*, vol. 11, no. 6, pp. 1976–1980, June 2012.

Appendix A

Induced EMF Approach

For a dipole along the z-axis, and wire radius of a, the induced EMF method requires the tangential z-directed electric field on the dipole surface $E_z(a, z)$. The excitation can be by magnetic frill or infinitesimal voltage gap or current element. Traditionally, a centre current element is used and so such an excitation is applied here to offer consistent results with previous EMF method solutions, i.e., for the 'no gap' case. The electric field vector is written as

$$\mathbf{E} = \hat{\rho} E_\rho + \hat{\mathbf{z}} E_z, \tag{A.1}$$

where $\hat{\rho}$ and $\hat{\mathbf{z}}$ are the unit vectors and E_ρ and E_z are the vector components in the cylindrical coordinate system. The field components are as follows,

$$\begin{aligned} E_\rho = j\frac{\eta I_o}{4\pi y}[(z-\frac{l}{2})\frac{e^{-jkR_1}}{R_1} + (z+\frac{l}{2})\frac{e^{-jkR_2}}{R_2} \\ - 2z\cos(\frac{kl}{2})\frac{e^{-jkr}}{r}], \end{aligned} \tag{A.2}$$

$$E_z = -j\frac{\eta I_o}{4\pi}\left[\frac{e^{-jkR_1}}{R_1} + \frac{e^{-jkR_2}}{R_2} - 2\cos(\frac{kl}{2})\frac{e^{-jkr}}{r}\right], \tag{A.3}$$

where R_1 and R_2 are the distances to the two ends of the dipole and r is the distance of the observation point to the origin. For sinusoidal current excitation, the input impedance Z_m can be found by solving the following integral which contains only E_z. (E_ρ component

is not needed for the induced EMF method.)

$$Z_m = -\frac{1}{I_m}[\int_{-\frac{l}{2}}^{-\frac{\delta}{2}} \sin\left[k(\frac{l}{2}+z^{'})\right] E_z(\rho=a, z=z^{'})dz^{'} + \int_{+\frac{\delta}{2}}^{+\frac{l}{2}} \sin\left[k(\frac{l}{2}-z^{'})\right] E_z(\rho=a, z=z^{'})\ dz^{'}]. \tag{A.4}$$

Appendix B

Trigonometric Integrals

$$
\begin{aligned}
P_{rad} = \eta \frac{|I_0|^2}{4\pi} \{ & C_{Euler} + \ln(kl) - C_i(kl) \\
& + \frac{1}{2}\sin(kl)[S_i(2kl) - 2S_i(kl)] \\
& + \frac{1}{2}\cos(kl)[C_{Euler} + \ln(\frac{kl}{2}) + C_i(2kl) - 2C_i(kl)] \Big\},
\end{aligned} \tag{B.1}
$$

where P_{rad} is the radiation power and C_{Euler} is the Euler's constant $C_{Euler} \approx 0.5772$ (introduced in chapter 2, section 2.5.1).

$$
S_i(x) = \int_0^x \frac{\sin y}{y} dy, \tag{B.2}
$$

$$
C_i(x) = -\int_x^\infty \frac{\cos y}{y} dy, \tag{B.3}
$$

$$
\begin{aligned}
C_{in}(x) =& \ln(\gamma x) - C_i(x) && \text{(B.4a)} \\
=& C_{Euler} + \ln(x) - C_i(x) && \text{(B.4b)} \\
=& \int_0^x \frac{1 - \cos y}{y} dy && \text{(B.4c)}
\end{aligned}
$$

Appendix C

Q from Measurement and Simulation

C.1 Q from Measurement Results

A fair in-depth comparison is not provided unless all the three methods for impedance, i.e., theory, simulations and measurement, are included. The Q from measurement are adapted from Best's paper (2004) [80]. The range of frequency, the dipole thickness and length are different from those of our research although there is some overlap. Therefore, a few frequency samples, i.e., corresponding to different electrical lengths, is chosen form the measured results which are within the range studied in this research and their impedance and Q factors are put together with the simulation and theoretical results. In [80], section III, the dimensions of the monopole and the frequency range are specified as,

- length, $l_m = 17.25$cm,
- radius, $a = 1$mm,
- frequency, $f = [300 - 1500]$ MHz.

Considering the length of the monopole, l_m, the length of the equivalent dipole is $l_d = 34.5$cm. Therefore, when the frequency of the operation is transformed to the electrical length, the length of the dipole in wavelength will be (there is an electrical length, i.e., $\frac{l_d}{\lambda}$,

corresponding to any frequency):

$$\frac{l_d}{\lambda} = \frac{34.5 \times 10^{-2}}{3 \times 10^8} \times [300 \ ... \ 1500] \times 10^6 \tag{C.1a}$$

$$= [0.345 \ ... \ 1.7250] \, . \tag{C.1b}$$

The electrical lengths of interest for which the Q is sought, are

$$\frac{l_d}{\lambda} = [0.45, \ 0.55, \ 0.66] \, , \tag{C.2}$$

which according to (C.1) correspond to the following operating frequencies:

$$f = [391, \ 478, \ 573] \, \text{MHz}. \tag{C.3}$$

The electrical radii for these three frequencies, i.e., equation (C.3), are also as follows:

$$\frac{a}{\lambda} = \frac{a}{c} \times f = \frac{a}{3 \times 10^8} \times [391, \ 478, \ 573] \times 10^6 \tag{C.4a}$$

$$= [0.0013, \ 0.0016, \ 0.0019] \, . \tag{C.4b}$$

In [80], Figure 8, the Q variation versus frequency has been shown. For the frequencies of interest, i.e., $f = [391, \ 478, \ 573] \, \text{MHz}$, (corresponding to $\frac{l_d}{\lambda} = [0.45, \ 0.55, \ 0.66]$, the Qs can readily be accessible, *viz*,

$$Q = [6.9, \ 4.9, \ 4.3] \, . \tag{C.5}$$

C.2 Simulation Results (MOM)

The results from both simulation and measurement are presented in [80], Figures 2, 3 and 8. The MOM was also applied with exactly the same dimensions as the dimensions in [80], i.e., $l_d = 34.50\text{cm}$, $a = 1\text{mm}$, and the same range of operating frequency, i.e., $f = [300 - 1500]\text{MHz}$. The simulation was repeated for different gap sizes, Some sample results for gap size 10^{-2}mm are included here. The results were checked with those of [80]. The Q values agree well for the frequencies of interest, refer to Figure C.4 (green line).

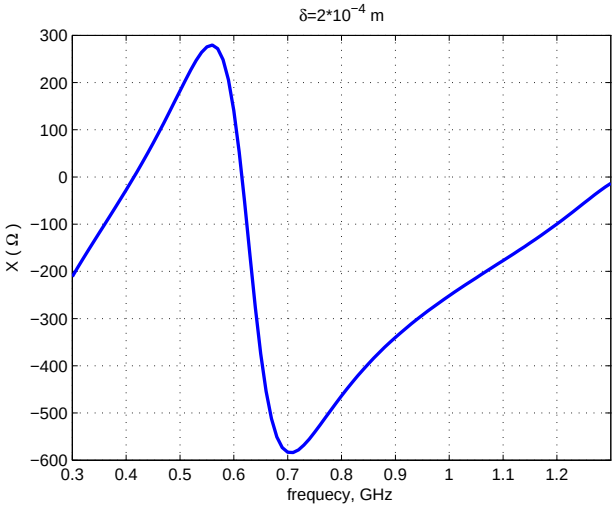

Figure C.1: Reactance

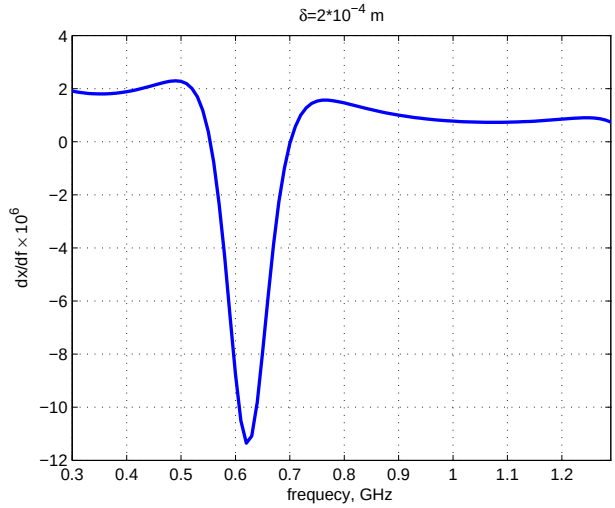

Figure C.2: Derivative of reactance

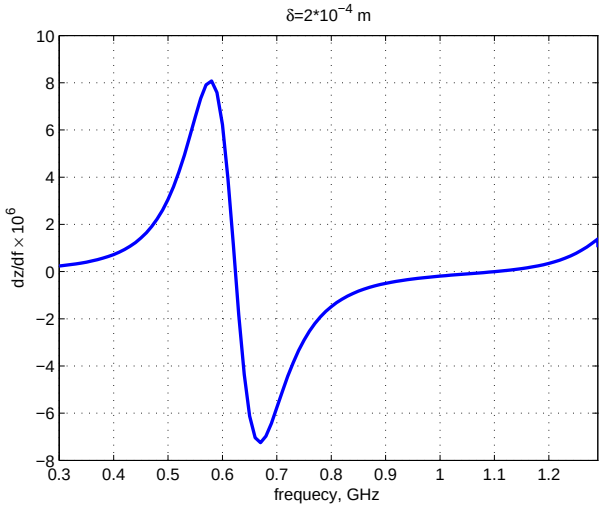

Figure C.3: Derivative of impedance (absolute value)

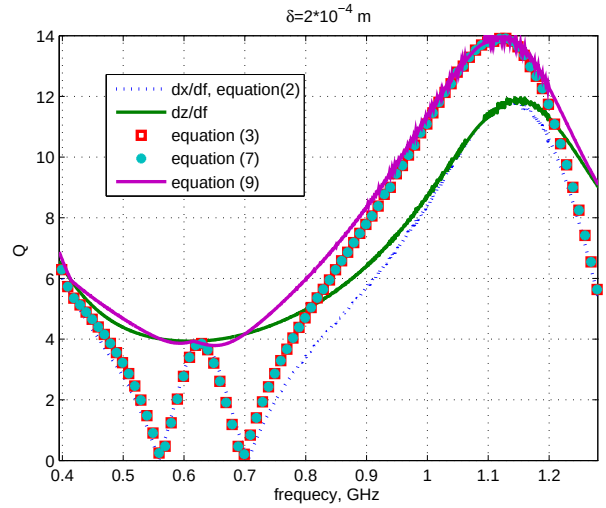

Figure C.4: Q (absolute value), calculated from the Q derivations in [80]